

**SHEAR RHEOMETRY PROTOCOLS TO ADVANCE THE DEVELOPMENT OF  
MICROSTRUCTURED FLUIDS**

by

**Eduard Andres Caicedo Casso**

**A Dissertation**

*Submitted to the Faculty of Purdue University*

*In Partial Fulfillment of the Requirements for the degree of*

**Doctor of Philosophy**



School of Materials Engineering

West Lafayette, Indiana

May 2019

**THE PURDUE UNIVERSITY GRADUATE SCHOOL  
STATEMENT OF COMMITTEE APPROVAL**

Dr. Kendra A. Erk, Chair

School of Materials Engineering

Dr. John A. Howarter

School of Materials Engineering

Dr. Carlos Martinez

School of Materials Engineering

Dr. Bryan W. Boudouris

School of Chemical Engineering

**Approved by:**

Dr. David F. Bahr

Head of the Graduate Program

*The culmination of this work would not have been possible without the unconditional support of  
my heroes:*

*My mon Blanca Nory Casso Bolaños*

*My dad Pedro Emilio Caicedo*

*My sister Angelica G Caicedo Casso*

*My second Mon Maria Nasly Casso Bolaños*

*My wife Urszula K Ochnik*

*and my grandfather Jose Ruben Casso Rivera*

***“In time of test, family is best.”***

***-Burmese Proverb***

## ACKNOWLEDGMENTS

Today I am very happy for having the opportunity to write these short lines to recognize the people and entities that diligently contributed to my doctoral education.

First, I would like to express my sincere gratitude to Dr. Kendra A Erk for accepting me as an active part of her research group. Her unconditional support and encouragement allowed me to learn the art of research and become a better engineer.

Furthermore, I am grateful for the genuine collaboration of my committee members Dr. John A Howarter, Dr. Carlos Martinez, and Dr. Bryan W Boudouris. Their insightful input during every step of my program opened my mind to new and distinct ideas to approach engineering challenges.

Besides, I want to express my appreciation to Dr. Travis Thornell who introduced me to the world of Rheometry, MS. Seth Linberg who showed me the life of an engineer in industry, and Dr. Kevin Trumble for his inspiration to practice deep and honest science. Also, I am very grateful for the collaboration of my lab mates Jessica Sargent, Baishakhi Bose, Ryan Szeto, Cole Davis, MS Jason Bice, Dr. Jerome Nash, Dr. Anna Walter, and Dr. Matthew Krafcik.

Lastly, I want to acknowledge the entities that found my doctoral journey. I express my gratitude for the financial support of the School of Materials Engineering at Purdue University, the National Science Foundation under Grant No. 1436255, and the Global Engineering leadership program at Procter and Gamble Co.

## TABLE OF CONTENTS

LIST OF TABLES .....	8
LIST OF FIGURES .....	9
ABSTRACT .....	11
1. INTRODUCTION .....	13
1.1 Scope of this Dissertation .....	15
1.2 Basics of Rheology .....	17
1.3 Basics of Shear Rheometry .....	19
1.4 Basics of Ultrasonic Speckle Velocimetry .....	22
1.5 References .....	23
2. RHEOLOGICAL AND MECHANICAL CHARACTERIZATION OF EVAPORATION- INDUCED MICROSTRUCTURES: THE CASE OF SELF-ASSEMBLY BLOCK COPOLYMERS.....	27
2.1 Introduction.....	27
2.2 Materials and Experimental Methods .....	31
2.2.1 Triblock copolymer samples.....	31
2.2.2 Characterization.....	32
2.2.2.1 Rheometry with minimal evaporation .....	32
2.2.2.2 Mechanical strength development upon solvent evaporation.....	32
2.2.2.3 Solvent evaporation rate .....	34
2.3 Results.....	35
2.3.1 Rheometry results with minimal evaporation.....	35
2.3.2 Rheometry results with significant evaporation .....	36
2.3.3 Solvent evaporation studies .....	40
2.4 Discussion .....	41
2.4.1 The effect of block chemistry on the flow behavior (no evaporation) .....	41
2.4.2 Viscoelastic behavior with significant evaporation .....	45
2.4.3 The block chemistry effect over the solvent evaporation rate .....	49
2.5 Summary and Implications .....	49
2.6 References.....	50

3. RHEO-PHYSICAL CHARACTERIZATION OF MICROSTRUCTURES SENSITIVE TO SHEAR DEFORMATION: THE CASE OF CONCENTRATED SURFACTANT SOLUTIONS.....	55
3.1 Introduction.....	55
3.2 Materials and Methods.....	59
3.2.1 Surfactant paste formulation.....	59
3.2.2 Bulk shear rheometry measurements.....	60
3.2.3 Ultrasonic rheo-flow velocimetry measurements.....	60
3.2.4 Microstructural characterization.....	62
3.2.4.1 Small-angle x-ray scattering.....	62
3.2.4.2 Optical microscopy and flow birefringence.....	63
3.3 Results.....	64
3.3.1 X-ray scattering patterns.....	64
3.3.2 Bulk shear rheometry results.....	65
3.3.3 Results from advanced rheo-physical measurements.....	67
3.3.4 Polarized light microscopy and birefringence observations.....	70
3.4 Discussion.....	73
3.4.1 Newtonian behavior of the spherical micelle sample.....	73
3.4.2 Bimodal behavior of worm-like micelle sample.....	74
3.4.3 Plug flow of the hexagonal sample.....	76
3.4.4 Apparent yield stresses of lamellar samples.....	78
3.5 Summary and Implications.....	80
3.6 References.....	82
4. SHEAR RHEOMETRY AS MEASURING TOOL OF THE POLYMER EROSION CONCENTRATION FOR POLYMER DISSOLUTION: THE CASE OF A SEMYCRYSTALLINE WATER-SOLUBLE POLYMER.....	90
4.1 Introduction.....	90
4.2 Materials and Methods.....	94
4.2.1 Materials.....	94
4.2.2 The stirrer-vial dissolution test work-flow.....	95
4.2.3 Average solvent shear rate for the stirrer-vial set-up.....	96

4.2.4	Calculation of velocity of diffusion for the stirrer-vial dissolution test .....	97
4.2.5	Film dissolution test work-flow .....	99
4.2.6	The diffusion coefficient of a Selvol E 205 chain in water .....	100
4.2.7	The link with shear rheology in the determination of $C_e$ .....	101
4.3	Results .....	102
4.3.1	Flow characterization .....	102
4.3.2	$C_e$ determination .....	103
4.3.3	The velocity of diffusion in the stirrer-vial dissolution test .....	106
4.3.4	The velocity of diffusion in the film dissolution test .....	107
4.4	Discussion .....	108
4.4.1	Viscoelastic response of samples S and SPPG and $C_e$ determination .....	109
4.4.2	Mass flux at the gel-solvent interface .....	112
4.4.3	Mass transfer correlations .....	115
4.4.4	Stirrer-vial versus films dissolution test. ....	116
4.5	Summary and Implications .....	117
4.6	References .....	118
5.	CONCLUSIONS AND FUTURE WORK .....	123
5.1	Conclusion .....	123
5.2	Future Work .....	124
VITA	.....	126

## LIST OF TABLES

Table 2-1. Composition of the polymers investigated in this study. ....	32
Table 2-2. Hansen solubility parameters for each component of the triblock terpolymer solutions. .....	43
Table 4-1. Physical constants for the stirrer-vial dissolution test. ....	97
Table 4-2. Oscillation stress for the linear viscoelastic range .....	105
Table 4-3. $C_e$ as a function of solvent Reynolds number in the stirrer-vial dissolution test .....	106
Table 4-4. Dissolution time as a function of film thickness for the film dissolution test.....	108

## LIST OF FIGURES

Figure 1-1 Typical rheological behaviors .....	18
Figure 1-2 Maxwell spring-dashpot model.....	18
Figure 1-3 . Shear rheometry most popular geometries.....	19
Figure 1-4 Representation of steady flow and most common flow instabilities as one-dimensional velocity profiles .....	22
Figure 1-5 USV electronic equipment illustration on the shear rheometer .....	23
Figure 2-1 Preliminary attempts of producing SNIPS membranes through roll-to-roll casting...	29
Figure 2-2 Triblock copolymer molecular structures .....	31
Figure 2-3. Illustration of the four parameters calculated from the oscillatory test upon solvent evaporation.....	34
Figure 2-4. Illustration of the physical set-up used to measure the diffusion coefficient of solvent through cast polymer films .....	34
Figure 2-5. Rheometry with minimal evaporation.....	36
Figure 2-6. Alternative test to determine the LVR .....	37
Figure 2-7. Mechanical strength development upon solvent evaporation .....	38
Figure 2-8. Summary of calculated four parameters .....	39
Figure 2-9. Viscous-to-elastic cross-over points for ISV, ISB, and ISD solutions .....	40
Figure 2-10. Diffusion coefficient for a solvent mixture of THF-DOX (30-70) through ISV, ISB, and ISD terpolymer films.....	40
Figure 2-11. Hypothesized location of an evaporation-induced viscoelastic film.....	46
Figure 3-1 Microstructural organization of sodium laureth sulfate (SLE <sub>1</sub> S) in deionized water .	56
Figure 3-2 Illustration of the velocimetry data .....	62
Figure 3-3 Small-angle X-ray scattering patterns for the surfactant solutions .....	64
Figure 3-4 Flow curve and mathematical fitting for all surfactant solutions.....	66
Figure 3-5 Flow-velocimetry shear start-up data for the following specimens .....	67
Figure 3-6 Flow curve and USV shear stress plateau relationship .....	68
Figure 3-7 Rheo-flow velocimetry results .....	69
Figure 3-8 Light microscopy (crossed-polarized) of 70 wt.% SLE <sub>1</sub> S (lamellar-70 sample) at rest .....	71

Figure 3-9 Polarized light imaging of 70 wt.% SLE <sub>1</sub> S (lamellar-70 sample) in the Linkam shear stage .....	72
Figure 3-10 Spherical sample: flow curve and flow velocimetry relationship.....	74
Figure 3-11 Worm-like sample: flow curve and flow velocimetry relationship .....	75
Figure 3-12 Hexagonal sample: flow curve and flow velocimetry relationship.....	77
Figure 3-13 Lamellar-40 flow curve and flow velocimetry relationship.....	78
Figure 3-14 Lamellar-70 sample: flow curve and flow velocimetry relationship .....	79
Figure 4-1. General dissolution framework of a dry polymer specimen that is being attacked by a penetrating solvent .....	91
Figure 4-2. Vial-stirrer experimental set up used for dissolution experiments.....	95
Figure 4-3. Film dissolution test set-up .....	99
Figure 4-4. Image sequence of the dissolution film test .....	100
Figure 4-5. Flow curve for sample S and SPPG .....	102
Figure 4-6. $G'$ and $G''$ general behavior of samples and SPPG.....	103
Figure 4-7. $G'$ data as a function of oscillation strain on a linear-log scale .....	104
Figure 4-8. $C_e$ master curve: oscillation stress necessary for viscous deformation as a function of polymer concentration .....	105
Figure 4-9. Gel-solvent interface position over time as a function of applied Reynolds number .....	106
Figure 4-10. Experimental and calculated dissolution time ratio of films as a function of the film thickness.....	108
Figure 4-11. $C_e$ versus the solvent shear rate .....	112
Figure 4-12. The evolution of the gel-solvent interface over time and its dependency with applied Reynolds number .....	113
Figure 4-13. Empirical Sherwood number as a function of Reynolds number of sample S and SPPG .....	116

## ABSTRACT

Author: Caicedo-Casso, Eduard, A. PhD

Institution: Purdue University

Degree Received: May 2019

Title: Shear Rheometry Protocols to Advance the Development of Microstructured Fluids.

Committee Chair: Kendra Erk

This doctoral dissertation takes the reader through a journey where applied shear rheology and flow-velocimetry are used to understand the mesoscopic factors that control the flow behavior of three microstructured fluids. Three individual protocols that measure relative physical and mechanical properties of the flow are developed. Each protocol aims to advance the particular transformation of novel soft materials into a commercial product converging in the demonstration of the real the chemical, physical and thermodynamical factors that could potentially drive their successful transformation.

First, this dissertation introduces the use of rotational and oscillatory shear rheometry to quantify the solvent evaporation effect on the flow behavior of polymer solutions used to fabricate isoporous asymmetric membranes. Three different A-B-C triblock copolymer were evaluated: polyisoprene-*b*-polystyrene-*b*-poly(4-vinylpyridine) (ISV); polyisoprene-*b*-polystyrene-*b*-poly(*N,N*-dimethylacrylamide) (ISD); and polyisoprene-*b*-polystyrene-*b*-poly(*tert*-butyl methacrylate) (ISB). The resulting evaporation-induced microstructure showed a solution viscosity and film viscoelasticity strongly dependent on the chemical structure of the triblock copolymer molecules.

Furthermore, basic shear rheometry, flow birefringence, and advanced flow-velocimetry are used to deconvolute the flow-microstructure relationships of concentrated surfactant solutions. Sodium laureth sulfate in water (SLE<sub>1</sub>S) was used to replicate spherical, worm-like, and hexagonally packed micelles and lamellar structures. Interesting findings demonstrated that regular features of flow curves, such as power-law shear thinning behavior, resulted from a wide variety of experimental artifacts that appeared when measuring microstructured fluids with shear rheometry.

Finally, the successful integration of shear rheometry to calculate essential parameters to be used in a cost-effective visualization technique (still in development) used to calculate the dissolution time of polymers is addressed. The use of oscillatory rheometry successfully quantify the viscoelastic response of polyvinyl alcohol (PVA) solutions and identify formulations changes such as additive addition. The flow behavior of PVA solutions was correlated to dissolution behavior proving that the developed protocol has a high potential as a first screening tool.

## 1. INTRODUCTION

The understanding and control of flow behavior are of paramount importance to advance in the design of the new generation of soft materials. Often, the successful introduction of new products to a market comes from the ability to design the right rheological response for a specific production process and end-use. <sup>1</sup> For instance, successful thin film casting relies on the tailored rheological properties of a fluid that will suffer different shear regimes while transforming into a solid sheet without defects. <sup>2</sup> Other examples such as consumer cleaning products rely on the tailored rheological behavior to have enough fluidity while dosing yet remain thick enough to stay without running and perform adequately in the body. <sup>3</sup>

However, the implementation of experimental rheological frameworks to drive business decisions is challenging because the majority of soft materials do not flow according to the ideal elastic (Hookean) or ideal liquid (Newtonian) theories of rheology; they are “complex fluids.” <sup>4</sup> Complex fluids are microstructured materials with coexisting phases of very different length scales (nm to  $\mu\text{m}$ ) such as individual solvent molecules, surfactant and polymer assemblings, oil-water droplets, and solid micro-aggregates. <sup>5</sup> While the bulk flow of simple fluids (single phase) such as dilute solutions or dilute suspensions is a straightforward consideration of a single internal friction coefficient, the characterization of microstructured fluids (multiphase) is more challenging. <sup>6</sup> Instead of performing only as an ideal solid or liquid, microstructured fluids exhibit a rheological response denominated viscoelastic. <sup>7</sup>

Viscoelastic behavior is the combination of elastic and viscous rheological character. <sup>8</sup> The viscoelastic behavior of microstructured fluids has been densely studied, but no consensus has been reached because small changes in their microstructure generate different responses to variables such as applied stress, testing time and history of deformation. <sup>9</sup> <sup>7</sup> Therefore, many of the documented developments in rheology of microstructured fluids focused on specific materials and applications; that is the implementation of applied rheology.

Applied rheology pursues the discovery of fundamental relationships to bridge the empirical observations of flow and essential characteristics of the material. <sup>1</sup> For instance, applied rheology

protocols have been used to correlate human sensory perception to flow properties of food,<sup>10</sup> the fracture and self-healing energy to monomer formulation of gels,<sup>11</sup> the solids and electrolyte content to aging behavior of slurries,<sup>12</sup> among many others. A common denominator of these studies is the use of shear rheometry as measuring technique to quantify empirical rheological responses with an industrial focus.

Shear rheometry is preferred in applied rheology of microstructured fluids because it has a demonstrated success in the creation of frameworks to drive business decisions.<sup>13</sup> It can be easily used to elucidate different responses to deformation using a one-factor function such as viscosity (rotational testing) or a two-component function such as the complex shear modulus (oscillatory testing).<sup>14</sup> Besides, shear rheometry has a low operative cost and great versatility in integrating environmental and processing variables to measurements.<sup>15</sup> The above opens the opportunity for unmatched scientific and economic revenue.<sup>16</sup>

Regardless of the versatility of shear rheometry, The analysis of rheological data is sometimes overseen due to possible misinterpretations of the phenomenological events.<sup>17</sup> Shear rheometers blindly calculate rheological parameters based on assumptions such as the “no-slip” boundary condition, uniform laminar flow (simple shear), and quiescent relaxation upon shear cessation.<sup>18</sup> However, these assumptions are often violated during the study of microstructured fluids, as typical rheological responses of these materials often include a number of shear-induced flow instabilities and artifacts, including signatures of wall-slip, shear banding, and fluid fracture.<sup>19 20</sup>

Indeed, the unstable behavior of microstructured fluids coupled with the lack of physical feedback from standard rotational rheometers makes shear rheometry prone to report artifacts and misleading data. The challenge in using applied rheology is to create an experiment that offers scalable results with meaningful insights. Subsequently, to fully understand the rheological response of microstructured fluids used in industrial applications, it is essential to validate the rheological characterization with suitable and complementary rheo-physical measurements. It is not just about arbitrary quality control measurements.<sup>21</sup>

From the group of available rheo-physical measurements, rheo-flow velocimetry is a technique in which local velocities within a sample can be directly quantified along with the simultaneous collection of rheological data.<sup>22 23 24</sup> Rheo-flow velocimetry techniques used in rotational rheometers include, but are not limited to, magnetic resonance velocimetry (MRV),<sup>25</sup> particle image velocimetry (PIV),<sup>26</sup> laser Doppler velocimetry (LDV),<sup>27</sup> and ultrasonic speckle velocimetry (USV).<sup>28</sup> The balance between the material of interest, the technique operative cost, and technique resolution dictates the choice of technique. For instance, PIV and USV systems may have similar spatial and temporal resolutions and similar operative cost, but USV systems will perform best for opaque samples which the core base of the majority of fluids in industry.

This doctoral dissertation shows the development of three shear rheometry protocols in which a series of experiments attempt to portray substantial correlations between fluid microstructure, chemical composition, environmental factors, and rheological behavior of microstructured (complex) fluids with potential industrial applications.

## **1.1 Scope of this Dissertation**

The bulk of this document introduces the development of three protocols of applied shear rheology aimed to advance the transformation into real products of novel self-assembly block copolymers, concentrated surfactant solutions, and water-soluble polymers. All protocols measure relative physical and mechanical properties of fluids cost-effectively in concordance with industry demands. The main goal of this dissertation is to create a robust set of experimental evidence to bridge the mesoscopic signatures of each studied microstructure fluid to flow behavior and the mechanical, physical, and mass transfer phenomena related to processing or end-use.

The novelty of this work lies in the integration of simple rheological measurements, scattering characterization techniques, mass transfer measurements, and advanced rheo-flow velocimetry to draw meaningful conclusions relevant to each industrial application. The use of advanced rheo-flow velocimetry is critical because it elucidates the gray areas of performing shear rheometry measurements on microstructured fluids. Flow-velocimetry results contribute to the creation of awareness to areas where further and more in-depth analysis in fluid dynamics would be required to draw stronger conclusions.

The analysis of each chapter converges to the idea of deconvoluting the links between flow behavior of a microstructured fluid and their changing microstructure.

For instance, Chapter 2 introduces a combination of rotation and oscillatory shear rheometry with environmental control to correlate factors such as molecular chemistry, molecular mass, side-groups rotational energies, solvent-polymer affinity, long-range self-assembly, and solvent diffusional characteristics to flow behavior of a solvent evaporation-induced microstructure commonly found in triblock copolymer with a high potential to be the future of filtration applications. The results of this study show how molecular chemistry and polymer long-range self-assembly capabilities have the most substantial effect on the experimental rheological results.

Next, Chapter 3 introduces a combination of basic rheological experiments, rheo-flow velocimetry tests, and flow birefringence measurements to correlate factors such as surfactant concentration, ionic strength, micellar assembly, inter-lamellae spacing and domain elasticity to the rheological response and flow instability formation of shear-induced microstructures most commonly found in liquid soaps and other consumer care products. The results of this study show that common features of flow curves such as shear thinning behavior resulted from a wide variety of material responses including shear-induced wall-slip in micellar samples and plug flow in hexagonal and lamellar samples.

Finally, Chapter 4 (still work in progress) introduces a combination of basic rheological experiments and mass transfer observations to correlate factors such polymer concentration, plasticizer addition, and inter-and intra-hydrogen bonding disruption to the flow behavior of a penetrating solvent-induced microstructure most commonly found in water-soluble polymers with potential use for smart packaging. The results of this study show efficiency of the work-flow to calculate dissolution times creating the opportunity to use the presented protocol as a screening tool for an initial decision-making exercise over considerable changes in the formulation of possible water-soluble polymers.

By the end of the document, the reader should have a better understanding of the different chemical, physical, and thermodynamical factors that dominate the correlation between the rheological behavior and external factors that induced microstructural changes in of microstructured fluids (solvent evaporation, shear deformation, and solvent penetration).

## 1.2 Basics of Rheology

Rheology is a branch of physics that study and describe the deformation of materials in terms of the extent, orientation and application time of an applied force. Principally, rheology uses measurable variables such as the applied stress, the extent of deformation (strain), the deformation rate (strain rate), and the ratios between stress-strain (modulus) and stress-strain rate (viscosity) to mathematically model the internal resistance to flow of materials.<sup>29</sup>

The foundations of rheology are the Hookean ideal solid and the Newtonian ideal liquid. Hooke described the intrinsic properties of solids using the stress ( $\tau$ ) as a linear function of deformation ( $\gamma$ ) times a constant of proportionality called elastic modulus ( $G$ ) [ $\tau = G\gamma$ ]. Newton described the intrinsic properties of an ideal liquid using the stress ( $\tau$ ) as a linear function of the strain rate ( $\dot{\gamma} = \frac{d\gamma}{dt}$ ) times a constant of proportionality called viscosity [ $\tau = \eta\dot{\gamma}$ ]. These laws can model many real solid materials such as metals and ceramics and liquids such as water and oils. However, the majority of microstructured materials used in industry fall in between both ideal behaviors. These usually show a non-linear dependency between stress and strain rate such as thinning [ $\tau = k\dot{\gamma}^n$ ;  $n < 1$ ], thickening [ $\tau = K\dot{\gamma}^n$ ;  $n > 1$ ], and yield behaviors [ $\tau = \tau_o + \eta\dot{\gamma}$ ] as illustrated in Figure 1-1. Then, the actual terminology to use is materials with viscoelastic responses.<sup>18</sup>

Viscoelasticity is the time-dependent rheological response of materials. The most didactic form to illustrate viscoelastic behavior is to describe the deformation of silly putty. If a ball made of silly putty is thrown fast at a solid surface, the ball will bounce back immediately as an elastic material. However, if the same ball rest on the surface of a counter for more extended periods, the putty sags to a completely flat shape flowing like a viscous liquid. The material is the same, but the timescales used for deformation are different.

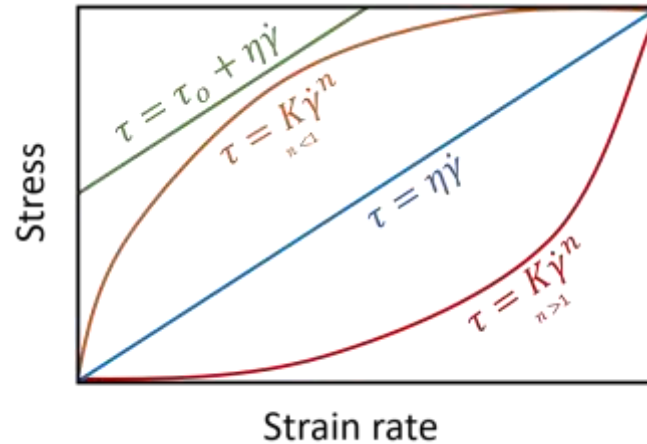


Figure 1-1 Typical rheological behaviors. Stress as a function of strain rate of Newtonian (blue), shear thinning (orange), shear thickening (red) and yield (green) fluids.

However, the extent of individual solid and liquid characters in a viscoelastic behavior is better understood using the Maxwell spring-dashpot model presented in Figure 1-2. In this element, two components with the freedom to deflect from each other are connected in series. The spring with elastic modulus  $G$  represents the ideal solid component (Hooke's law). The dashpot containing a Newtonian liquid of viscosity  $\eta$  represents the ideal viscous component (Newton's law).

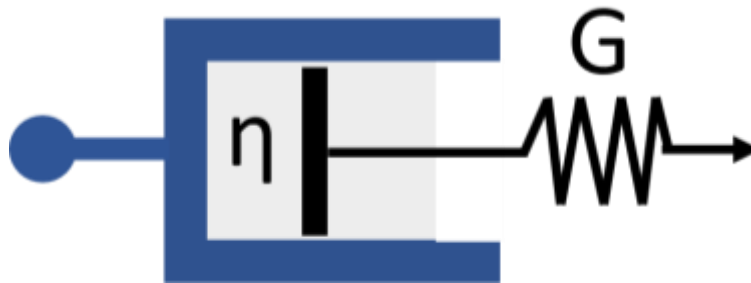


Figure 1-2 Maxwell spring-dashpot model. Graphical representation of the Maxwell model for viscoelastic behavior. The liquid in dashpot has a viscosity  $\eta$  and spring has an elastic modulus  $G$ . Consider an application of a constant force in the direction of the arrow to the element shown in Figure 1-2. When the force is initially applied the spring will deform (dashpot does not) until the spring reaches a constant deformation. Immediately after, the spring will pull the piston at a constant rate of deflection. This movement continues (at a steady rate) as long as the force is applied. Once the application of force stops, the spring recoils elastically to its initial position, but the dashpot never recovers its initial position. The amount of strain recovered by the spring is proportional to the elastic energy stored by the Maxwell element, and the unrecovered strain of the

dashpot is proportional to the lost energy during the process of deformation of the Maxwell element.

### 1.3 Basics of Shear Rheometry

Rheometry is the core base technique used in this dissertation to quantify rheological behaviors of microstructured fluids. Shear rheometers are of relative importance to carry on with these measurements because they offer great versatility and low operative cost. Shear rheometers are drag flow machines that measure the resistance to flow of a thin film of fluid placed in between a moving and stationary wall. The torque to produce a deflection is measured (or vice-versa) to calculate rheological constants such as viscosity or complex modulus.<sup>14</sup> Importantly, the selection of the geometry to perform the measurement depends on the type of test to perform and viscoelastic nature of the specimen to analyze. Figure 1-3 presents the most typical geometries used in shear rheometers: concentric cylinders, cone, and plate and parallel plates.

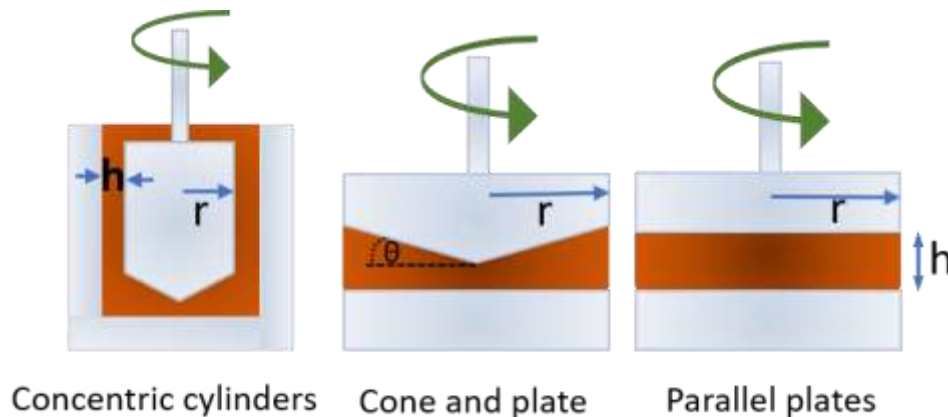


Figure 1-3 . Shear rheometry most popular geometries to measure the flow of simple and microstructured fluids. Dimensions are not at a scale

Concentric cylinders comprise the basis of the beginnings of rotational rheometry. The small thin film of fluid is placed in between a moving rotor and a static cup. This geometry is very useful for fluids with low to moderate viscosity and offers excellent protection to the specimen from environmental conditions. The curvature of concentric cylinders is not considered an issue as the gap is narrow and the conical bottom design matches the shear rates of the gap. Some of the limitations of concentric cylinders are the development of secondary flows at high shear rates due

to the effects of fluid inertia and the need for a large volume of sample. Besides, concentric cylinders are generally used to measure flow properties under rotational deformation. Oscillatory testing is limited using this geometry due to instrument inertia effects.<sup>29</sup>

The cone and plate geometry is modified version of parallel plate geometry. The angle of the cone plays an essential role in equalizing the effects of fluid velocity and gap respect to distance from the center of the geometry. This geometry exerts a uniform bidirectional shear within the thin film of fluid for improved and more uniform measurements. Cone and plate geometry is suitable to measure low to moderate viscosity fluids. It is not recommended for suspensions with a particle size equal to or greater than 1/10 the truncation gap of the cone (minimum distance from the center of the cone to the plate). Different than concentric cylinders, cone and plate expose the sample to the environment. This geometry is used in oscillatory experiments, and it is not entirely recommended for rotational experiments at very high angular velocities because inertial forces drive the specimen out of the gap.<sup>18</sup>

Finally, the parallel plates geometry. It is the most versatile tool presented in Figure 1-3. Different than the cone and plate, and the concentric cylinders, the shear conditions in parallel plates can be adjusted by varying the gap between plates [ $\dot{\gamma} = v/h$ ]. The adjustable gap also allows for an easy protocol to load specimens, thus all kind of fluids (low to very high viscosity) are tested using this geometry. With no truncation gap, the sensitivity to particle size is adjustable. However, the flat surfaces produce an uneven shear condition in the radial direction of the geometry. Usually, the reported strain data (maximum strain) belongs to the outer rim of the plate. Also, torque responses are mainly from the outer ring of the plates. As well as cone and plate, parallel plates expose the samples to environmental conditions. Also, parallel plates are not the first choice for rotational experiments as inertial forces drive the sample out of the gap.<sup>14</sup>

In terms of testing approaches, rheological behaviors are quantified using different procedures that result from the applied deformation; continuous (rotational) or dynamic (oscillatory) deformation (strain).

The microstructure of fluid is extensively disturbed when applying rotational deformation. Therefore, the resistance to flows of the specimen is correlated to one-component rheological

function such as viscosity. The viscosity response is a function of the level of strain and strain rate. Simple and Newtonian fluids will show a constant function of viscosity, but microstructured fluids usually depict a time-dependent function as shown in Figure 1-1. The universal test in the industry is the flow curve (the stress response as a function of strain rate). During this test, stress or strain is applied in the form of constant values, logarithmic ramps, or constant ramps. The best approach to reach a steady state measurement is the application of a list of constant values or the slow increasing logarithmic ramps. <sup>14</sup>

Conversely, oscillatory deformation is useful to correlate the internal resistance to flow to a two-component rheological function such the complex modulus. This approach is more suitable to study viscoelasticity. From the different available options, this document uses elaborated experiments considering linear viscoelasticity with sinusoidal deformations. Linear viscoelasticity uses small deformations to ensure an undisturbed state of the microstructure where only spontaneous rearrangements (relaxations) are reflected in the stress response. The range for small deformations where the stress is independent of strain is called the linear viscoelastic regime.

The stress or strain are applied in the form of sinusoidal waves. Both will respond to another like waves of the same frequency but shifted by a phase angle ( $\delta$ ). This deconvolution leads to the derivation of two dynamic moduli; the storage modulus  $G'$  and viscous modulus  $G''$ .  $G'$  represent the elastic component of deformation: the stored energy for immediate recovery upon strain cessation. Conversely,  $G''$  represents the viscous component of deformation: the energy lost in the form of heat.  $G'$  and  $G''$  compose the complex modulus which magnitude is given by  $[|G^*| = (G'^2 + G''^2)^{1/2}]$ . Both moduli tell the story about the microstructural arrangement of the specimen to dynamic deformation using  $\tan \delta = G''/G'$ . For  $\tan \delta \gg 1$ ,  $G'' > G'$  so the fluid behaves more liquid than solid. For  $\tan \delta \ll 1$ ,  $G' > G''$  so the fluid behaves more solid than liquid. Finally, using both dynamic moduli, the stress response can be expressed as a function of frequency ( $w$ ), a constant strain ( $\gamma_0$ ) and the elastic and viscous characters  $[\tau = \gamma_0(G' \sin wt + G'' \cos wt)]$ . <sup>5</sup>

## 1.4 Basics of Ultrasonic Speckle Velocimetry

Elucidate the presence of shear-induced flow instabilities (most common shown in Figure 1-4) is essential to avoid significant complications during the interpretation of shear rheometry data. Traditional shear rheometers lack of physical feedback of the flow conditions within the volume of the sheared specimen. Thus, the presence and root cause of instabilities in microstructured fluids are unrevealed using traditional shear rheometry but, rheo-flow characterization techniques can help to visualize the formation of mesoscopic domains with distinct local velocities and strain localization.<sup>30 31</sup>

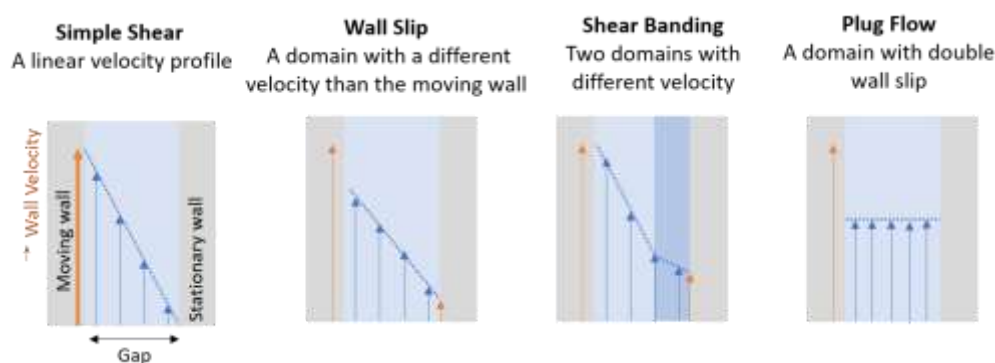


Figure 1-4 Representation of steady flow and most common flow instabilities as one-dimensional velocity profiles. Classical representation of a sheared fluid within a moving and stationary plate.

In this dissertation, a rheo-flow velocimetry characterization technique able to provide a one-dimensional velocity profile of an opaque specimen is coupled to the standard shear rheometry to deliver the physical feedback that validates the veracity of the analysis of rheological measurements.

Ultrasonic speckle velocimetry (USV) is a measurement technique that uses a complex, high frequency backscattered ultrasonic signal to resolve the velocity and position of contrast agents within the volume of a deforming specimen, hence indirectly obtaining the one-dimensional velocity profile of the specimen. Local velocity measurements are achieved by using highly sophisticated electronic equipment as illustrated in Figure 1-5. The details of the physical set up used at Purdue University are provided in Chapter 3 section 3.2.3. A brief overview of this technique is provided here; a more in-depth description of this system is given elsewhere.<sup>22 32</sup>

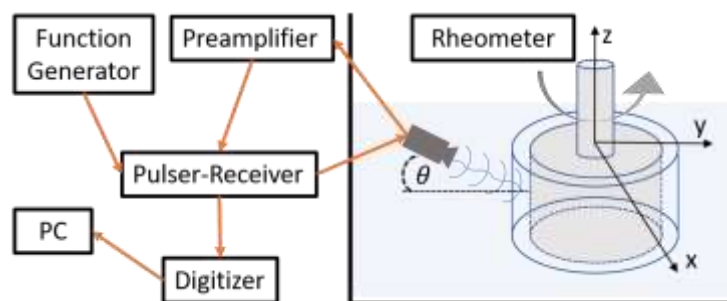


Figure 1-5 USV electronic equipment illustration on the shear rheometer

The measurement process begins with the emission of an ultrasonic pulse and the reception of the respective echo. Pulses are generated with a user-defined pulse repetition frequency (PRF) that is selected based on the shear rate of the experiment – higher PRF values are required for high applied shear rates. Pulses and echoes exist in distinct times, allowing one ultrasonic transducer to perform as both emitter and receiver. Echoes are generated from the interaction between the ultrasonic pulses and contrast agents (here, 11  $\mu\text{m}$  hollow glass spheres). During data post-processing, a cross-correlation algorithm uses two consecutive echoes to determine the delay in time. The delay time between a pair of echoes and the geometrical constants of the physical hardware provide sufficient information to obtain the position within the rheometer gap and the radial velocity of a given contrast agent. Theoretically, only two pulses are needed to determine the velocity of an agent; however, in this experiment, 1,000 pulses divided into 1,000 segments are collected to provide statistical meaning to the calculated velocity values. The geometrical calibration of the hardware is achieved by using a Newtonian liquid, *e.g.*, reverse osmosis water seeded with contrast agents. The velocity of sound used in this experiment is obtained from separate time-of-flight measurements.

## 1.5 References

1. Eley RR. *Applied Rheology in the Protective and Decorative Coatings Industry.*; 2005. <http://www.bsr.org.uk>. Accessed March 27, 2019.
2. Peressini D, Bravin B, Lapasin R, Rizzotti C, Sensidoni A. Starch-methylcellulose based edible films: Rheological properties of film-forming dispersions. *J Food Eng.* 2003;59(1):25-32. doi:10.1016/S0260-8774(02)00426-0

3. Boyd J V. Psycho-rheology the relevance of rheology to consumer acceptance. *J Soc Cosmet Chem.* 1976;27:247-256.  
<http://citeseerx.ist.psu.edu/viewdoc/download?doi=10.1.1.513.914&rep=rep1&type=pdf>. Accessed March 18, 2019.
4. Gelbart WM, Ben-Shaul A. The “New” Science of “Complex Fluids.” *J Phys Chemistry.* 1996;100(31):13169-13189. doi:10.1021/jp9606570
5. Larson RG. *The Structure and Rheology of Complex Fluids (Topics in Chemical Engineering)*. Oxford University Press; 1999.
6. Larson RG. The rheology of dilute solutions of flexible polymers: Progress and problems Ronald. *J Rheol (N Y N Y)*. 2005;49(1):1-70. doi:10.1122/1.1835336
7. Chen DTN, Wen Q, Janmey PA, Crocker JC, Yodh AG. Rheology of Soft Materials. *Annu Rev Condens Matter Phys* 2010. 2010;1:301-322. doi:10.1146/annurev-conmatphys-070909-104120
8. Fernandez-Nieves A, Manuel-Puertas A. *Fluids, Colloids, Soft Materials, and an Introduction to Soft Matter Physics*. (Fernandez-Nieves A, Manuel-Puertas A, eds.). Hoboken, New Jersey: John Wiley & Sons, Inc.; 2016.  
<http://www.wiley.com/go/permission.www.wiley.com>. Accessed January 8, 2019.
9. Roux D, Nallet F, Diat O. Rheology of Lyotropic Lamellar Phases. *Europhys Lett.* 1993;24(1):53-58. doi:10.1209/0295-5075/24/1/009
10. Jack FR, Paterson A, Piggott JR. Relationships between rheology and composition of Cheddar cheeses and texture as perceived by consumers. *Int J Food Sci Technol.* 2007;28(3):293-302. doi:10.1111/j.1365-2621.1993.tb01275.x
11. Thornell TL, Subramaniam K, Erk KA. The impact of damage accumulation on the kinetics of network strength recovery for a physical polymer gel subjected to shear deformation. *J Polym Sci Part B Polym Phys.* 2016;54(17):1693-1701.  
doi:10.1002/polb.24071
12. Abu-Jdayil B. Rheology of sodium and calcium bentonite–water dispersions: Effect of electrolytes and aging time. *Int J Miner Process.* 2011;98(3-4):208-213.  
doi:10.1016/J.MINPRO.2011.01.001
13. Fischer P, Windhab EJ. Rheology of food materials. *Curr Opin Colloid Interface Sci.* 2011;16:36-40. doi:10.1016/j.cocis.2010.07.003

14. Mezger TG. *The Rheology Handbook: For Users of Rotational and Oscillatory Rheometers*. Vincentz Network GmbH & Co KG; 2006.  
<https://books.google.com/books?id=N9Fdn0MEIDIC&pgis=1>. Accessed November 3, 2015.
15. Malkin AI, Isayev AI. *Rheology : Concepts, Methods, and Applications*. ChemTec Pub; 2012.
16. Barnes HA. An examination of the use of rotational viscometers for the quality control of non-Newtonian liquid products in factories. *Appl Rheol*. 2001;11(2):89-101.  
<http://www.appliedrheology.org>. Accessed March 18, 2019.
17. Divoux T, Fardin MA, Manneville S, Lerouge S. Shear Banding of Complex Fluids. *Annu Rev Fluid Mech*. 2016;48:81-103. doi:10.1146/annurev-fluid-122414-034416
18. Macosko CW. *Rheology: Principles, Measurements, and Applications*. Vol 41. Wiley-Blackwell; 1995. doi:10.1002/aic.690411025
19. Larson RG. Instabilities in viscoelastic flows. *Rheol Acta*. 1992;31(3):213-263.  
doi:10.1007/BF00366504
20. Wyss HM. Rheology of soft materials. *Fluids, Colloids Soft Mater An Introd to Soft Matter Phys*. 2018:149-164. doi:10.1002/9781119220510.ch9
21. Eley R. Applied Rheology. *British society Rheol*. 2005:173-240. <http://www.bsr.org.uk>. Accessed March 19, 2019.
22. Manneville S, Becu L, Colin A. High-frequency ultrasonic speckle velocimetry in sheared complex fluids. *Eur Phys J Appl Phys*. 2004;28(3):361-373. doi:10.1051/epjap:2004165
23. Divoux T, Barentin C, Manneville S. From stress-induced fluidization processes to Herschel-Bulkley behavior in simple yield stress fluids. *Soft Matter*. 2011;7(18):8409.  
doi:10.1039/c1sm05607g
24. Herle V, Manneville S, Fischer P. Ultrasound velocimetry in a shear-thickening wormlike micellar solution: Evidence for the coexistence of radial and vorticity shear bands. *Eur Phys J E*. 2008;26(1-2):3-12. doi:10.1140/epje/i2007-10304-3
25. Poelma C. Ultrasound Imaging Velocimetry: a review. *Exp Fluids*. 2017;58(1):3.  
doi:10.1007/s00348-016-2283-9

26. Dimitriou CJ, Casanellas L, Ober TJ, McKinley GH. Rheo-PIV of a shear-banding wormlike micellar solution under large amplitude oscillatory shear. *Rheol Acta*. 2012;51(5):395-411. doi:10.1007/s00397-012-0619-9
27. Shapley NC, Armstrong RC, Brown RA. Laser Doppler velocimetry measurements of particle velocity fluctuations in a concentrated suspension. *J Rheol (N Y N Y)*. 2002;46(1):241-272. doi:10.1122/1.1427908
28. Manneville S, Colin A, Waton G, Schosseler F. Wall slip, shear banding, and instability in the flow of a triblock copolymer micellar solution. *Phys Rev E - Stat Nonlinear, Soft Matter Phys*. 2007;75(6):1-11. doi:10.1103/PhysRevE.75.061502
29. Chhabra RP, Richardson JF. *Non-Newtonian Flow and Applied Rheology : Engineering Applications*. 2nd ed. Butterworth-Heinemann/Elsevier; 2008. doi:10.1016/B978-0-7506-8532-0.X0001-7
30. Fardin MA, Ober TJ, Grenard V, et al. Interplay between elastic instabilities and shear-banding: three categories of Taylor-Couette flows and beyond †. *Soft Matter*. 2012;8:10072. doi:10.1039/c2sm26313k
31. Divoux T, Barentin C, Manneville S. Stress overshoot in a simple yield stress fluid: An extensive study combining rheology and velocimetry. *Soft Matter*. 2011;7(19):9335-9349. doi:10.1039/c1sm05740e
32. Bice JE. Using Ultrasonic Speckle Velocimetry to Detect Fluid Instabilities in a Surfactant Solution. 2017;(December).

## **2. RHEOLOGICAL AND MECHANICAL CHARACTERIZATION OF EVAPORATION-INDUCED MICROSTRUCTURES: THE CASE OF SELF-ASSEMBLY BLOCK COPOLYMERS**

Portions of the following chapter contain text or figures adapted with permissions from Caicedo-Casso, E., Sargent, J., Dorin, R. M., Wiesner, U. B., Phillip, W. A., Boudouris, B. W. and Erk, K. A. (2019), A rheometry method to assess the evaporation-induced mechanical strength development of polymer solutions used for membrane applications. *J. Appl. Polym. Sci.*, 136, 47038. doi: 10.1002/app.47038

### **2.1 Introduction**

The self-assembly and non-solvent induced phase separation (SNIPS) method is an innovative fabrication technique for block copolymer-based filtration devices.<sup>1 2 3 4</sup> SNIPS can be used to create filtration membranes with a hierarchical tapered structure.<sup>5</sup> A periodically-ordered structure in the top layer offers effective separation of solutes from the solvent. This layer is the result of block copolymer assembly and exhibits a well-ordered structure with a high density of uniform nanoscale pores.<sup>3</sup> In the bottom layer, an asymmetric substructure mechanically supports membrane, allowing the membrane to withstand the stresses experienced by the film during the process of filtration.<sup>6 7 8 9</sup> This support layer also facilitates a rapid passage of solvent through an asymmetric macro-void structure, which minimizes the fluid drag resistance during practical membrane operation.<sup>10</sup>

The SNIPS method consists of the preparation of a polymer solution, then the casting of the polymer solution into a film, followed by a controlled solvent evaporation step, before a rapid solvent to non-solvent exchange that is used to precipitate the polymer and create the final nanoporous membrane.<sup>11</sup> The necessary components of the SNIPS process are the self-assembled block copolymer, a mixed solvent system to prepare the polymer solution, and a non-solvent bath. The block copolymer and the components of the solvent mixture interact with each other to create the selective layer via self-assembly upon solvent evaporation. Upon phase inversion induced by the non-solvent bath (i.e., polymer-solvent de-mixing), the non-equilibrium structures of selective and support layers precipitate from solution.<sup>12</sup>

The high solute selectivity, as well as the high solvent permeability, are key properties of SNIPS membranes to outperform current commercial materials.<sup>7 4 9</sup> However, one of the significant challenges towards the creation of a commercial SNIPS filtration membrane is to manufacture these materials by continuous casting techniques (e.g., a roll-to-roll process).<sup>7</sup> To create a scalable SNIPS process, it is necessary to adapt SNIPS to the manufacturing environment and, precisely, the film translation steps that occur during roll-to-roll casting.

Research focused on membranes created through the combination of self-assembly and phase inversion has concentrated on the interrelationship of the molecular architecture with the final membrane morphology and separation performance.<sup>6</sup> Mechanisms regarding the self-assembly process and final assembled morphology have been proposed by Dorin, et al.,<sup>6</sup> Sargent, et al.,<sup>7</sup> Gu, et al.,<sup>13</sup> and Rangou, et al.<sup>14</sup> Also, the effect of relative humidity over the final assembled morphology have been elucidated by Li, *et al.*<sup>15</sup>

Hypotheses have been proposed in order to correlate the solvent evaporation rate to the orientation of the self-assembled cylinders.<sup>16 17</sup> Phillip, *et al.* stated that a relatively fast solvent evaporation rate is necessary to obtain the nucleation and continuous growth of perpendicular-to-surface orientated cylinders. Thus, necessary and allowable evaporation windows are different for every polymer-solvent combination used in SNIPS. Only the right combination of chemistry and selective solvent under an adequate evaporation window and evaporation rate lead to a perpendicular-to-surface oriented cylinder structure or a cubic arrangement of channels useful in filtration applications.<sup>1 5 13 18</sup>

Despite the extensive research on molecular architecture and final morphology, there is no information about the effect of new roll-to-roll variables such as convection, shear stresses, and film deformation on the critical factors that define the success of a scalable SNIPS method.<sup>19</sup> Consequently, preliminary roll-to-roll casting experiments were performed to understand the complexity of such effects visually. The results of the preliminary casting that are shown in Figure 2-1 suggested that the casting of SNIPS membranes using roll-to-roll was feasible, but much understanding of rheology of the polymer solution was needed. The change in opacity of the cast film shown in Figure 2-1a suggested that phase separation was successful, but defects on the film

surface suggested that film casting uniformity success will first depend on the mechanical development of the cast film.

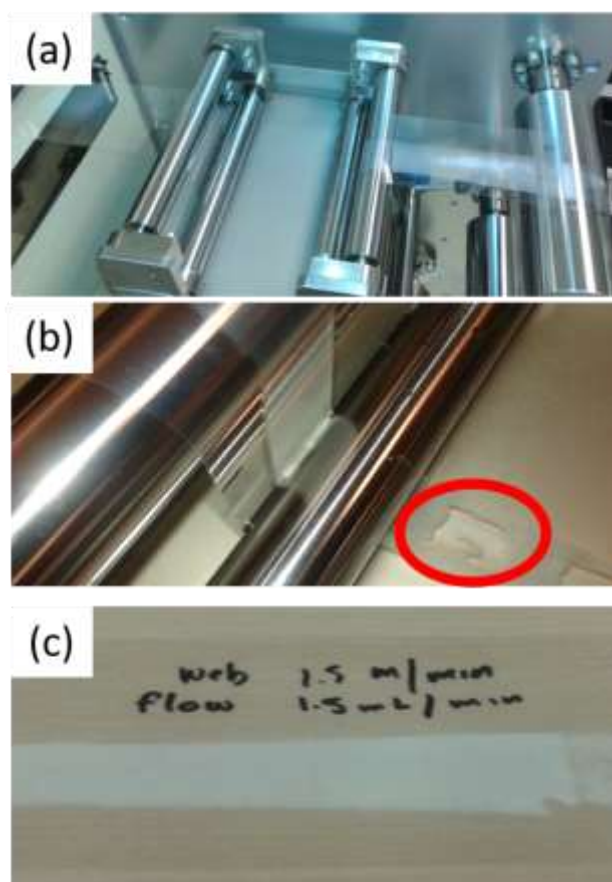


Figure 2-1 Preliminary attempts of producing SNIPS membranes through roll-to-roll casting. (a) Web film opacity change after passing the non-solvent bath (b) peeling defects due to rollers contact on a wet film with low mechanical strength (c) example of a uniform cast section. Author source.

The literature showed that continuous growth of the selective layer of a SNIPS membrane depends on the ability of the solvent to diffuse through a polymer matrix.<sup>16 20</sup> However, the success of a scalable roll-to-roll SNIPS process not only will depend on the successful assembly of polymer on the surface. The success will start with the ability of a SNIPS cast film of preserving the desired morphology over the time before non-solvent exchange. That is, the physicochemical nature of the selective layer is as essential as its viscoelastic properties.<sup>20</sup> Consequently, elucidating the viscoelastic behavior of the block copolymers and the solvent evaporation effects at early stages is imperative to accurately translate the SNIPS membrane from the laboratory scale to a commercial-scale product.

The viscoelastic behavior is typical of all polymeric materials.<sup>21</sup> The polymers used in SNIPS membrane fabrication are expected to show a rheological viscoelastic behavior similar to those of associative block copolymers.<sup>22,23</sup> Associative block copolymers assemble in regular and diverse structures creating unique intermolecular interactions (bridges) that are dependent on the physicochemical nature of the block copolymer – solvent system.<sup>22,24</sup> The amount and lifetime of the individual or cumulative bridges define the viscoelastic behavior of associative polymers.<sup>22</sup> Higher numbers and lifetimes of the bridges suggest higher viscosities and greater solid-like behavior. Consequently, it is expected that phase separation due to solvent evaporation in a particular polymer system produces a unique intermolecular interaction that can be observed in the evolution of the viscoelastic behavior of SNIPS polymer solutions. The evolution of the viscoelasticity can be seen as the transition from liquid-like to solid-like rheological behavior.<sup>25</sup> Out of all available methods to measure the viscoelastic evolution of a thin film of solution, the most suitable method in this case, where the solvent is allowed to evaporate, is dynamic sinusoidal oscillations within a small strain experimental range. The above choice is made because the method preserves the integrity of the sample such that the effects of solvent evaporation can be isolated.<sup>21</sup>

This chapter describes the first protocol created in this dissertation. The current protocol uses shear rheometry measurements to directly quantify the flow behavior and the effect of solvent evaporation over the mechanical strength development of polymer solutions used to produce SNIPS membranes. A relationship between the factors (molecular chemistry and solvent evaporation) of developing microstructures and their viscoelastic response is demonstrated. Rotational shear experiments are used to quantify the flow behavior under shear deformation of most common polymer systems, and oscillatory shear experiments are applied to elucidate the mechanical development of SNIPS solutions upon solvent evaporation.

## 2.2 Materials and Experimental Methods

### 2.2.1 Triblock copolymer samples

Polyisoprene-*b*-polystyrene-*b*-poly(4-vinylpyridine) (ISV), Polyisoprene-*b*-polystyrene-*b*-poly(*tert*-butyl methacrylate) (ISB) and polyisoprene-*b*-polystyrene-*b*-poly(*N,N*-dimethylacrylamide) (ISD) were the triblock copolymer samples used in this experiment. Figure 2-2 presents their chemical structures.

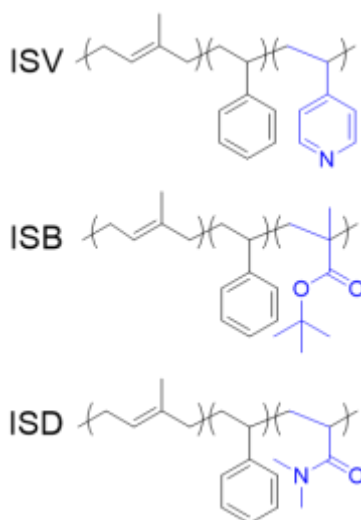


Figure 2-2 Triblock copolymer molecular structures for: polyisoprene-*b*-polystyrene-*b*-poly(4-vinylpyridine) (ISV), polyisoprene-*b*-polystyrene-*b*-poly(*tert*-butyl methacrylate) (ISB), and polyisoprene-*b*-polystyrene-*b*-poly(*N,N*-dimethylacrylamide) (ISD).

Table 2-1 reports the physical and chemical characteristics of each sample, showing that all three polymers exhibit similar overall molar mass and dispersity ( $\mathbf{D}$ ) values. These are tailored block copolymers; their synthesis methods and full characterization are reported by Phillip, *et al.*,<sup>18</sup> (ISV), Caicedo-Casso *et al.*,<sup>26</sup> (ISB), and Mulvenna, *et al.*,<sup>3</sup> (ISD).

Table 2-1. Composition of the polymers investigated in this study.

A-B-C Block Polymer	$M_n$ (kg mol <sup>-1</sup> )	$\bar{D}$	Volume Composition (%) of A/B/C Moieties
ISV [polyisoprene- <i>b</i> -polystyrene- <i>b</i> -poly(4-vinylpyridine)]	43.0	1.02	27/55/18
ISB [polyisoprene- <i>b</i> -polystyrene- <i>b</i> -poly( <i>tert</i> -butyl methacrylate)]	40.1	1.50	24/41/35
ISD [polyisoprene- <i>b</i> -polystyrene- <i>b</i> -poly( <i>N,N</i> -dimethylacrylamide)]	42.3	1.40	21/43/36

## 2.2.2 Characterization

### 2.2.2.1 Rheometry with minimal evaporation

The flow behavior of ISV, ISB and ISD polymer solutions at three different polymer concentrations (9 wt.%, 12 wt.% and 15 wt.%) was studied using rotational shear rheometry. A rheometer (Anton Paar MCR702) paired with a 10 mm concentric cylinder fixture and solvent trap was selected to execute all rotational shear experiments with minimal to zero solvent evaporation. The volume of the samples used was 1.2 ml. In this experiment the polymer concentration was kept constant; therefore, the internal structure of the sample was only subject to changes induced by shear deformation. The shear rate was applied using logarithmic ramps to construct the flow profile. Steady state was reached using shear rate control and 3 seconds of data averaging at each measured point. The temperature was held constant at 22 °C over all experiments using a Peltier system.

For all rheological studies, the solid copolymer was dissolved using a solvent mixture of 70% 1,4-dioxane (DOX) (Sigma Aldrich) and 30% tetrahydrofuran (THF) (Fisher Scientific), by weight. The polymer solutions were magnetically stirred for 6 hours and allowed to degas overnight before testing.

### 2.2.2.2 Mechanical strength development upon solvent evaporation

The development of mechanical strength upon solvent evaporation from the ISV, ISB, and ISD polymer solutions was evaluated using oscillatory rheometry. The initial polymer concentrations were set to 9 wt.%, 12 wt.% and 15 wt.%. These concentrations changed with time due to solvent

evaporation. An ARG2 rheometer (TA Instruments) paired with 40 mm parallel plates fixture was used to allow solvent evaporation while measuring the apparent storage modulus ( $G'$ ) and apparent loss modulus ( $G''$ ) over time;  $G'$  and  $G''$  are reported as apparent properties because the composition of the film is not uniform and varies over the course of the experiment due to solvent evaporation. The gap between plates was 0.4 mm. The sample volume was 0.6 mL. Small amplitude oscillatory shear (SAOS) rheometry was imperative to isolate and quantify the solvent evaporation effects. Then, it was necessary to determine the linear viscoelastic range (LVR) to perform SAOS. An alternative approach to measure the LVR was used because a traditional experiment such as the amplitude sweep to determine the LVR would not be representative for the physical situation of a sample with a time-evolving viscosity. The new approach involved the use of a 15wt. % ISB solution and time sweeps at different strain values (0.1%, 0.5%, 1% and 2% strain). In this approach, it is assumed that the viscoelastic response of the specimen to dynamic strain is linear as long as the applied strain is within the LVR. Therefore, it is expected that an applied strain within the LVR would produce similar responses of  $G'$  and  $G''$ . The results of the new approach to determine the LVR suggested a strain of 0.5% and an oscillation frequency of 10  $\text{rad s}^{-1}$  as oscillatory parameters for all subsequent experiments. The temperature was held constant at 22 °C over all experiments using a Peltier system.

The quantification of the development of mechanical strength upon solvent evaporation was visualized using four parameters that were calculated from the oscillatory data: the initial slope, the plateau slope, the cross-over point, and the average  $G'$  plateau value. Linear regression over  $G'$  data for  $t < 30$  s was performed to calculate the initial slope. The initial slope offers an approximate measure of the formation rate of a viscoelastic film right at the edge of the parallel plates upon initial solvent evaporation. The plateau slope was calculated using linear regression over  $G'$  data for  $300 \text{ s} < t < 600 \text{ s}$ . The plateau slope can be used to quantify the rate of elasticity development of the viscoelastic film upon continuous solvent evaporation. The cross-over point was calculated via regression-extrapolation of the phase shift (*i.e.*,  $\tan \delta$ ) data close to a value of 1. The cross-over point displays the time at which the viscoelastic behavior of the sample changes from a predominantly viscous ( $G'' > G'$ ) to an elastic response ( $G' > G''$ ). The average  $G'$  data for  $t > 300$  s was used to define the average  $G'$  plateau. The average  $G'$  plateau is an approximation of the possible value of the maximum elastic strength of a SNIPS-cast film before the non-solvent

exchange step with the solvent. Note that all four parameters are graphically illustrated in Figure 2-3.

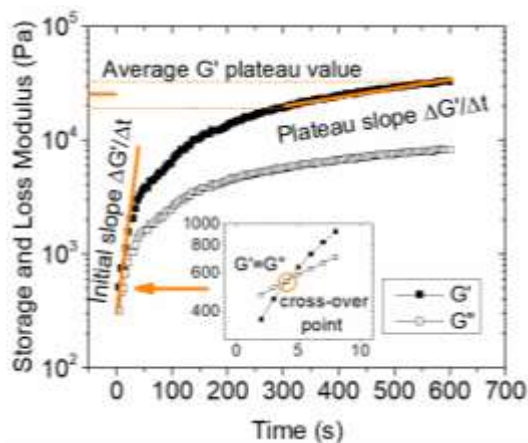


Figure 2-3. Illustration of the four parameters calculated from the oscillatory test upon solvent evaporation (0.5% strain and  $10 \text{ rad s}^{-1}$  angular frequency).

### 2.2.2.3 Solvent evaporation rate

The diffusion coefficient of the solvent through the cast polymer film was calculated by measuring the change in mass over time of cast films as graphically shown in Figure 2-4. Blade casting was used to produce a film with an enclosed area of  $5 \text{ cm}^2$  and a thickness of  $382 \text{ }\mu\text{m}$  on a glass surface. The specimen was massed on an Acculab ALC-210.4 scale with a maximum mass measurement of  $210 \text{ g}$  and accuracy up to  $0.0001 \text{ g}$ . The change in mass over time data was recorded over 15 minutes.

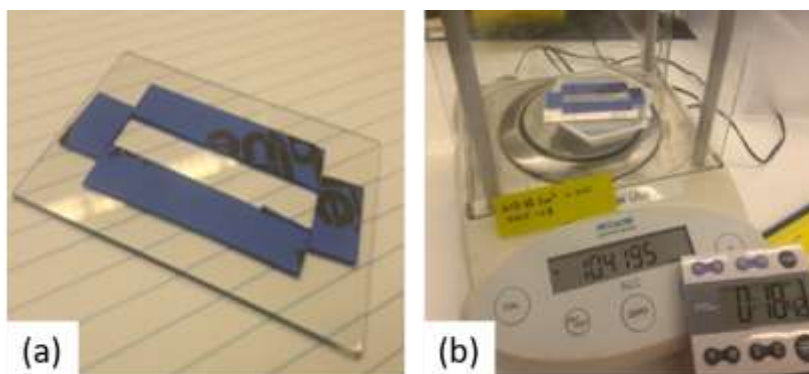


Figure 2-4. Illustration of the physical set-up used to measure the diffusion coefficient of solvent through cast polymer films.

The ability of the solvent to evaporate from a cast film was related to the resistance that the solvent encounters to diffuse from the bulk solution to the solution-gas interface with similar analysis previously reported.<sup>16</sup> The change in mass of a cast film can be related to solvent diffusivity through a solidifying film using Equation 2-1.<sup>27 28</sup>

Equation 2-1. Steady diffusion mass transfer correlation of an evaporating solvent at the polymer solution-air interface.

$$\frac{M_0 - M}{A_m} = \sqrt{2Dt} c_B$$

The parameters of Equation 2-1 are defined as the instantaneous mass ( $M$ ), the initial mass ( $M_0$ ), the evaporation area ( $A_m$ ), the diffusion coefficient ( $D$ ), time ( $t$ ), and the bulk solvent concentration ( $C_B$ ). Equation 2-1 is a 1D model considered valid due to the relatively thin film compared to the large cross-sectional area (steady state Fickian diffusion)<sup>29</sup>. Convection terms are not included in the derivation of Equation 2-1 because the solvent mass transport in the gas phase is not considered to be the limiting factor for solvent diffusion.<sup>16</sup> The constant change in mass of a cast film of a specific evaporation area is compared to the square root of time. As a result, the diffusion coefficient of the solvent within a polymer film can be calculated via linear regression methods.

## 2.3 Results

### 2.3.1 Rheometry results with minimal evaporation

Figure 2-5a displays a schematic of the rotational test set up and Figure 2-5b shows the viscosity curve results for the ISV, ISB, and ISD solutions at 15 wt.%, under minimal evaporation effects. The viscosity behavior under rotational shear of all three solutions corresponds to a Newtonian behavior within the range of the studied shear rates. Despite the Newtonian response, the three solutions exhibited different values of Newtonian viscosity. The ISV ( $70 \text{ mPas}^{-1}$ ) and ISD ( $14 \text{ mPas}^{-1}$ ) solutions showed the highest and lowest viscosity, respectively. The ISB solution ( $22 \text{ mPas}^{-1}$ ) showed an intermediate viscosity. Polymer solutions at 9 wt.% and 12 wt.% are expected to show a similar Newtonian response. However, these results are not reported because the measurements were too close to the minimum torque resolution limit of the MRCR 702 rheometer ( $0.01 \text{ } \mu\text{N.m}$ ).

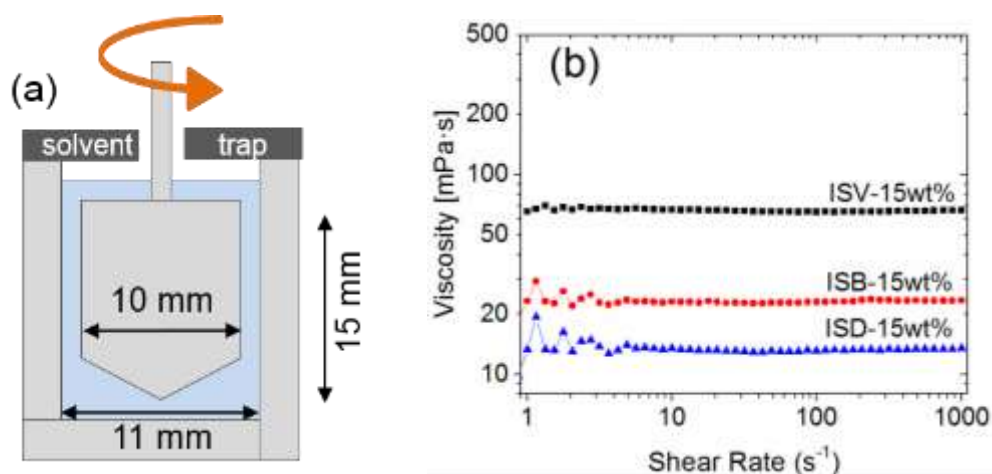


Figure 2-5. Rheometry with minimal evaporation. (a) Illustration of the 10-mm concentric cylinder fixture with a solvent trap used to discourage solvent evaporation. (b) Viscosity curves of ISV, ISB, and ISD solutions at 15 wt.% polymer concentration using the concentric cylinder fixture.

### 2.3.2 Rheometry results with significant evaporation

Figure 2-6 shows the results for the LVR determination test (alternative approach). The  $G'$  response to sinusoidal deformation as a function of time at different values of strain is reported for an ISB solution with 15 wt.% initial polymer concentration. High strain (2%) produced a lower  $G'$  compared to low strain (0.1%). Additionally, the high strain produced significant noise that suggests an extensive disruption of the integrity of the sample; that is a non-linear response to sinusoidal deformation. Figure 2-6 shows that only strain values of 0.1%, 0.5%, and 1% behaved similarly, even after significant solvent evaporation. The above statements suggest that 2% strain is already outside the LVR, and, 0.1%, 0.5% and 1% strain values are close to or within the LVR. Consequently, a 0.5% strain was selected for use in oscillatory experiments as it is within the SAOS regime.

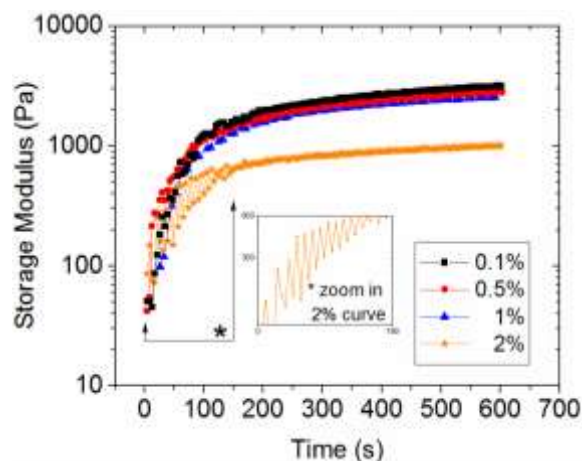


Figure 2-6. Alternative test to determine the LVR. Time sweep of a ISB solution at 15 wt.% initial polymer concentration. 0.1%, 0.5%, 1% and 2% strain points were evaluated at an oscillatory frequency of 10 rad s<sup>-1</sup>.

$G'$  and  $G''$  showed a similar trend in their evolution during the oscillatory experiments. Figure 2-3 shows how  $G'$  and  $G''$  rapidly increase over several orders of magnitude, during the initial seconds of the test. At longer times, both moduli tend to attain a steady state value.  $G'$  or  $G''$  predominance is a function of time. In the initial seconds of the experiment, the sample exhibits a viscous behavior, as expected for the predominantly solvent-containing solutions, with  $G'' > G'$ . Eventually, the predominant behavior turns to  $G' > G''$  just a few seconds after the experiment starts. This behavior suggests that the solvent evaporation produces a transition from viscous to elastic response in each tested sample. This transition is represented by the cross-over point, which is the time when  $G' = G''$ .

Figure 2-7 shows the  $G'$  and  $G''$  development upon solvent evaporation at different initial polymer concentrations for ISV (Figure 2-7a), ISB (Figure 2-7b), and ISD (Figure 2-7c) solutions. The general trend of  $G'$  and  $G''$  is similar but differs in extent due to differences in the chemistry of the triblock copolymer and the initial polymer concentration. These results are summarized in Figure 2-8. Figure 2-8 reports the initial slope, plateau slope and average  $G'$  plateau for each sample (as defined in Figure 2-3). At the same initial polymer concentration, the ISV solution exhibits the highest and fastest mechanical strength development represented by the highest average  $G'$  plateau and the highest initial slope, respectively. ISB follows at an intermediate magnitude and rate, and ISD displays the lowest magnitude and slowest rate.

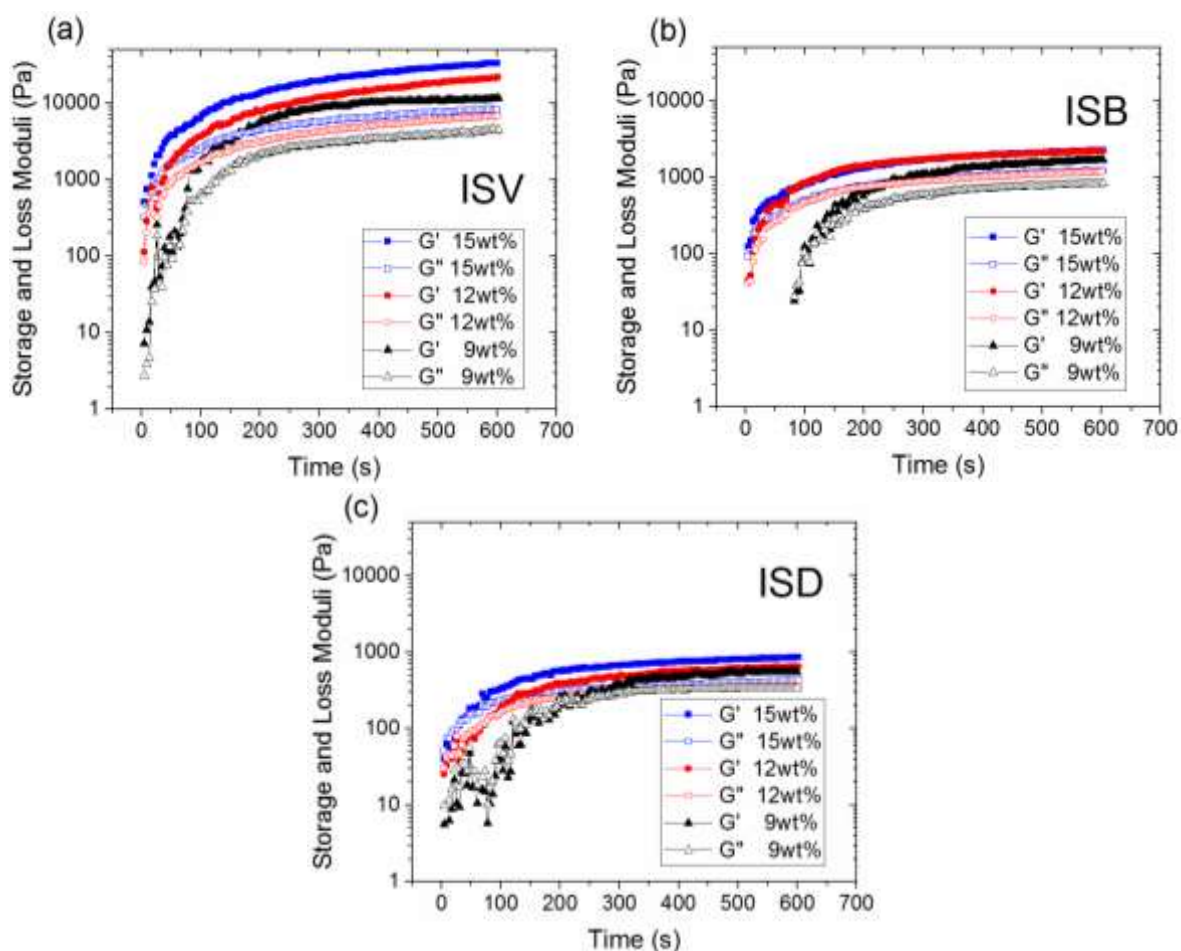


Figure 2-7. Mechanical strength development upon solvent evaporation. 9 wt.%, 12 wt.%, and 15 wt.% initial terpolymer concentrations for (a) ISV, (b) ISB, and (c) ISD solutions.

Considering the same triblock copolymer, it is observed that the initial polymer concentration is the factor that drives the rate and extent of mechanical strength development. Figure 2-8 reports that a higher initial polymer concentration results in greater initial slope and average  $G'$  plateau. On the contrary, increasing initial polymer concentration results in lower cross-over points as shown in Figure 2-9.

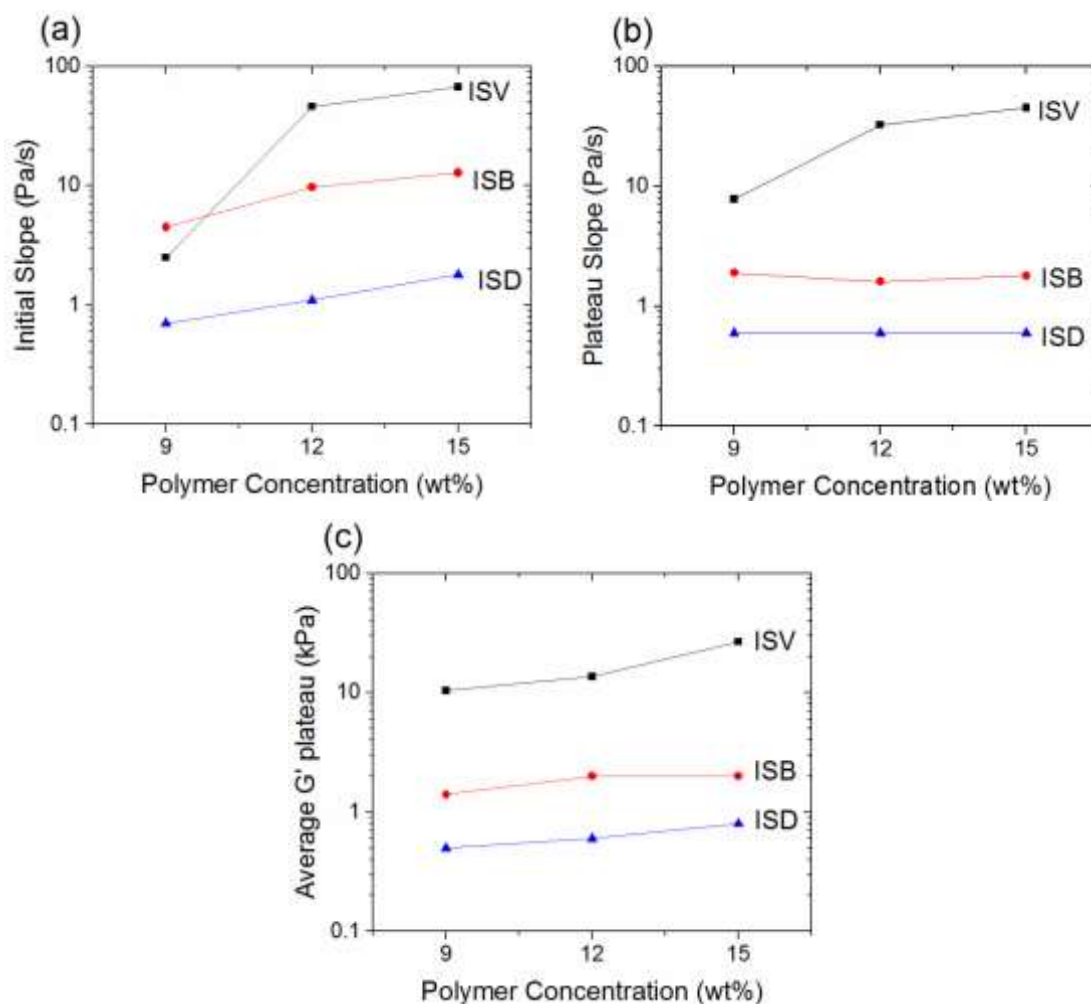


Figure 2-8. Summary of calculated four parameters. (a) Initial slope, (b) plateau slope, and (c) average  $G'$  plateau for ISV, ISB, and ISD solutions at 9 wt.%, 12 wt.% and 15 wt.% initial terpolymer concentrations; data calculated from the results in Figure 2-7.

Interestingly, the cross-over point data in Figure 2-9 seems to follow a different trend concerning block chemistry than the other three calculated parameters (reported in Figure 2-8). The ISD solution at 9 wt.% initial concentration shows the latest cross-over point compared to solutions ISV and ISB. It is expected that solutions at 12 wt.% and 15 wt.% also follow the same trend. ISV and ISB solutions at 9 wt.% initial concentrations show a cross-over point equal to 32 s and 96 s, respectively. However, cross-over points for ISV and ISB solutions at 12 wt.% and 15 wt.% are not shown because the points occur too quickly to be resolved by the rheometer accurately.

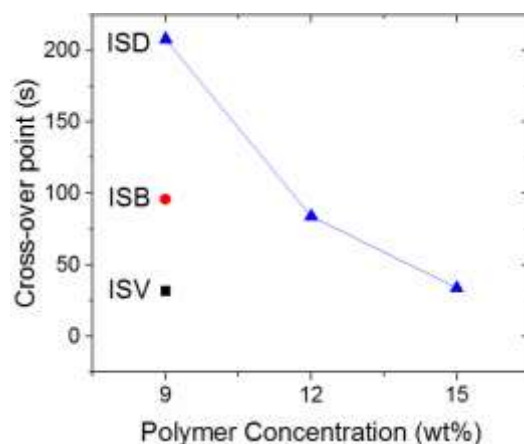


Figure 2-9. Viscous-to-elastic cross-over points for ISV, ISB, and ISD solutions initially at 9wt.%, 12wt.%, and 15wt.% terpolymer concentrations. These data points are calculated from the results in Figure 2-7.

### 2.3.3 Solvent evaporation studies

Figure 2-10 shows the apparent diffusion coefficient ( $D$ ) of the THF-DOX (30-70) solvent mixture in ISV, ISB, and ISD films.

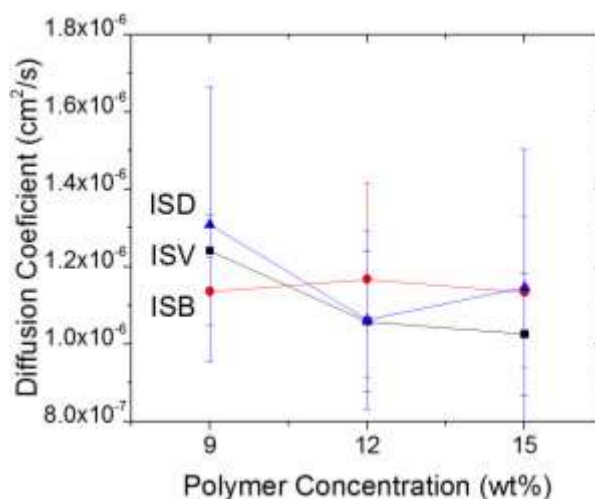


Figure 2-10. Diffusion coefficient for a solvent mixture of THF-DOX (30-70) through ISV, ISB, and ISD terpolymer films. The initial terpolymer concentrations were 9wt.%, 12wt.%, and 15wt.%.

It is observed that the coefficient was independent of solution concentration and triblock terpolymer chemistry. The diffusion coefficient varied from  $1.02 \times 10^{-6}$  to  $1.31 \times 10^{-6} \text{ cm}^2 \text{ s}^{-1}$  for

the different chemistries and initial polymer concentrations, with overlapping standard deviation in average  $D$  values. Consequently, any variation in  $D$  was not statistically significant, and the solvent diffusion coefficient was considered to be similar for all samples.

## 2.4 Discussion

### 2.4.1 The effect of block chemistry on the flow behavior (no evaporation)

Rotational rheometry has been previously used to study SNIPS polymer solutions, with a particular focus on determining the effects of polymer solution concentration through the measurement of solution viscosity.<sup>14</sup> Previous literature stated that block polymers in solution with low viscosities (low polymer concentrations) tend to precipitate asymmetric membranes with finger-like macrovoids.<sup>30, 23</sup> These finger-like domains are desirable as a support layer for SNIPS membranes because they provide lower resistance to the flow of solvent during filtration and adsorptive applications. Conversely, block polymers in solution with high viscosity (high polymer concentration) tend to precipitate a sponge-like support structure due to losses in chain mobility. This sponge-like structure is a less-desirable result for membrane performance because of its higher resistance to flow results in a lower permeability.<sup>31</sup> Consequently, the study of the effects of polymer chemistry on the viscosity of the SNIPS polymer solutions may be used to tune the final microstructure of SNIPS membranes.<sup>32</sup>

The viscosity responses ( $\eta$ ) displayed in Figure 2-5b for 15 wt.% ISV, ISB, and ISD solutions are Newtonian (i.e., independent of shear rate), with  $\eta_{\text{ISV}} > \eta_{\text{ISB}} > \eta_{\text{ISD}}$ . This response is characteristic of a dilute polymer solution, where the intermolecular forces are negligible in comparison to the hydrodynamic forces between the polymer molecules and the solvent.<sup>33 34</sup> Then, the viscosity is directly dependent on the displaced volume of each polymer molecule in solution (i.e., the overall size of the swollen or coiled polymer molecule) and the frictional forces between polymer segments and the surrounding solvent.<sup>35</sup> For the solutions investigated here, the terpolymer concentrations are well above the expected critical micelle concentration (CMC; e.g., 0.13 to 0.5 wt.% for 59 kg mol<sup>-1</sup> ISD from Ref. <sup>7</sup>) so the displaced volume of individual terpolymer micelles and the micelle-solvent interactions are most important to consider.

Previous research by Radjabian, *et al.*<sup>32</sup> quantified the flow response of a particular SNIPS diblock copolymer solution (polystyrene-*b*-poly(4-vinylpyridine) in a solvent mixture of DMF/THF) and observed that the viscosity displayed a power-law, shear thinning response with exponents of approximately  $-1/2$ . It is possible that the higher polymer concentrations studied by Radjabian, *et al.*<sup>32</sup> (25 wt.% to 28 wt.%) form structures that would dissociate as the shear rate is increased and cause the observed shear thinning response. In another previous study, Dorin, *et al.*<sup>2</sup> employed small angle x-ray scattering to characterize 59 kg mol<sup>-1</sup> ISV triblock terpolymer solutions (in a solvent mixture of 7:3 DOX/THF). For the ISV solutions, only broad correlation peaks were observed for low concentration solutions (10-14 wt.% ISV) while the data displayed peaks consistent with micelles in a body centered cubic (BCC) lattice structure at concentrations of 16 wt.% ISV, which ultimately resulted in cast membrane active layers with pores displaying a simple cubic structure. Gu, *et al.*<sup>13</sup> conducted *in situ* grazing incidence small-angle x-ray scattering experiments on blade cast films of an identical ISV system to what is investigated here (43 kg mol<sup>-1</sup>; solvent mixture of 7:3 DOX/THF). The 16 wt.% ISV solution was observed to be disordered at early times (after 4 s of evaporation) but after additional evaporation ( $t > 16$  s), evidence of micelles in a BCC lattice structure was observed ( $t = 16$  s) which eventually transitioned to simple cubic (SC) at longer times ( $t > 40$  s).

In the present study, solution concentrations of 9, 12, and 15 wt.% were investigated in an evaporation-controlled rheometer cell; thus, compared to the previous studies outlined above, the solutions investigated here were more dilute and while terpolymer micelles are expected to form, the structure is likely to be disordered, causing the Newtonian behavior that was observed over the full range of shear rates (1-1000 s<sup>-1</sup>). If robust micellar structures with long-range order were present in the solutions, a shear thinning response would be expected in Figure 2-5b, as the increased flow would disrupt the structures and result in a corresponding decrease in measured stress (and thus viscosity).

Because the molar mass of the three triblock terpolymers in solution are similar (see Table 2-1), the hierarchical behavior of Newtonian viscosities reported in Figure 2-5b is most likely due to differences in micelle size. The micelle size is driven by variation in the C-block chemistry (in terms of the Hansen solubility parameter,  $\delta$ ) as well as the differences in block fraction (vol.%)

and especially the fraction of polystyrene in the molecule. Unfortunately, the three triblock terpolymers investigated here contain different C-block chemistries as well as different fractions of polystyrene; thus, it is not possible to fully deconvolute the separate impact of block chemistry and block fraction on the viscosities reported in Figure 2-5b. However, an attempt is made in the following paragraphs to provide some insight on the polymer conformation in solution, potential micelle structure, and ultimately the flow behavior of the solutions in this dilute, amorphous regime.

Table 2-2. Hansen solubility parameters for each component of the triblock terpolymer solutions.

Chemistry	Solubility parameter $\delta$ (MPa <sup>0.5</sup> )
Polyisoprene [I]	17.4 <sup>36</sup>
Polystyrene [S]	19.1 <sup>36</sup>
Poly(4-vinylpyridine) [V]	23.0 <sup>37</sup>
Poly( <i>tert</i> -butyl methacrylate) [B]	18.0 <sup>36</sup>
Poly( <i>N,N</i> -dimethylacrylamide) [D]	19.9 <sup>38</sup>
Tetrahydrofuran [THF]	19.4 <sup>36</sup>
1,4-dioxane [DOX]	20.5 <sup>39</sup>

Table 2-2 reports the Hansen solubility parameter for each component of the terpolymer solutions. Because the A- and B-block of the ISV, ISB, and ISD molecules are the same, these blocks will most likely interact similarly with the surrounding solvent molecules and allow us to concentrate our analysis on the interaction of the C-block of each terpolymer molecule with the solvents (30% THF – 70% DOX). The C-blocks of ISB and ISD are likely to adopt an expanded or swollen conformation in solution because their solubility parameters are similar to those of the solvents. Conversely, the C-block of ISV may form a more coiled or collapsed conformation in the presence of the solvents due to more significant differences in solubility parameters. 40 A more coiled molecule (or smaller micelle) would have reduced hydrodynamic drag compared with a swollen molecule, leading to a reduction in solution viscosity; thus, if solvent/C-block interactions are dominant, ISV would be expected to display the lowest viscosity. However, this trend is the opposite of what is observed in Figure 2-5b, where ISV has the highest viscosity, implying that the viscosity response is impacted by more than just block-solvent interactions.

Besides the interaction between solvents and each C-block, there is also a possibility of interactions between the A-, B-, and C-blocks. In the case of ISB and ISD, the solubility parameters are reasonably similar for all the blocks, ranging from 17.4 to 19.9 (see Table 2-2). However, for ISV the solubility parameter of the C-block is much larger (V: 23.0) than the A-block (S: 17.4) and B-block (I: 19.1); thus, this molecule is more likely to form an expanded conformation (and proportionately larger micelle) compared to ISB and ISD, which would increase the viscosity of the solution.<sup>33 34 35</sup> Thus, if intramolecular interactions are dominant, ISV would be expected to display the highest viscosity, consistent with results displayed in Figure 2-5b.

Unfortunately, considering the block-solvent and block-block interactions does not conclusively explain the viscosity values displayed in Figure 2-5b; perhaps it is also important to consider the volume fraction of polystyrene (B-block) in the molecules. A higher concentration of polystyrene in the ISV (55 vol.%) compared to the ISB (41 vol.%) and ISD (43 vol.%) molecules is consistent with the increased viscosity of ISV solutions. Rangou, *et al.*<sup>14</sup> found a positive relationship between the viscosity of SNIPS polymer solutions and the concentration of polystyrene in the polymer molecule as reduced viscosities were measured for polystyrene-*b*-poly(4-vinylpyridine) diblock copolymer solutions with an increasing 4-vinylpyridine fraction (and proportionally less polystyrene). The authors do not attempt to explain this behavior; however, it is likely that the relatively large (“bulky”) phenyl group of the styrene segments results in steric hindrance that manifests as an overall increase in molecule volume and thus greater hydrodynamic drag in solution.<sup>41</sup> Consequently, in the present investigation, the higher concentration of polystyrene in ISV may increase the molecule (micelle) volume compared with ISD and ISB and result in increased viscosity of the solution, again consistent with the results displayed in Figure 2-5b.

In summary, the hierarchical viscosity behavior of 15 wt.% ISV, ISB, and ISD triblock terpolymer solutions may be the result of the relative magnitudes of hydrodynamic drag forces caused by the different conformations adopted by the triblock terpolymers in solution which are believed to result in the formation of larger, disordered micelles within ISV solutions compared with ISD and ISB solutions. The observations in Figure 2-5b are most likely controlled by a combination of the factors described above; e.g., viscosity increases could be the combined result of the dominance

of block-block interactions over block-solvent interactions and the steric hindrance contributions of polystyrene.

#### 2.4.2 Viscoelastic behavior with significant evaporation

The results of the rotational experiments were meaningful because the internal structure of the sample only suffered deformation induced by shear (e.g., rotational shear at a constant polymer concentration). In the case of samples with variable polymer concentration, the results generated from oscillatory experiments are more meaningful because it is possible to isolate the effect of solvent evaporation over the viscoelastic development.<sup>25</sup>

In a block polymer solution with minimal solvent evaporation (see Figure 2-5a), the enthalpic intermolecular interactions of the block polymer are partially screened by the solvent molecules,<sup>35</sup> and the viscosity of the solution does not depend on the mobility of the individual polymer segments.<sup>42</sup> However, in the absence of solvent, polymer-to-polymer intermolecular interactions increase due to the enthalpic interaction of each segment of the block polymer,<sup>20</sup> and significant solvent evaporation drives the system to form nanodomains in solution.<sup>32</sup> Pendergast, *et al.*<sup>43</sup> have previously speculated that for a triblock terpolymer solution undergoing SNIPS, the resulting selective layer upon solvent evaporation is composed of a polystyrene matrix with spherical inclusions of polyisoprene and a cubic network of channels of the respective third block. The evaporation of the solvent is the initial step towards the creation of a viscoelastic film containing these phase-segregated pores.

The development of the mechanical strength with time (reported in Figure 2-7) of triblock copolymer solutions studied here is attributed to the formation of a viscoelastic film at the edge of the parallel plates (illustrated in Figure 2-11). The viscoelastic film can be thought of as a “skin” and is typically found in asymmetric membranes obtained from precipitation of polymer solutions.<sup>30</sup> Figure 2-11 shows the hypothesized location of a viscoelastic film that is formed as a result of the progressive removal of the solvent. Film formation initiates at the air-liquid interface and grows radially toward the center of the parallel plates, acting as a physical barrier that delays the migration of solvent from the bulk to the air-liquid interface.<sup>30</sup> The  $G'$  and  $G''$  response, the cross-over point, and the  $G'$  plateau behavior is mainly attributed to the mechanical strength

development of this viscoelastic film which, in turn, depends on the chemistry of the polymer molecules and the initial polymer concentration in the solutions.

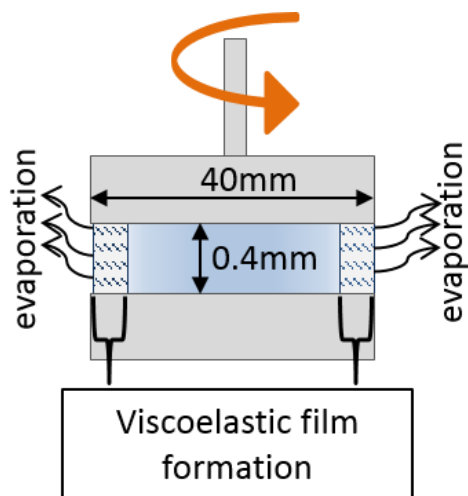


Figure 2-11. Hypothesized location of an evaporation-induced viscoelastic film Formed during oscillatory testing in a 40 mm parallel plate fixture.

The differences in mechanical strength development reported in Figure 2-7 at the same polymer concentration may be attributed to the possible long-range lattice organization based on the differences in block chemistry of each sample. Sargent, *et al.*<sup>7</sup> previously reported that ISD terpolymer solutions ( $59 \text{ kg mol}^{-1}$ ) formed individual micelles at low polymer concentrations (<1 wt.%) and long-range lattices at significantly higher polymer concentration (>22 wt.%) using DOX as a solvent. Dorin, *et al.*<sup>2</sup> showed that 16 wt.% ISV terpolymer solutions ( $59 \text{ kg mol}^{-1}$ ) organized into lattices using a 7:3 THF:DOX solvent mixture. Meanwhile Gu, *et al.*<sup>13</sup> showed that the type and extent of micellar organization within ISV terpolymer solutions ( $43 \text{ kg mol}^{-1}$ ) was a function of solvent concentration.

All three studies mentioned above convey the idea that the long-range micelle organization is directly connected to the final pore structure of the selective layer of SNIPS membranes. Then, the type and extent of the mechanical response to deformation depend on the type of lattice structure and the evolution of the lattice structure over time. Unfortunately, due to the difference between each study and the samples used in the present experiments, there is insufficient evidence to accurately correlate the effect of micellar organization on the mechanical strength development reported in Figure 2-7 and the trend differences of data reported in Figure 2-8a. However, in all

cases, micelle assembly and long-range ordering, as well as the bulk mechanical response to deformation, also depend on the mobility of the individual polymer molecules. Consequently, here an attempt is made to understand better the mechanical responses reported in Figure 2-7 from the perspective of individual molecules. Upon solvent evaporation, the intermolecular distance between polymer chains (and micelles) is significantly reduced and the surface area of polymer chains in contact with each other increases, which in turn, increases the energy required for polymer chains to translate past each other.<sup>44</sup> The increase in energy required for motion, including local conformation changes, is intensified if the polymer molecule has relatively bulky side groups attached to the backbone.<sup>44 45</sup> Consequently, a more significant amount of energy, proportional to the concentration and type of side group, must be applied to induce molecular motion and, specifically, the deformation and restructuring of micelles.<sup>41 46</sup>

In this work, all three terpolymer molecules contain bulky side groups within the B- and C-block. The B-block is a relatively stiff macromolecule (polystyrene) with large phenyl rings as side groups. The C-block contains 4-vinylpyridine in ISV, *tert*-butyl methacrylate in ISB, and *N,N*-dimethylacrylamide in ISD (see Figure 2-2). As shown in Figure 2-7, the growth rate of  $G'$  and  $G''$  is dependent on polymer chemistry and polymer initial concentration. These trends may be partly explained by considering the rotational barrier energies of chemical structures that are analogous to the bulky side groups of the ISV, ISB, and ISD. Bryantsev, *et al.*<sup>47</sup> reported rotational barrier energy values for alkyl- and phenyl-substituted urea around a C-N bond: 0.86-2 kcal/mol for methylurea, 5.2-9 kcal/mol for *tert*-butylurea, and 9-15 kcal/mol phenylurea. Due to the similarities in chemical structure, the methylurea groups that Bryantsev, *et al.* studied are a close representation of the *N,N*-dimethylacrylamide groups in the ISD molecule. In the same way, *tert*-butylurea is representative of *tert*-butyl methacrylate in ISB, and, phenylurea is analogous to phenyl rings (B-block) and 4-vinylpyridine in ISV. Then, considering the rotational barrier values reported by Bryantsev *et al.* for each bulky side group in the C-block, it is expected that 4-vinylpyridine will restrict the ability of ISV molecules (and micelles) to translate past each other to a greater extent than the *tert*-butyl methacrylate and *N,N*-dimethylacrylamide groups in ISB and ISD, respectively.<sup>41 45</sup> In addition, the higher concentration of polystyrene that ISV contains over ISB and ISD (see vol.% in Table 2-1) represents a higher density of bulky side groups per molecule with the highest rotational barrier. Subsequently, ISV molecules (and micelles) are expected to

require greater input energy compared to ISB and ISD molecules to deform a given amount,<sup>41</sup> consistent with the results in Figure 2-7 and the trends displayed by ISV solutions in Figure 2-8a (greatest initial slopes) and Figure 2-8c (greatest average  $G'$  plateau.)

Initial polymer concentration has a strong influence on the temporal cross-over points reported in Figure 2-9. In general, the viscous-to-elastic transition occurs at reduced times for solutions with greater initial polymer concentrations (and thus greater solution viscosity). If the solvent diffusion coefficient is considered the same for all samples (as was found here), then the viscous-to-elastic transition is also dependent on the type and density of bulky side groups present in the molecule. ISD solutions displayed the greatest transition times for all initial polymer concentrations (9 wt.%: 208 s; 12 wt.%: 84 s; 15 wt.%: 34 s). The viscous-to-elastic transition for 9 wt.% ISV and ISB solutions occurred more quickly (32 s, 96 s, respectively); and the cross-over points for 12 wt.% and 15 wt.% ISV and ISB solutions are not shown in Figure 2-9 because the viscous-to-elastic transition apparently happens very fast ( $t < 4$  s, beyond the measurement window of the experiment). These results are consistent with the analysis of rotational barriers for ISV, ISB and ISD molecules.

In summary, the observed order of the oscillatory rheometry results agrees well with the rotational rheometry results. ISV solutions displayed the greatest initial viscosity as well as the fastest development and greatest magnitude of mechanical strength. The viscosity behavior of each solution is attributed to the dominant block-block interactions and the steric hindrance of polystyrene which most likely manifests in the formation of larger micelles in the ISV solutions compared with ISB and ISD solutions. Upon solvent evaporation, mechanical strength develops as the terpolymer micelles order into lattices, the initial rate of which may be controlled by the presence of bulky side groups in the C-blocks of each molecule and their different rotational barriers. As solvent evaporation proceeds further, additional restructuring is possible. For example, in addition to segregation of poly(4-vinylpyridine) from polystyrene and polyisoprene in ISV, the polyisoprene blocks segregate from the polystyrene blocks which is most likely responsible for the observed transition from BCC to SC observed by Gu, et al.<sup>13</sup> for 16 wt.% ISV solutions. There then will exist domains of poly(4-vinylpyridine) and polyisoprene in a matrix of polystyrene, and the observed resistance to shear is likely dependent on the energy required to deform the ordered

lattice and its rate of evolution (e.g., from BCC to SC) than on the rotational barrier energies of the molecular structures of individual molecules.

### **2.4.3 The block chemistry effect over the solvent evaporation rate**

The similar diffusion coefficient ( $D$ ) of a THF-DOX solvent mixture in ISV, ISB, and ISD films is attributed to the similar chemical structure of the triblock terpolymer molecules and, specifically, the isoprene-styrene matrix that forms upon solvent evaporation. On average, 75% of the triblock terpolymer molecules are composed of polyisoprene and polystyrene blocks in relatively similar proportions. Having a very similar matrix to diffuse through, it is not surprising that the rate of solvent diffusion is very similar for the different films.<sup>48</sup>

## **2.5 Summary and Implications**

The role of the triblock terpolymer chemistry and solvent evaporation over the mechanical strength development of polymer solutions used to fabricate membranes via SNIPS process was studied. Three different polymer chemistries with similar molar mass were analyzed. Shear rheometry was used to quantify the flow behavior under minimal and significant solvent evaporation conditions. The solvent diffusion coefficients through different polymer films were also measured and found to be independent of initial solution concentration (9 wt.%, 12 wt.%, and 15 wt.% polymer in solution) and triblock terpolymer composition (ISV, ISB, and ISD). Results suggested that: For all triblock terpolymer solutions investigated here, solvent evaporation resulted in the formation of a viscoelastic film typical of asymmetric membranes. The development rate and magnitude of the film's mechanical strength were successfully measured with oscillatory rheometry and parallel-plate fixtures.

For all triblock terpolymer compositions, the increased initial concentration of polymer in solution resulted in greater solution viscosities (found to be Newtonian), faster strength development, and greater strength magnitudes.

Solution properties – viscosity and mechanical strength development – were strongly dependent on the chemical structure of the triblock terpolymer molecules. A hierarchical order (ISV>ISB>ISD) in magnitude was observed for both properties, with ISV solutions displaying the

greatest solution viscosity and fastest strength development and greatest strength magnitude of the evaporation-induced viscoelastic film.

Block-block and block-solvent interactions, as well as the concentration of polystyrene within the terpolymer molecules, are believed to be the factors that most influenced the experimental results by directly impacting the relative size of terpolymer micelles that are expected to form in solution and the ability of the micelles to order and restructure as the solvent evaporates.

The findings above may have potential use to tailor the final microstructure of SNIPS filtration membranes. The viscosity of polymer solutions can be tailored based on the physical and chemical information of the selected polymer molecule. In this specific case, it can be speculated that ISV polymer solutions will require a smaller concentration of polymer than ISB and ISD solutions to achieve the desired viscosity, micelle mobility, and a final macro-void support layer.

## 2.6 References

1. Peinemann K-V, Abetz V, Simon PFW. Asymmetric superstructure formed in a block copolymer via phase separation. 2007. doi:10.1038/nmat2038
2. Dorin RM, Marques DS, Sai H, et al. Solution Small-Angle X-ray Scattering as a Screening and Predictive Tool in the Fabrication of Asymmetric Block Copolymer Membranes. *ACS Macro Lett.* 2012;1(5):614-617. doi:10.1021/mz300100b
3. Mulvenna R a., Weidman JL, Jing B, et al. Tunable nanoporous membranes with chemically-tailored pore walls from triblock polymer templates. *J Memb Sci.* 2014;470:246-256. doi:10.1016/j.memsci.2014.07.021
4. Y. Zhang, J. L. Sargent, B. W. Boudouris WAP. Microfiltration and ultrafiltration membrane science and technology. *J Appl Polym Sci.* 2015;41683:17. doi:10.1002/app.42002
5. Gu Y, Werner JG, Dorin RM, Robbins SW, Wiesner U. Graded porous inorganic materials derived from self-assembled block copolymer templates. *Nanoscale.* 2015;7(13):5826-5834. doi:10.1039/C4NR07492K
6. Dorin RM, Phillip W a., Sai H, Werner J, Elimelech M, Wiesner U. Designing block copolymer architectures for targeted membrane performance. *Polym (United Kingdom).* 2014;55(1):347-353. doi:10.1016/j.polymer.2013.09.038

7. Sargent JL, Hoss DJ, Phillip WA, Boudouris BW. Solution self-assembly behavior of A-B-C triblock polymers and the implications for nanoporous membrane fabrication. *J Appl Polym Sci*. 2017;45531:1-8. doi:10.1002/app.45531
8. Poole JL, Donahue S, Wilson D, et al. Biocatalytic Stimuli-Responsive Asymmetric Triblock Terpolymer Membranes for Localized Permeability Gating. *Macromol Rapid Commun*. 2017;1700364:1700364. doi:10.1002/marc.201700364
9. Yang SY, Park J, Yoon J, Ree M, Jang SK, Kim JK. Virus filtration membranes prepared from nanoporous block copolymers with good dimensional stability under high pressures and excellent solvent resistance. *Adv Funct Mater*. 2008;18(9):1371-1377. doi:10.1002/adfm.200700832
10. Weidman JL, Mulvenna RA, Boudouris BW, Phillip WA. Unusually Stable Hysteresis in the pH-Response of Poly(Acrylic Acid) Brushes Confined within Nanoporous Block Polymer Thin Films. *J Am Chem Soc*. 2016;138(22):7030-7039. doi:10.1021/jacs.6b01618
11. Weidman JL, Mulvenna RA, Boudouris BW, Phillip WA. Nanostructured Membranes from Triblock Polymer Precursors as High Capacity Copper Adsorbents. *Langmuir*. 2015;31(40):11113-11123. doi:10.1021/acs.langmuir.5b01605
12. Dorin RM, Sai H, Wiesner U. Hierarchically Porous Materials from Block Copolymers. *Chem Mater*. 2014;26(1):339-347. doi:10.1021/cm4024056
13. Gu Y, Dorin RM, Tan KW, Smilgies DM, Wiesner U. In Situ Study of Evaporation-Induced Surface Structure Evolution in Asymmetric Triblock Terpolymer Membranes. *Macromolecules*. 2016;49(11):4195-4201. doi:10.1021/acs.macromol.6b00265
14. Rangou S, Buhr K, Filiz V, et al. Self-organized isoporous membranes with tailored pore sizes. *J Memb Sci*. 2014;451:266-275. doi:10.1016/j.memsci.2013.10.015
15. Li YM, Zhang Q, Álvarez-Palacio JR, et al. Effect of humidity on surface structure and permeation of triblock terpolymer derived SNIPS membranes. *Polym (United Kingdom)*. 2017;126:368-375. doi:10.1016/j.polymer.2017.05.037
16. Phillip W a., Hillmyer M a., Cussler EL. Cylinder Orientation Mechanism in Block Copolymer Thin Films Upon Solvent Evaporation. *Macromolecules*. 2010;43(18):7763-7770. doi:10.1021/ma1012946

17. Schaefer C, Van Der Schoot P, Michels JJ. Structuring of polymer solutions upon solvent evaporation. *Phys Rev E - Stat Nonlinear, Soft Matter Phys.* 2015;91(2):1-6. doi:10.1103/PhysRevE.91.022602
18. Phillip W a, Dorin RM, Werner J, Hoek EM V, Wiesner U, Elimelech M. Tuning structure and properties of graded triblock terpolymer-based mesoporous and hybrid films. *Nano Lett.* 2011;11(7):2892-2900. doi:10.1021/nl2013554
19. U.S. Department of Energy. Roll to Roll Processing. In: 2015 QTR, ed. *Innovating Clean Energy Technologies in Advance Manufacturing.* ; 2015:34. [http://energy.gov/sites/prod/files/2015/02/f19/QTR Ch8 - Roll To Roll Processing TA Feb-13-2015.pdf](http://energy.gov/sites/prod/files/2015/02/f19/QTR_Ch8_-_Roll_To_Roll_Processing_TA_Feb-13-2015.pdf).
20. Arya RK. Drying Induced Phase Separation. *J Chem Eng.* 2012;C(1):12-20.
21. Macosko CW. *Rheology: Principles, Measurements, and Applications.* Vol 41. Wiley-Blackwell; 1995. doi:10.1002/aic.690411025
22. Chassenieux C, Nicolai T, Benyahia L. Rheology of associative polymer solutions. *Curr Opin Colloid Interface Sci.* 2011;16(1):18-26. doi:10.1016/J.COCIS.2010.07.007
23. Winnik MA, Yekta A. Associative polymers in aqueous solution. *Curr Opin Colloid Interface Sci.* 1997;2(4):424-436. doi:10.1016/S1359-0294(97)80088-X
24. Hamley IW. *Block Copolymers in Solution : Fundamentals and Applications.* Wiley; 2005. <https://www.wiley.com/en-us/Block+Copolymers+in+Solution%3A+Fundamentals+and+Applications-p-9780470015575>. Accessed June 26, 2018.
25. Zhou J, Man X, Jiang Y, Doi M. Structure Formation in Soft-Matter Solutions Induced by Solvent Evaporation. *Adv Mater.* 2017;29(45):1703769. doi:10.1002/adma.201703769
26. Caicedo-Casso E, Sargent J, Dorin RM, et al. A rheometry method to assess the evaporation-induced mechanical strength development of polymer solutions used for membrane applications. *J Appl Polym Sci.* August 2018:47038. doi:10.1002/app.47038
27. Crank J. *The Mathematics of Diffusion.* 2nd ed. Oxford University Press; 1975.
28. Bird RB, Stewart WE, Lightfoot EN. *Transport Phenomena.* J. Wiley; 2007.
29. Atkinson PM, Lloyd DR. Anisotropic flat sheet membrane formation via TIPS: thermal effects. *J Memb Sci.* 2000;171(1):1-18. doi:10.1016/S0376-7388(99)00376-2

30. Strathmann H, Kock K. The formation mechanism of phase inversion membranes. *Desalination*. 1977;21(3):241-255. doi:10.1016/S0011-9164(00)88244-2
31. Zhang Q, Li YM, Gu Y, Dorin RM, Wiesner U. Tuning substructure and properties of supported asymmetric triblock terpolymer membranes. *Polym (United Kingdom)*. 2016;107:398-405. doi:10.1016/j.polymer.2016.07.076
32. Radjabian M, Koll J, Buhr K, et al. Tailoring the morphology of self-assembled block copolymer hollow fiber membranes. *Polymer (Guildf)*. 2014;55(13):2986-2997. doi:10.1016/j.polymer.2014.04.041
33. Brust M, Schaefer C, Doerr R, et al. Rheology of human blood plasma: Viscoelastic versus Newtonian behavior. *Phys Rev Lett*. 2013;110(7):6-10. doi:10.1103/PhysRevLett.110.078305
34. Cassagnau P. Linear viscoelasticity and dynamics of suspensions and molten polymers filled with nanoparticles of different aspect ratios. *Polym (United Kingdom)*. 2013;54(18):4762-4775. doi:10.1016/j.polymer.2013.06.012
35. Larson RG. *The Structure and Rheology of Complex Fluids (Topics in Chemical Engineering)*. Oxford University Press; 1999.
36. H. G. Barth REM. Approaches for Extracting and determining additives, contaminants, and low-molecularweight by-products in synthetic polymers. *LCGC North Am*. 2013;31(1):14-29.
37. O'Driscoll S, Demirel G, Farrell RA, et al. The morphology and structure of PS-b-P4VP block copolymer films by solvent annealing: Effect of the solvent parameter. *Polym Adv Technol*. 2011;22(6):915-923. doi:10.1002/pat.1596
38. Krevelen DW van (Dirk W, Nijenhuis K te. *Properties of Polymers : Their Correlation with Chemical Structure ; Their Numerical Estimation and Prediction from Additive Group Contributions*. Elsevier; 2009.
39. Hansen CM. *Hansen Solubility Parameters : A User's Handbook*. CRC Press; 2007.
40. Pendergast MM, Mika Dorin R, Phillip WA, Wiesner U, Hoek EM V. Understanding the structure and performance of self-assembled triblock terpolymer membranes. *J Memb Sci*. 2013;444:461-468. doi:10.1016/j.memsci.2013.04.074
41. Bueche F. Segmental Mobility of Polymers Near Their Glass Temperature. *J Chem Phys*. 1953;21(10):1850. doi:10.1063/1.1698677

42. Adam M, Delsanti M. Viscosity of semi-dilute polymer solutions. *J Phys*. 1982;43(3):549-557. doi:10.1051/jphys:01982004303054900>
43. Pendergast MM, Mika Dorin R, Phillip W a., Wiesner U, Hoek EMV. Understanding the structure and performance of self-assembled triblock terpolymer membranes. *J Memb Sci*. 2013;444:461-468. doi:10.1016/j.memsci.2013.04.074
44. Brueggeman BG, Minnick MG, Schrag JL. The Influence of Side Groups in Polymer Chain Dynamics. Alternative Comparisons of Viscoelastic Data and Dilute Solution Theory. *Macromolecules*. 1978;11(1):119-126. doi:10.1021/ma60061a022
45. Shaw MT, MacKnight WJ. *Introduction to Polymer Viscoelasticity*. 3rd ed. John Wiley & Sons, Inc.; 2005. doi:10.1002/0471741833.fmatter
46. Lenhart JL, Fischer DA, Chantawansri TL, Andzelm JW. Surface orientation of polystyrene based polymers: Steric effects from pendant groups on the phenyl ring. *Langmuir*. 2012;28(44):15713-15724. doi:10.1021/la303507e
47. Bryantsev VS, Firman TK, Hay BP. Conformational Analysis and Rotational Barriers of Alkyl-and Phenyl-Substituted Urea Derivatives. *J Phys Chem*. 2005;109(5):832-842. doi:10.1021/jp0457287
48. Tsige M, Grest GS. Solvent evaporation and interdiffusion in polymer films. *J Phys Condens Matter*. 2005;17(49):S4119-S4132. doi:10.1088/0953-8984/17/49/008

### 3. RHEO-PHYSICAL CHARACTERIZATION OF MICROSTRUCTURES SENSITIVE TO SHEAR DEFORMATION: THE CASE OF CONCENTRATED SURFACTANT SOLUTIONS

Portions of the following chapter contain text or figure adapted with permission from Caicedo-Casso, E., Bice, J.E., Nielsen, L.R., Sargent, J., Lindberg, S., and Erk, K.A. (2019) Rheo-physical characterization of microstructure and flow behavior of concentrated surfactant solutions. *Rheologica Acta*. Accepted (in-press.)

#### 3.1 Introduction

In an effort to comply with international environmental standards, the industry of consumer cleaning and beauty care is making commitments to reduce the water usage in their products.<sup>1 2 3</sup> Concentrated consumer products are new platforms with efficient packaging and transportation considering that they deliver principally active ingredients. Consequently, the production of concentrated materials is an appropriate way of reducing the usage of fossil fuels and contribute to a reduced environmental footprint from the consumer cleaning and beauty care industry.<sup>4</sup> Nonetheless, fabricating concentrated materials is difficult when using conventional production methods. Processing of concentrated feedstock regularly induces an increasing in the input energy (cost). Additionally, concentrated formulations are very sensitive to shear processing; mixing and other operations based on shear flow may alter the initial material's microstructure and thus its basic properties.<sup>5</sup>

For instance, consider the different microstructures, physical properties and flow behaviors that a widely used anionic surfactant such as sodium laureth sulfate could exhibit. Figure 3-1, shows the relative changes in the microstructure of sodium laureth sulfate solutions as a function of surfactant concentration. The molecules self-assemble into spherical micelles in the dilute state (often < 26 wt.%, depending on hydrophobic chain length) and form a solution that is optically isotropic and Newtonian. However, in the concentrated state (typically > 26 wt.%), the molecules form optically birefringent, lyotropic crystalline structures with increased viscoelasticity and non-Newtonian character.<sup>6 7 8</sup> Additionally, the incorporation of additives like oil or salt are known to alter the microstructure and bulk rheology of all phases (*e.g.*, induce cylindrical, “worm-like” micelles from spherical ones).<sup>8</sup>

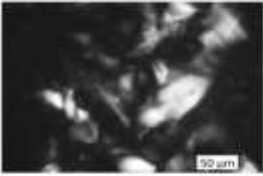
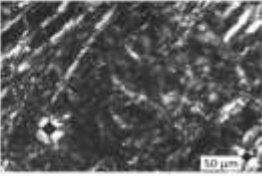
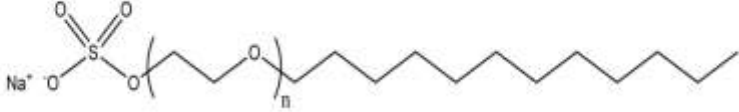
Concentration	0-26%	26-60%	60-70%
Surfactant Phase	Spherical Micelles	Hexagonal	Lamellar
Polarized Light Micrograph			
SLE <sub>1</sub> S molecule			

Figure 3-1 Microstructural organization of sodium laureth sulfate (SLE<sub>1</sub>S) in deionized water. Isotropic (22°C) phase diagram

The rheological behavior of dilute detergents (typically Newtonian) has been studied for decades thanks to a straightforward sample preparation and measurement of rheological properties. The extent knowledge of microstructure-flow relationships of dilute surfactant solutions (spherical and worm-like micelles) fuels the quick development on design and manufacture.<sup>9</sup> Conversely, the development of concentrated detergents is slow and complex because the characterization of concentrated surfactant solutions such as lyotropic structures (non-Newtonian and prone to structural changes under flow) has been more challenging due to the convoluted interplay between microstructure and shearing.<sup>6 10 11 12 13 14</sup>

Commonly, the rheological characterization of consumer products (dilute or concentrated) is executed using bulk shear rheometry. Engineers use shear rheometry measurements to solve day-to-day issues with fabrication or formulation of products because rheometers are fast, versatile, and cost-effective to elucidate and measure the bulk viscosity and viscoelastic behavior of complex fluids.<sup>15</sup> For instance, process designers rely on rheological information knowledge to specify and design transport of liquids, often over distances of hundreds of meters and high flow rates.<sup>16</sup> Likewise, same rheological measurements can help product designers to ensure that final formulations have enough fluidity while dosing yet remain thick enough to perform adequately; *e.g.*, the fluid should remain in the consumer's hand after dosing without running through their fingers.

Certainly, bulk rheometry has a general utility in the development of consumer products. However, the routine data analysis associated with these measurements is typically “blind” to the formation and evolution of shear-induced flow instabilities within the sample.<sup>17</sup> Shear rheometers calculate important rheological parameters based on assumptions such as the “no-slip” boundary condition, homogeneous laminar flow (simple shear) throughout the sample, and quiescent relaxation upon shear cessation.<sup>18</sup> However, these assumptions are often violated during the study of microstructured fluids (*e.g.*, concentrated surfactants), as typical rheological responses of these materials often include a number of flow instabilities and artifacts, including signatures of wall-slip, shear banding, and fluid fracture.<sup>19</sup>

Wall-slip is considered to be a sudden disengagement of the bulk sample from the wall of the rheometer fixture, and such the sample adhered to the wall have different shear response than the bulk sample response.<sup>20 21 22</sup> Shear banding is the formation of mesoscopic domains within the sample that display distinct deformation responses, typically manifest as domains with different local velocities of deformation.<sup>23 24 25</sup> Fluid fracture is an extreme example of strain localization within a sample, resulting in the creation of stationary domains (*i.e.*, zero or near-zero shear rate) adjacent to moving domains.<sup>26 27 28</sup> The root cause of each instability in microstructured fluids varies widely, from edge effects<sup>29 30 31</sup> and sample inhomogeneities (*e.g.*, trapped air bubbles and contaminants, segregation and sedimentation)<sup>32 33</sup> to deformation-induced restructuring of the fluid driven by physical relaxation events,<sup>34</sup> concentration gradients,<sup>35</sup> and phase changes.<sup>36</sup>

Clearly, significant complications to interpret rheological data are introduced by the presence of known or unknown flow instabilities. The unsteady behavior of microstructured fluids, often transient in nature, coupled with the lack of physical, morphological feedback from standard rotational rheometers make these instruments prone to report artifacts and misleading data. For instance, data which may resemble a uniform shear thinning could actually result from the formation of localized shear bands and fracture zones within the specimen (*e.g.*, as observed with physically associating polymer solutions<sup>25 37 38 39</sup>). This is especially typical when the measuring shear rates may exceed relaxation timescales of the fluid (*i.e.*, at moderate to high values of the Weissenberg number).

Therefore, it is essential to combine rheological characterization with suitable physical measurements to fully understand the rheological response of microstructured fluids for industrial applications (e.g., concentrated surfactant solutions which are foundational to most consumer care products). Such suitable physical measurements are gathered using rheo-physical characterization techniques. These hyphenated techniques combine rheological measurements with microstructural,<sup>40</sup> chemical,<sup>41</sup> or physical evolution<sup>42</sup> of soft materials and microstructured (complex) fluids. The most adequate rheo-physical measurement to help fulfill the goal of this study is referred to as rheo-flow velocimetry.<sup>43</sup> This is a family of techniques in which local velocities within a sample can be directly quantified along with the simultaneous collection of rheological data.<sup>44 45 46</sup> Rheo-flow velocimetry techniques applied to rotational rheometry include, but are not limited to, magnetic resonance velocimetry (MRV),<sup>47 48</sup> particle image velocimetry (PIV),<sup>49</sup> particle tracking velocimetry (PTV),<sup>50</sup> laser Doppler velocimetry (LDV),<sup>51</sup> and ultrasonic speckle velocimetry (USV).<sup>52</sup> The choice of technique for a given application is typically dictated by the material of interest; for instance, PIV, PTV, and USV systems may have similar spatial and temporal resolutions but USV systems will perform best for opaque samples while laser-based PIV and PTV systems are better suited for transparent or semi-transparent samples.

This chapter introduces the second protocol developed in this dissertation. This chapter attempts to draw meaningful connections between the formulation, microstructure, and rheological properties of solutions of sodium laureth sulfate (SLE<sub>1</sub>S). A key objective of this study is to evaluate the quality of information about concentrated surfactants that can be obtained from a single flow curve, a basic rheological measurement of shear stress as a function of applied strain rate that is potentially ideal for screening a large number of different formulations in an industrial setting. SLE<sub>1</sub>S was selected for use here to easily recreate the different microstructural arrangements that are most commonly found in the vast majority of consumer care products, from cleaning products to beauty care. The “model microstructures” – specifically, spherical micelles, worm-like micelles, hexagonally packed micelles, and lamellar structures – were created by simply varying the concentration of surfactant in water from 20 to 70 wt.% and by increasing the ionic concentration with the addition of salt (2-5% NaCl). X-ray scattering measurements were performed to characterize the microstructure of each solution, and for select samples, the evolution of the microstructure during shear deformation was directly observed through optical birefringence

measurements in conjunction with a parallel-plate shear cell. Then a combination of basic shear rheometry and advanced rheo-physical measurements – rheometry coupled with ultrasound-based flow visualization – was performed to correlate rheometry data with the local deformation response of shear-induced evolving microstructures.

## **3.2 Materials and Methods**

### **3.2.1 Surfactant paste formulation**

Sodium laureth sulfate (SLE<sub>1</sub>S, where 1 denotes the presence of a single ethoxy group) surfactant paste was obtained from Stepan Company and used as received: STEOL CS170 UB SLE<sub>1</sub>S, 70 wt.% surfactant in water, with a hydrophobic average chain length of 12 carbon (C) atoms and range of C10-C16.

The naming convention adopted for this study reports both the expected static microstructure of the sample and surfactant concentration. Raw SLE<sub>1</sub>S paste will be denoted as “lamellar-70”. Diluted surfactant paste (using reverse osmosis water) to concentrations of 40 wt.% and 20 wt.% are denoted here as “hexagonal” and “spherical”, respectively. Sodium chloride (NaCl) was added to select samples to induce a microstructural rearrangement of the surfactant molecules: 2% NaCl was added to 20 wt.% solutions (creating the “worm-like” sample) and 5% NaCl was added to 40 wt.% solutions (creating the “lamellar-40” sample). The salt percentage was calculated over the total mass of surfactant and water mixture. Surfactant, reverse osmosis water and additives were placed in sealed containers until complete dissolution and phase stabilization was achieved. The time scale for preparation of each sample varied from hours to several days depending on the final surfactant concentration.

The USV measurements required the use of an ultrasonic contrast agent within each specimen. All specimens were seeded with hollow glass spheres (Sigma Aldrich) with a density of 1.1 g.cm<sup>-3</sup> and an average diameter of 11 μm. Solutions containing 20 wt.% surfactant (*i.e.*, the spherical and worm-like micelle samples) were mixed with the glass spheres using a high shear mixer followed by a thermal equilibration. Other specimen (of hexagonal, lamellar-40, and lamellar-70 samples)

were mixed with the glass spheres using a vacuum mixer to avoid air entrapment. Specimen volume for every USV measurement was approximately 25 cm<sup>3</sup>.

### **3.2.2 Bulk shear rheometry measurements**

The shear stress and viscosity response of a specimen of each surfactant solution were measured using a rotational rheometer (Anton Paar MCR 702) paired with a 10 mm concentric cylinder. The shear stress and viscosity data are part of the flow characterization of the different surfactant solutions. Also, the flow data was used as initial screening tool to identify the critical shear rates for the onset of flow instabilities. The volume of each specimen was approximately 1.2 cm<sup>3</sup>. The application of shear followed a logarithmic ramp from the highest (100 s<sup>-1</sup>) to lowest shear rates (0.001 s<sup>-1</sup>). The parameters for data acquisition included strain control and steady state shear with 7 s of averaging per point.

### **3.2.3 Ultrasonic rheo-flow velocimetry measurements**

Flow velocimetry measurements were gathered using a Ultrasonic speckle velocimetry (USV) measurement technique. The details of the technique are explained in the introduction of this dissertation in section 1.4. However, the physical configuration of the equipment used at Purdue University and method development are described in the following paragraphs.

The USV system built at Purdue University utilizes an ultrasonic transducer (Panametrics PI50-2-R0.50) with central frequency of 36 MHz and approximate focal length of 12.7 mm. The transducer is controlled by the following set of equipment: a function generator (BK precision 20GHz 4040-B); an Olympus pulser receiver (5073PR) that produces electrical signals at 220 V and gains ranging between 0 to 40 dB; and a pre-amplifier (Olympus 5678) that amplifies the echo received by the ultrasonic transducer. A data acquisition PCI card (Agilent Digitizer U1084A) is used to convert the analog data into digital values, and custom MATLAB code is used for post-processing.

The USV system was used in combination with a rotational rheometer (Anton Paar MCR 302 ) and custom-machined concentric cylinder cell. The concentric cylinder cell was a precision machined fixture from polymethyl methacrylate. It included a 48-mm cylindrical rotor and surrounding semi-transparent cup, separated by a 0.83-mm gap. To ensure the transport of the

ultrasound waves as well as the uniform temperatures within the specimen, the concentric cylinder cell and ultrasonic transducer were fully immersed in a temperature-controlled water bath. This is a custom-built Plexiglas water chamber coupled with a JULABO water pump. Unless specified, all measurements (including bulk rheometry and USV) were conducted at 22°C.

The above equipment allows for a temporal resolution of 0.1 s to 100 s and a spatial resolution of approximately 42  $\mu\text{m}$ . The minimum and maximum allowable shear rate to measure are 0.2  $\text{s}^{-1}$  and 200  $\text{s}^{-1}$ , respectively.

The geometrical calibration of the hardware was achieved by measuring a liquid with proven Newtonian rheological response seeded with contrast agents (1 wt. %). The calibration protocol required the measurement of different shear rates (4, 10, 15, 20 and 30  $\text{s}^{-1}$ ) to manually fit parameters such as the initial position of the transducer respect the concentric cylinder fixture. The USV measurements were performed in conjunction with shear start-up tests, in which a constant shear rate is applied over time. Shear rates of 0.7, 7, and 70  $\text{s}^{-1}$  were selected based on bulk rheometry results as good reference points to compare in every specimen. An exception was made for the hexagonal sample (40 wt.% surfactant, no added salt) which exceeded the torque limit of the rheometer. Hexagonal sample was investigated to shear rates of 0.5 and 1  $\text{s}^{-1}$  only. A single specimen of each surfactant solution was used to evaluate the three different shear rates in descending order, and 30 s of pre-shear was applied before each measurement. Thus, for each specimen: 100  $\text{s}^{-1}$  pre-shear was applied before the 70  $\text{s}^{-1}$  shear start-up measurement; 10  $\text{s}^{-1}$  pre-shear was applied before the 7  $\text{s}^{-1}$  measurement; and 1  $\text{s}^{-1}$  pre-shear was applied before the 0.7  $\text{s}^{-1}$  measurement. The reason for descending shear rate procedure and the application of pre-shear was to homogenize the specimen and to avoid transient, history-dependent effects during the velocimetry measurements. Additionally, the measurements for each specimen started after 30 s of shearing to ensure that a steady state behavior was achieved.

In this chapter, velocimetry data is expressed as velocity,  $v$ , in  $\text{mm}\cdot\text{s}^{-1}$  as a function of gap length,  $x$ , in mm. The point  $x = 0$  mm represents the position within the specimen directly adjacent to the rotor (*i.e.*, the moving wall) while  $x = 0.83$  mm represents the position of the specimen adjacent to the stationary wall. Thus, for an ideal Newtonian specimen displaying uniform simple shear and

no wall-slip,  $v(0)$  should equal the velocity of the moving wall (calculated as the applied shear rate multiplied by the gap length),  $v(0.83 \text{ mm})$  should be zero, and all other  $v(x)$  data (*i.e.*, local velocities within the volume of the specimen) will adopt a linear decay. Another illustrative plot used in this study is of the normalized velocity ( $v / v_0$ ) as a function of normalized gap ( $x / x_0$ ), where  $v_0$  is the velocity of the moving wall and  $x_0$  is the gap length (0.83 mm). Then, the resulting plot for an ideal Newtonian specimen will consist of data points organized along the line between point (0, 1) and (1, 0) and any deviation from linearity may indicate the presence of shear-induced flow instabilities within the volume of the specimen. Both illustrative plots are displayed in Figure 3-2.

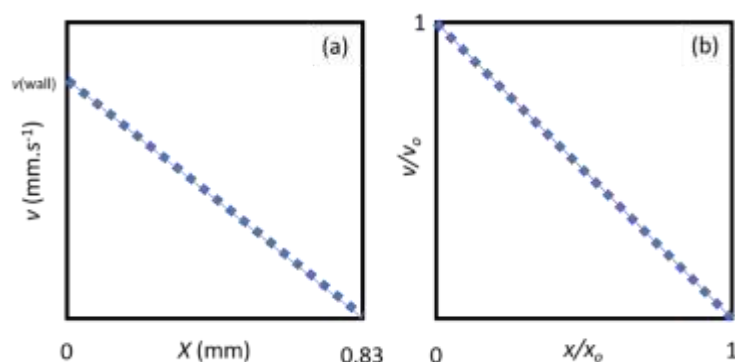


Figure 3-2 Illustration of the velocimetry data. (a)  $v$ , in  $\text{mm}\cdot\text{s}^{-1}$  as a function of gap length,  $x$ , in mm (b) normalized velocity ( $v / v_0$ ) as a function of normalized gap ( $x / x_0$ ). Dots and line represent the expected behavior for a Newtonian response. Any deviation from this response may indicate the presence of a shear induced flow instability.

### 3.2.4 Microstructural characterization

#### 3.2.4.1 Small-angle x-ray scattering

In this study, different solution of SLE<sub>1</sub>S were formulated to recreate specific microstructural organizations. Hence, small-angle X-ray scattering (SAXS) measurements were performed to confirm that the surfactant solutions of interest contained the expected model microstructure. SAXS is a characterization technique that utilizes the scattering of an X-ray beam by electrons in a material to obtain averaged measurements of a material's structure and long-range nanoscale order. Depending on the density of the electron cloud and arrangement relative to neighboring species, a given molecule or molecular assembly will scatter X-rays at particular intensities and

angles. Condensed assemblies such as surfactant micelles, with higher electron densities than the surrounding medium, would produce a unique scattering pattern indicating the average shape of the assemblies (*e.g.*, spherical or worm-like) and an average size parameter (*e.g.*, diameter or length). For repeating structures such as lyotropic organizations, multiple reflections will appear within the scattering pattern. The ratio of the scattering vector of higher order reflections to that of the primary reflection can be used to determine the nature of the repeat unit (*e.g.*, lamellar or hexagonal) and a domain size parameter (*e.g.*, center-to-center distance). A full explanation of this technique can be found elsewhere.<sup>53</sup>

All SAXS measurements were conducted in an independent experiment using an Anton Paar SAXSpoint 2.0 system (note: this is a conventional SAXS machine that is *not* coupled with any rheometry systems). For each experiment, the specimen was placed in a paste cell containing Kapton windows and sealed with rubber O-rings to withstand vacuum pressure. Data for all samples was collected at a sample-to-detector distance (SDD) of 363 mm using an incident X-ray beam of 50.047 keV and 0.999 mA with a wavelength of 1.54 Å. For each specimen, three frames of 300 s exposures were collected and averaged. Intensity values are reported in arbitrary units.

#### **3.2.4.2 Optical microscopy and flow birefringence**

A CSS450 optical shear stage (Linkam Scientific, Tadworth UK) was used to visualize the microstructural as a function of flow of the lamellar-70 sample. The optical shear stage is a parallel plate cell with glass plates and a viewing window located at 7.5 mm off center; the gap and rotational velocity are electronically controlled. The vertical gap was set to 100 μm, and temperature set constant at 25°C. The stage was mounted on a Motic upright microscope (BA410E) fitted with 5x LM Plan lens (NA 0.13) and 20x lens (NA 0.4). Crossed polarizers above and below the stage were placed at 45° with respect to the flow across the window, such that optical retardance with the flow direction was maximized. Images were acquired using a QICam Fast 1394, color 12-bit camera controlled by Metamorph 7.7 software (Molecular Devices). Exposure times varied from 25 ms (for lamellar samples) and 150 ms (for worm-like samples). For flow birefringence measurements, the mean intensity across the field of view was tracked per frame during time-lapse acquisition. Specimens were tested immediately after preparation.

Static polarized light imaging was achieved with the same software and camera equipped to a Zeiss Axioskop microscope with Plan NEOFLUAR Pol 10x (0.50NA) and 20x (0.30NA) objective lenses and 0.9NA condenser lens.

### 3.3 Results

#### 3.3.1 X-ray scattering patterns

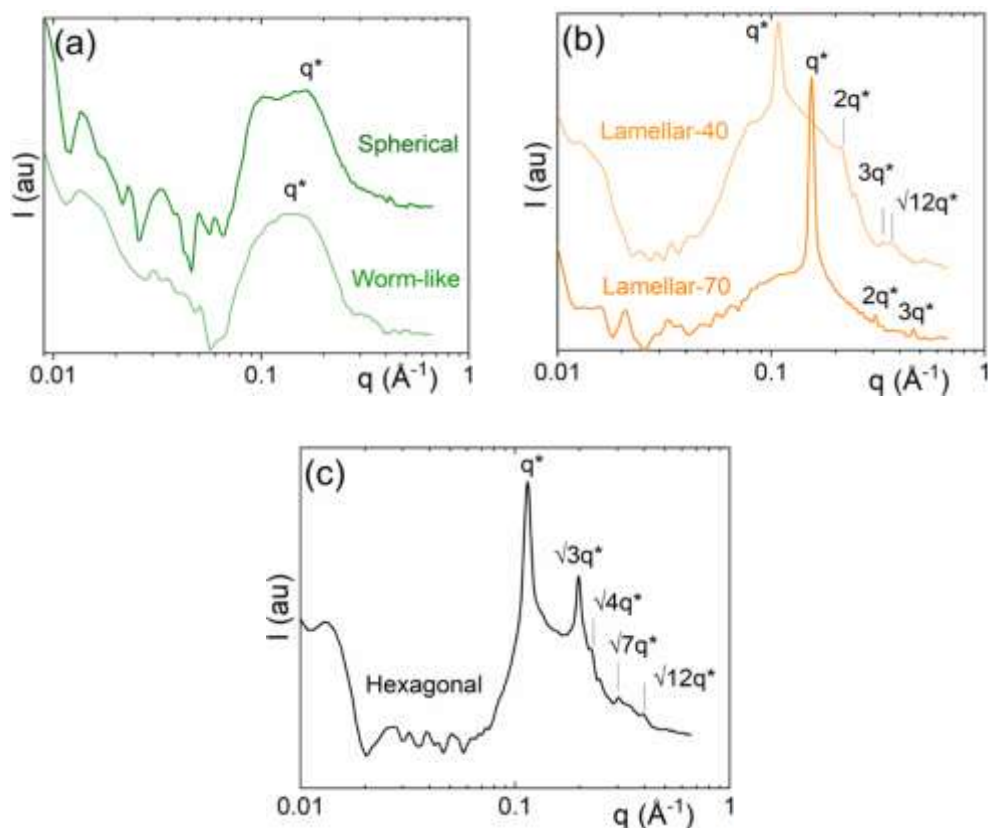


Figure 3-3 Small-angle X-ray scattering patterns for the surfactant solutions: (a) 20 wt.% SLE<sub>1</sub>S with 0% NaCl (spherical micelle sample) and 20 wt.% SLE<sub>1</sub>S with 2% NaCl (worm-like micelle sample); (b) 40 wt.% SLE<sub>1</sub>S with 5% NaCl (lamellar-40 sample) and 70 wt.% SLE<sub>1</sub>S (lamellar-70 sample); (c) 40 wt.% SLE<sub>1</sub>S (hexagonal sample)

Figure 3-3 displays all the results from SAXS characterization. First, Figure 3-3a shows the patterns for specimens from spherical and worm-like samples. A broad reflection at  $q = 0.1635 \text{ \AA}^{-1}$  for the spherical and  $q = 0.1414 \text{ \AA}^{-1}$  for the specimen worm-like are observed. The reflection  $q = 0.1635 \text{ \AA}^{-1}$  suggest the existence of polydisperse spherical micelles with an average diameter of

38.4 Å, and, the reflection  $q = 0.1414 \text{ \AA}^{-1}$  suggest that the addition of salt increased the average size of the micelles to 44.4 Å.

Next, Figure 3-3c shows the pattern of the specimen from Hexagonal sample. Observed reflections at ratios of 1,  $\sqrt{3}$ ,  $\sqrt{4}$ ,  $\sqrt{7}$ , and  $\sqrt{12}$  times  $q^*$ , indeed confirm the presence of a uniform hexagonally packed structure.<sup>54</sup> The calculated domain size parameter for Hexagonal sample is  $d = 55.0 \text{ \AA}$ .

Finally, Figure 3-3b shows the pattern for specimens from Lamellar-40 (40 wt.% surfactant solution with 5 wt.% NaCl), and specimens from Lamellar-70 (70 wt.% surfactant solution). The pattern for Lamellar-40 displays a shift from the hexagonally packed structure to a mixture of hexagonal and lamellar structures. It is observed that the characteristic lamellar reflections dominate over the hexagonal reflections (1, 2, and 3 times  $q^*$  are characteristic of a lamellar structure). The average domain size parameter for the Lamellar-40 was  $d = 58.1 \text{ \AA}$ . Similarly, the pattern for the specimen from Lamellar-70 displayed distinct reflections at 1, 2, and 3 times  $q^*$ , indicating a uniform lamellar structure with a domain size (center-to-center distance between lamellae) of 40.5 Å.

### 3.3.2 Bulk shear rheometry results

Figure 3-4 displays the stress response to increasing applied shear rates for all samples. Newtonian behavior is found in the spherical sample (Figure 3-4a). It is observed that the shear stress ( $\tau$ ) increased linearly with increasing shear rate ( $\dot{\gamma}$ ) according to  $[\tau = \eta\dot{\gamma}]$ , with a viscosity value ( $\eta$ ) of 6.1 mPa.s, roughly six times that of water. The behavior of the worm-like sample was shear rate dependent (Figure 3-4a). Newtonian behavior was observed at  $< 5 \text{ s}^{-1}$  and shear thinning was observed at greater rates, following a power-law  $[\tau = k\dot{\gamma}^n]$  with index ( $n$ ) of 0.14 and consistency ( $k$ ) of 74 Pa.s .

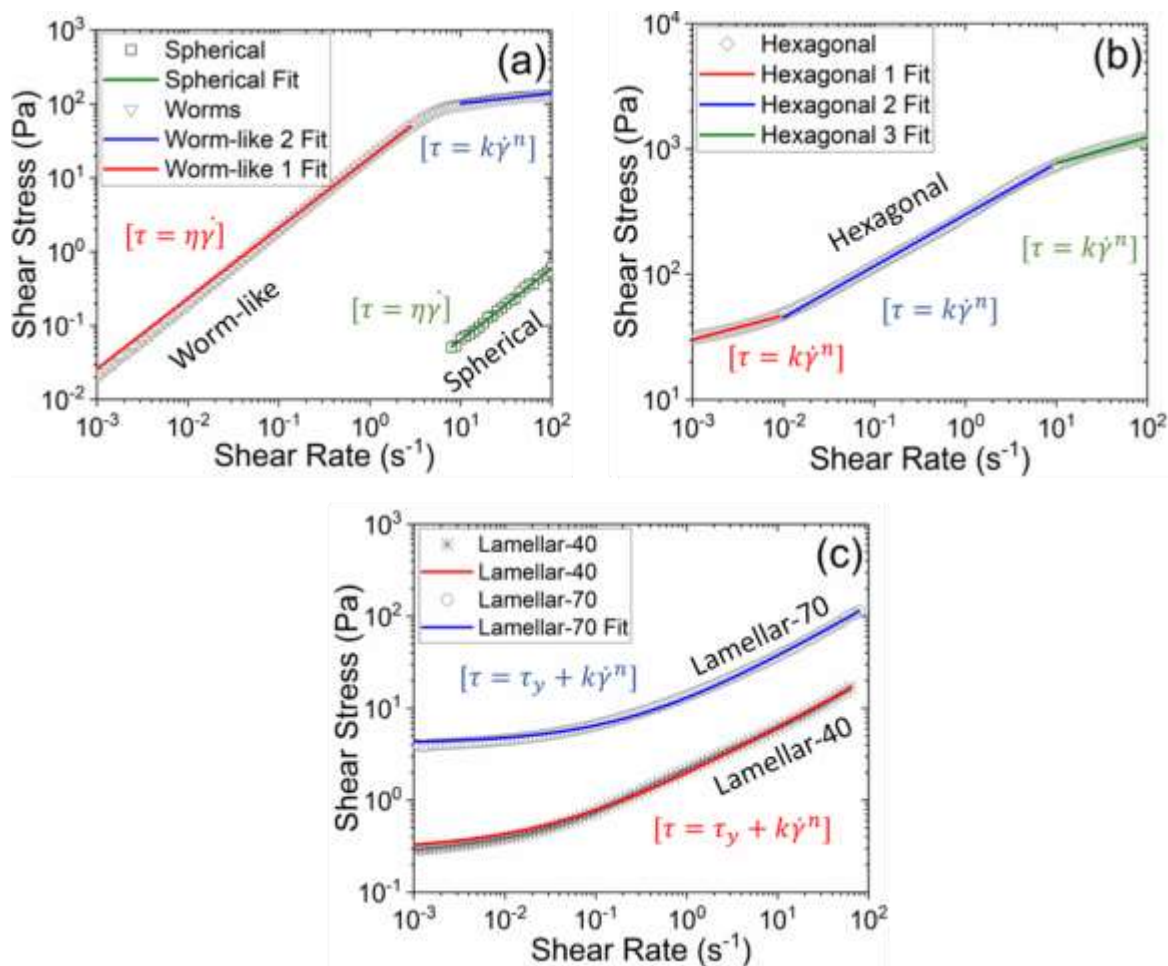


Figure 3-4 Flow curve and mathematical fitting for all surfactant solutions. (a) spherical (squares) and worm-like (triangles) sample (b) Hexagonal sample (diamonds) (c) lamellar-40 (starts) Lamellar-70 (circles) samples. The solid line represents the applied models (as described in the manuscript) and the semi-transparent symbols are the raw data points. The symbols in the equations stand for shear stress ( $\tau$ ), shear rate ( $\dot{\gamma}$ ), power index ( $n$ ), viscosity ( $\eta$ ), yield stress ( $\tau_y$ ), and consistency ( $k$ ). Origin 2018b linear and non-linear fitting tool was used

A general strong shear thinning response is observed in the hexagonal sample over the full range of investigated shear rates (Figure 3-4b). Two points of inflection occurring at shear rates of  $\sim 0.01$  s<sup>-1</sup> and  $10$  s<sup>-1</sup> were observed. Qualitatively, the hexagonal sample fit the description of a yield stress fluid with an apparent yield stress ( $\tau_y$ ) of 31 Pa. However, the Herschel-Buckley model, a model that is commonly used to describe yield stress fluids, did not describe accurately the experimental data.<sup>45</sup> Instead, three different power laws at shear rate ranges of  $0.001$  to  $0.01$  s<sup>-1</sup>,  $0.01$  to  $10$  s<sup>-1</sup>, and  $10$  to  $100$  s<sup>-1</sup>, with  $n = 0.19$ ,  $0.41$ , and  $0.20$  and  $k = 115$ ,  $301$ ,  $480$  Pa.s, respectively were used to describe the shear stress response. Interestingly, the strong shear thinning behavior shown in

Figure 3-4b is inconsistent with actual observations of sample Lamellar-40—*e.g.*, it does not flow under gravity, and it fractures, slips, and squishes when touched.

Different magnitude of yield stress fluid responses (with a strong shear thinning behavior) were captured using the Herschel-Bulkley model [ $\tau = \tau_y + k\dot{\gamma}^n$ ] for sample Lamellar-40 and Lamellar-70 (Figure 3-4b). The experimental data of Lamellar-40 yield to  $n = 0.54$ ,  $k = 1.71$  Pa.s, and  $\tau_y = 0.29$  Pa fitting parameters. Similarly, Lamellar-70 yield to  $n = 0.57$ ,  $k = 8.9$  Pa.s, and  $\tau_y = 4.1$  Pa fitting parameters.

### 3.3.3 Results from advanced rheo-physical measurements

Figure 3-5 shows the results for the shear start-up test used while performing USV experiments. The seemingly constant shear stress behavior on all samples suggest that the designed descending shear rate procedure and the application of pre-shear indeed homogenized the specimen avoiding transient and history-dependent effects during the velocimetry measurements.

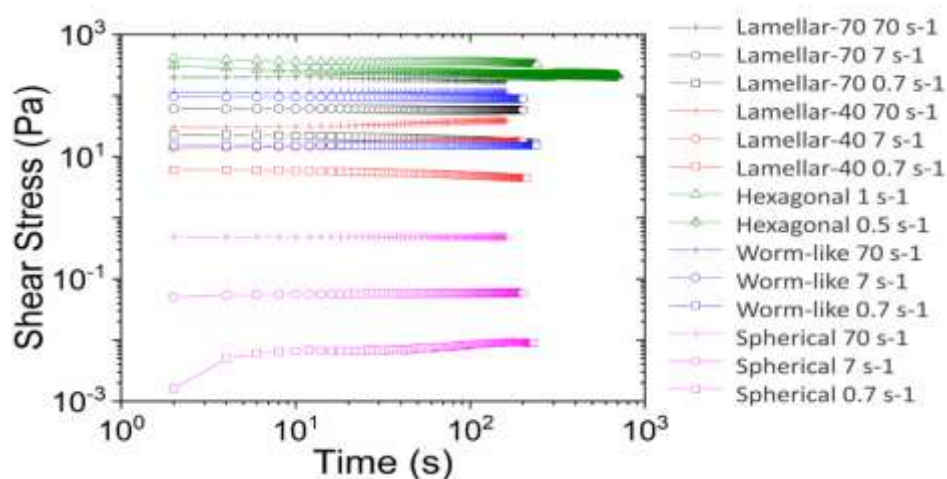


Figure 3-5 Flow-velocimetry shear start-up data for the following specimens: spherical sample, worm-like sample, hexagonal sample lamellar-40 sample, and Lamellar-70 sample. Shear stress response over time is presented in a log-log scale

Even though the rheological response in Figure 3-4 and Figure 3-5 are measured using different fixtures, there was good agreement between the steady state values of stress in the shear start-up tests (Figure 3-5) performed during the advance rheo-physical measurements and the associated values of stress in the flow curves (Figure 3-4) as shown in Figure 3-6. Figure 3-6 shows the shear

stress plateau for each shear rate and sample superimposed on the flow curve for each sample. For all samples and investigated shear rates, the velocimetry measurements were performed after the specimen had achieved steady state behavior (sufficient time for the shear stress response to become constant, or nearly so was allowed).

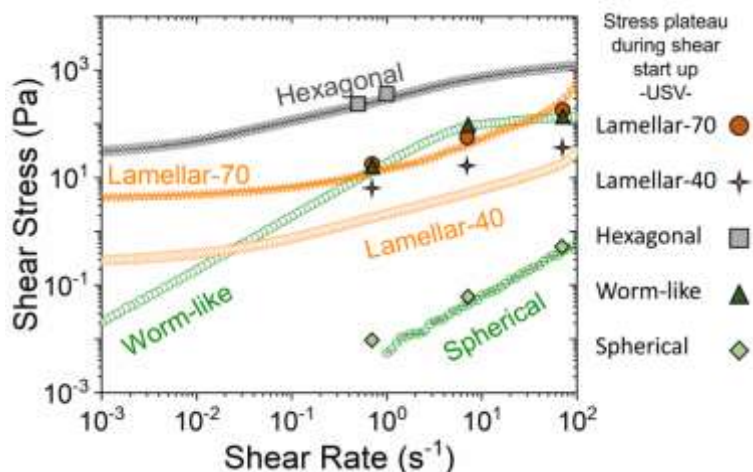


Figure 3-6 Flow curve and USV shear stress plateau relationship for: spherical sample, worm-like sample, hexagonal sample, lamellar-40 sample, and Lamellar-70 sample. The superimposed symbols represent the flow velocimetry shear stress plateaus at the different experimental shear rates:  $0.7 \text{ s}^{-1}$ ,  $7 \text{ s}^{-1}$  and  $70 \text{ s}^{-1}$  for the spherical (diamonds), worm-like (triangles), lamellar-40 (stars) and lamellar-70 (circles) samples and  $0.5 \text{ s}^{-1}$  and  $1 \text{ s}^{-1}$  for the hexagonal (squares) sample.

The characterization of the rheo-physical behavior of the different surfactant solutions involved the measurement of the 1D local velocity profile: rheo-flow velocimetry. USV measurements were performed at fixed shear rate values of  $0.7 \text{ s}^{-1}$ ,  $7 \text{ s}^{-1}$ , and  $70 \text{ s}^{-1}$  for the spherical, worm-like, and lamellar samples and  $0.5 \text{ s}^{-1}$  and  $1 \text{ s}^{-1}$  for the hexagonal sample.

Figure 3-7 displays the rheo-flow velocimetry results for all surfactant solutions characterized using the USV system at Purdue. The spherical micelle sample (Figure 3-7a) was the only sample that exhibited a velocity profile with nearly linear, simple shear behavior at all three investigated shear rates, as indicated by the good agreement of the data points with the dashed lines in the plot.

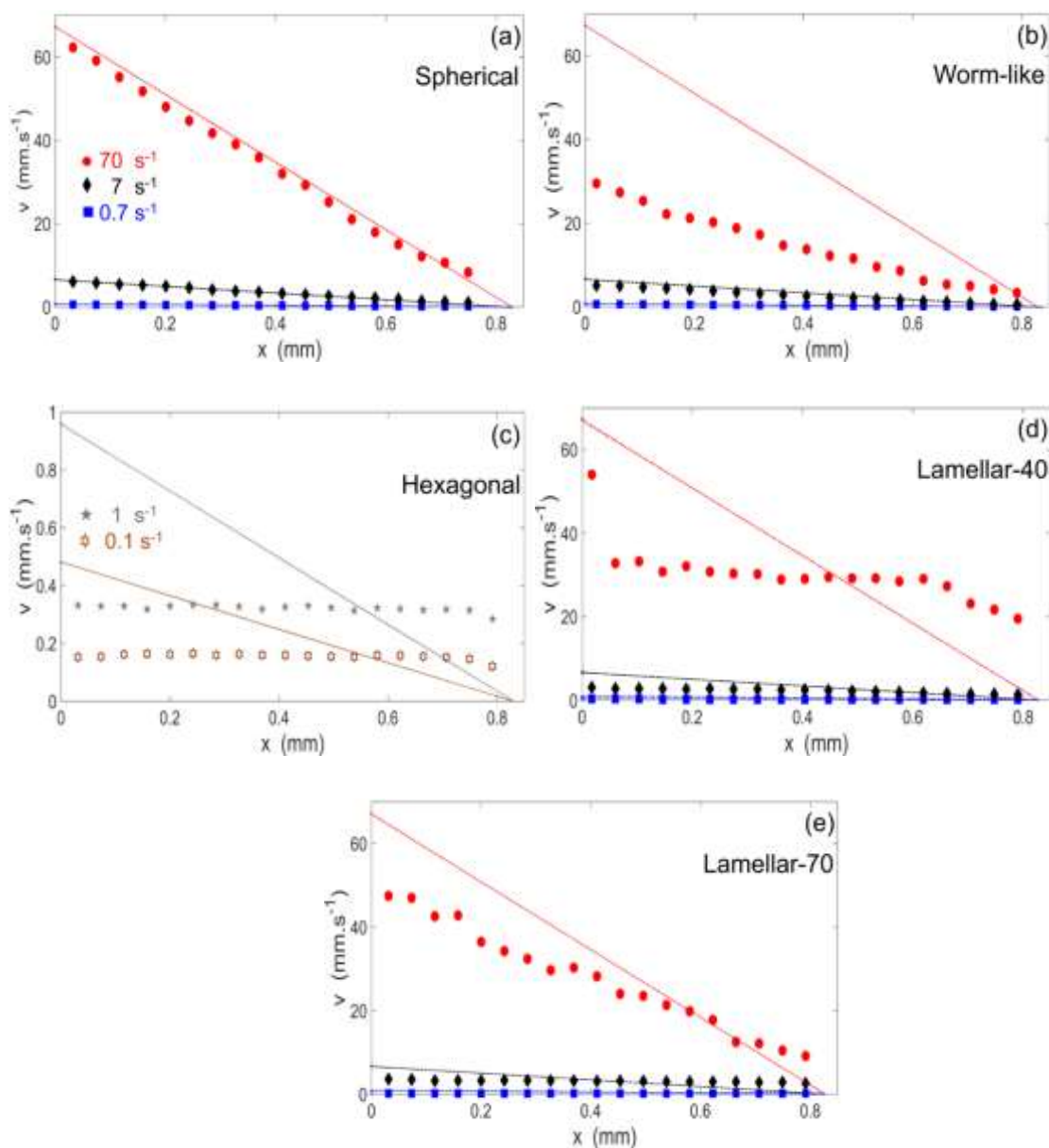


Figure 3-7 Rheo-flow velocimetry results for three different applied shear rates,  $70 \text{ s}^{-1}$  (red circles),  $7 \text{ s}^{-1}$  (black diamonds), and  $0.7 \text{ s}^{-1}$  (blue squares), for the following surfactant solutions: (a) 20 wt.% SLE<sub>1</sub>S with 0% NaCl (spherical sample); (b) 20 wt.% SLE<sub>1</sub>S with 2% NaCl (worm-like sample); (d) 40 wt.% SLE<sub>1</sub>S with 5% NaCl (lamellar-40 sample); and (e) 70 wt.% SLE<sub>1</sub>S (lamellar-70 sample). For the (c) 40 wt.% SLE<sub>1</sub>S (hexagonal sample),  $0.5 \text{ s}^{-1}$  (gray pentagrams) and  $1 \text{ s}^{-1}$  (brown hexagrams) were the applied shear rates. In every plot, the colored lines indicate the simple shear velocity profile expected for each applied shear rate

The worm-like micelle sample (Figure 3-7b) exhibited simple flow characteristics only at the lowest applied shear rate ( $0.7 \text{ s}^{-1}$ ). At the intermediate shear rate of  $7 \text{ s}^{-1}$ , the specimen appeared to slip at the moving wall. There is evidence of a reduced magnitude of the velocimetry data in direct

proximity to the moving wall from its expected value. However, the deviation is small to conclude effectively. Conversely, at the highest investigated shear rate of  $70 \text{ s}^{-1}$ , the deviation of the velocimetry data from the dashed line is clearly seen in Figure 3-7b indicating the disruption of wall-sample grip: wall-slip is induced. (note: this is better highlighted by the normalized velocity plots in the discussion section).

The hexagonal sample (Figure 3-7c) displayed evidence of strong wall-slip at both the moving and stationary walls of the rheometer fixture while maintaining a nearly constant velocity throughout its volume, thus adopting a velocity profile characteristic of plug flow. This plug flow response was observed for both values of applied shear rate.

The lamellar-40 sample (Figure 3-7d) exhibited plug flow-like behavior, though not as idealized as the behavior displayed by the hexagonal sample as not all portions of the specimen volume deformed at a constant velocity (*e.g.*, the region near the stationary wall,  $x \approx 0.6\text{-}0.8 \text{ mm}$ ). For the lamellar-40 sample, wall-slip was also observed. At  $70 \text{ s}^{-1}$ , evidence of a discontinuity was observed at  $x \approx 0\text{-}0.8 \text{ mm}$ , as neighboring velocimetry measurements reported very different values. Specifically, the velocimetry data representing a layer of solution  $\sim 80 \text{ }\mu\text{m}$  in thickness near the moving wall was approximately 75% of the wall velocity but all data between  $80\text{-}600 \text{ }\mu\text{m}$  was approximately 50% of the wall velocity.

The lamellar-70 sample (Figure 3-7e) was perhaps the most interesting sample as the basic rheology was similar to the lamellar-40 sample (Figure 3-7d) but with a strikingly different velocity profile at the highest shear rate. At low shear rates ( $0.7$  and  $7 \text{ s}^{-1}$ ), the lamellar-70 sample exhibited plug flow behavior with wall-slip at both the moving and stationary walls. However, at  $70 \text{ s}^{-1}$ , a behavior more like simple shear was observed and there was no evidence of a discontinuous velocity profile, such as the one observed in the lamellar-40 sample.

### 3.3.4 Polarized light microscopy and birefringence observations

Crossed-polarized imaging and flow birefringence were used to complete the structural characterization of the SLE<sub>1</sub>S samples. Figure 3-8 displays the micrographs of the expected microstructural phases (liquid crystalline patterns of common surfactant phases) under cross-

polars as a function of relative shear<sup>55</sup>. The birefringence of surfactant microstructures changes respect to their orientation with respect to the polarized illumination. For instance, with gently preparation and minimal shear during loading, the lamellar-70 sample exhibited randomized domains of optically-isotropic, dark sheets (see Figure 3-8a, blue arrow) and optically anisotropic oily streaks that appeared bright (Figure 3-8a, white arrow). Multilamellar vesicles, which are rolled-up sheets spheres consisting of concentric layers (onion-like) exhibit Maltese-cross patterns (Figure 3-8b, white arrow); formed here by dispersing SLE<sub>1</sub>S in 1 Pa-s silicone oil. Now, if shear is applied back and forth uniaxially while mounted on the microscope slide, the lamellar-70 sample from Figure 3-8a resulted in aligned oily streaks as shown in Figure 3-8c. In the same way of preparation, a sheared lamellar-40 sample (Figure 3-8d) displayed a lower concentration of oily streaks than the lamellar-70 sample (Figure 3-8c) due to the differences in surfactant and salt concentrations. Lastly, the fan-like patterns of the hexagonal sample were visible after significant applied shear between the microscope slides (Figure 3-8e).

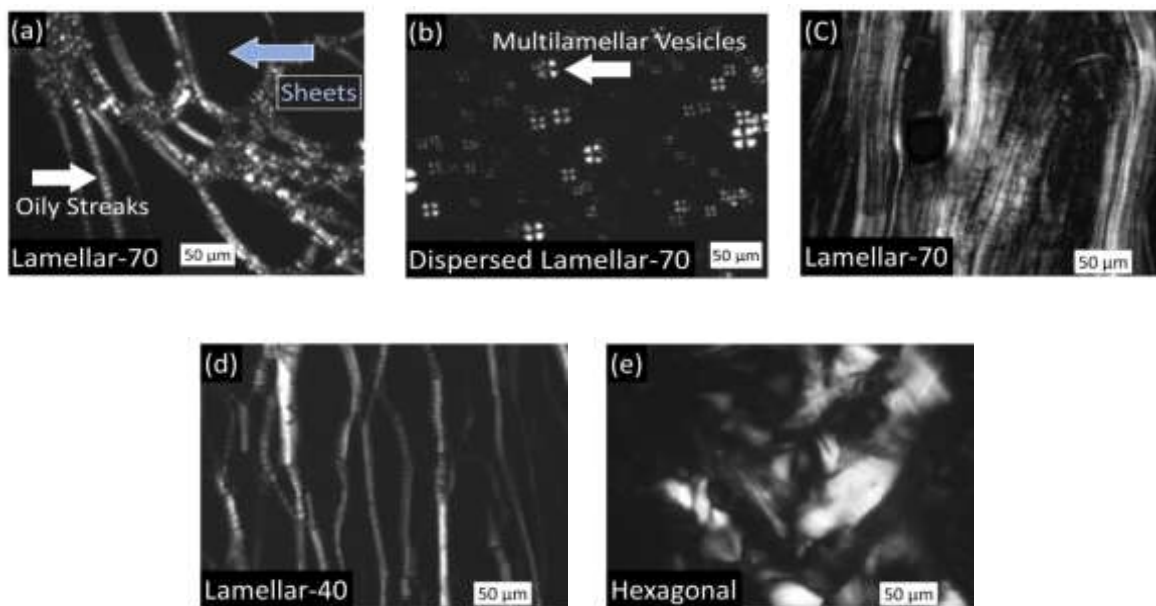


Figure 3-8 Light microscopy (crossed-polarized) of 70 wt.% SLE<sub>1</sub>S (lamellar-70 sample) at rest (a); dispersed in silicone oil to demonstrate MLV patterns (b); and after shear (c); (d) 40 wt.% SLE<sub>1</sub>S with 5% NaCl (lamellar-40 sample) after shear; (e) 40 wt.% SLE<sub>1</sub>S (hexagonal sample) after shear

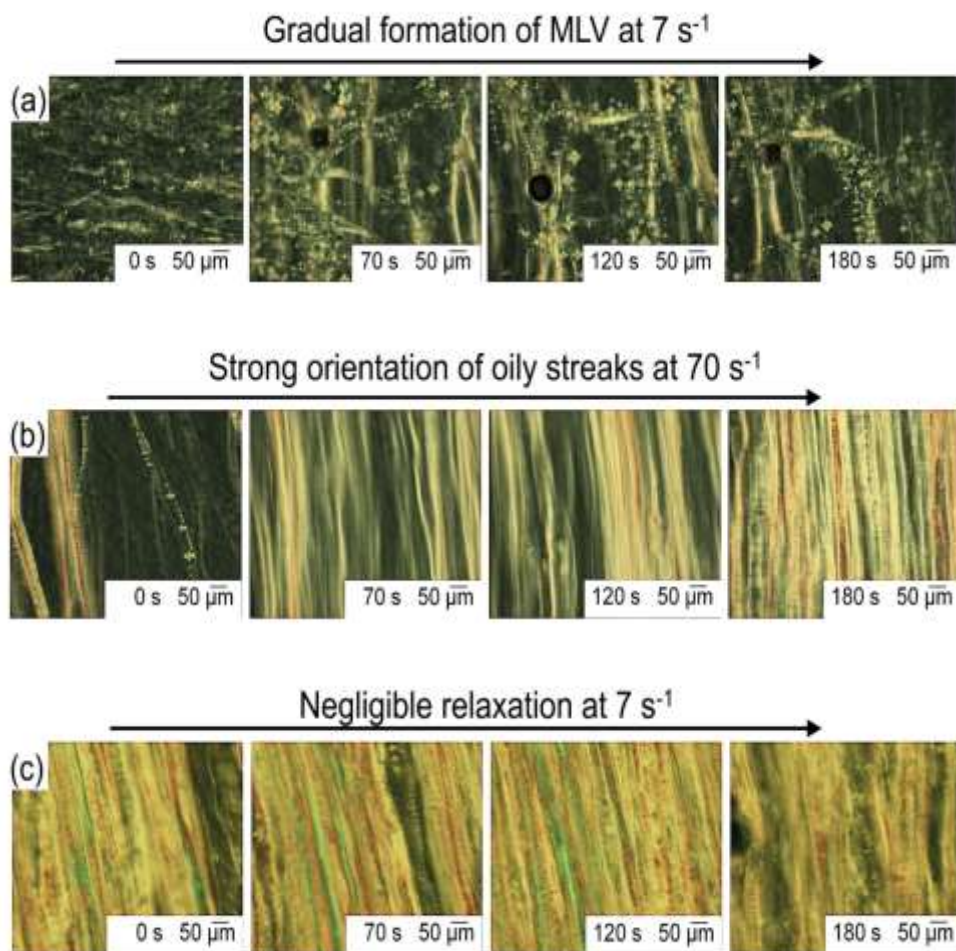


Figure 3-9 Polarized light imaging of 70 wt.% SLE<sub>1</sub>S (lamellar-70 sample) in the Linkam shear stage illustrating shear-induced microstructural rearrangement during consecutive 3-minute intervals of rotation at (a) 7 s<sup>-1</sup>, (b) 70 s<sup>-1</sup>, and (c) 7 s<sup>-1</sup> (note that direction of flow is from top to bottom in each image)

The static microstructure of concentrate surfactants can vary if shear is continuously applied. Figure 3-9 is composed of time-lapsed snapshots of the microstructural evolution of the lamellar-70 sample at various, constant shear rates. The first image (at time-zero) is taken after sample loading but prior to any applied shear. This first image exhibited many liquid crystalline domains that were randomly oriented, so the image was relatively dark compared to subsequent ones (Figure 3-9a). Oily streaks and some MLVs organized as 7 s<sup>-1</sup> was applied for 3 minutes. As shown in Figure 3-9b, higher shear rates (70 s<sup>-1</sup>) increased the rate of assembly, producing optically brighter oily streaks aligned with the flow direction (top to bottom). With increasing duration of shear, oily streaks became more and more organized with the flow. Finally, to test reversibility

and relaxation rates, a final interval of low shear ( $7 \text{ s}^{-1}$ ) was applied (see Figure 3-9c). The crystalline lamellar superstructures did not display strong evidence of relaxation or reorganization during experimental timescales (order of minutes).

### 3.4 Discussion

As mentioned in the introduction, this study attempted to evaluate the quality of information about a model surfactant solution that was obtained from flow curve measurements. To conduct this evaluation, with a focus on potentially uncovering the solutions' true rheological responses and thus determining accurate structure-property relationships, connections were established between the shear rheometry data (Figure 3-4), rheo-flow velocimetry data (Figure 3-7), and flow-imaging results (Figure 3-8, and 6), coupled with prior knowledge about surfactant solution formulation and phase behavior (Figure 3-1).

#### 3.4.1 Newtonian behavior of the spherical micelle sample

The sample containing 20 wt.% SLE<sub>1</sub>S formed spherical micelles in solution as expected. The transformation into ordered structures of surfactant molecules was driven by the endless battle between the entropy and enthalpy to lower the total energy of the system.<sup>56</sup> The formation of micelles (spherical in this case) requires adequate amounts of surfactant and/or counterions<sup>57</sup>; 20 wt.% surfactant in solution was expected to be enough to form spherical micelles because this concentration was far above the expected critical micelle concentration (0.023 wt.%).<sup>58</sup> SAXS results confirmed the presence of spherical micelles and did not show any evidence of a long-range arrangement. Lacking long-range order, it was thus expected that the dilute solution of spherical micelles exhibited Newtonian behavior analogous to hard spheres in a sea of solvent.<sup>9 59 60</sup> This expectation was consistent with the flow curve in Figure 3-4 and velocity profiles in Figure 3-7a. The velocity profiles are presented in normalized inset-plots in Figure 3-10 for direct comparison with the respective flow curve. The Newtonian, simple shear response was a consequence of the displaced volume of solvent that each sphere produced; that is, micelle-micelle interactions were negligible compared to the hydrodynamic drag that each micelle produced during deformation.<sup>61</sup>  
<sup>62</sup> A deviation between the velocimetry data and the expected simple shear response was observed at the lowest shear rate, most likely a consequence of slight fluctuations of the applied shear rate due to the finite torque sensitivity of the stress-controlled rheometer.

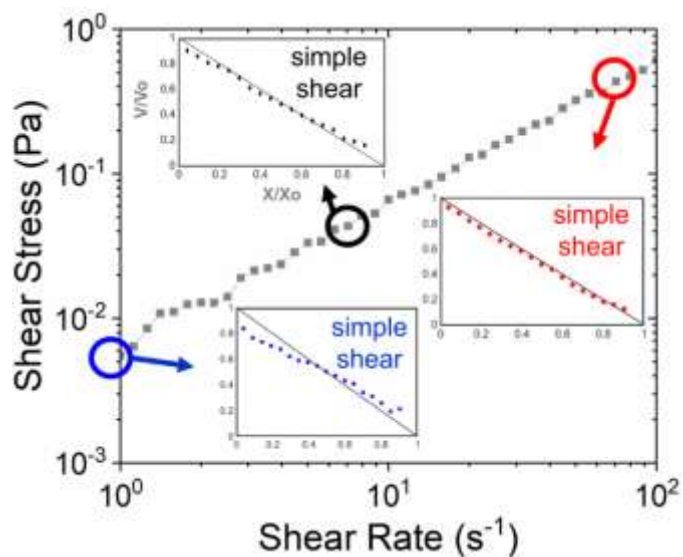


Figure 3-10 Spherical sample: flow curve and flow velocimetry relationship. Flow curve data from Figure 3-4a and local velocity profiles at three shear rates from Figure 3-7a. Inset plots display the normalized velocity as a function of normalized gap

### 3.4.2 Bimodal behavior of worm-like micelle sample

The worm-like micelle sample was created with the addition of 2% NaCl to the 20 wt.% surfactant solution. The addition of counterions (*i.e.*,  $\text{Na}^+$ ) screened the anionic head groups of the surfactant molecules<sup>63</sup> so that the micelles transformed from spheres into elongated, cylindrical geometries.<sup>9</sup> These worm-like micelles have remarkable structural stability as well as regenerative properties (*i.e.*, the ability to break and reform in solution) and are widely used in the lubricant, pharma, and personal and home care industries.<sup>63 64</sup>

X-ray scattering was used to verify the microstructure of this sample at the Angstrom-level. SAXS characterization suggested a larger micelle diameter compared to the spherical sample and no long-range order. This implies that the worm-like micelles were isotropic and amorphously entangled at rest, and the measured micelle size indicated the average diameter of the worms. While it can be difficult to confirm the presence of cylindrical micelles using SAXS, the characteristic signatures of these structures have been observed using flow birefringence measurements in surfactant systems with analogous formulations.<sup>65 66</sup>

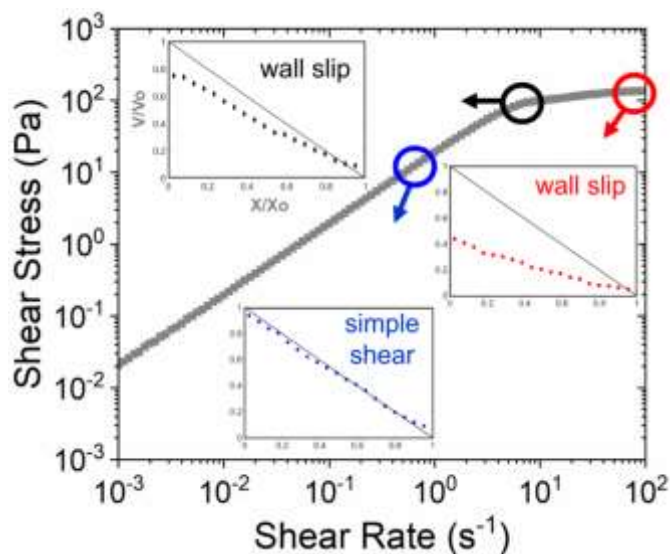


Figure 3-11 Worm-like sample: flow curve and flow velocimetry relationship. Flow curve data from Figure 3-4a and local velocity profiles at three shear rates from Figure 3-7b. Inset plots display the normalized velocity as a function of normalized gap

The flow curve of the worm-like sample displayed a Newtonian response at low shear rates and shear thinning behavior at higher rates, as previously reported by many others.<sup>63 67 68</sup> As expected, the Newtonian response corresponded with a simple shear velocity profile (see Figure 3-11). Also shown in Figure 3-11, at the approximate onset of shear thinning, slight wall-slip was observed which increased in magnitude at higher applied shear rates. Thus, the measured shear thinning response was not representative of the bulk sample but was instead a consequence of shear-induced wall-slip.

Usually, the bimodal rheology of samples containing worm-like micelles is attributed to the shear-induced formation of bands of different viscosities.<sup>20 67 69</sup> However, velocimetry results did not show strong evidence of shear band formation, which is typically manifest as a “kink” (change of slope) in the velocity profile. Some have found that the formation of shear bands can be delayed or even prevented if wall-slip is present.<sup>70</sup> Thus, as shear bands were not observed here, their formation was most likely prevented by the slippage that occurred at medium ( $7 \text{ s}^{-1}$ ) and high shear rates ( $70 \text{ s}^{-1}$ ). From a molecular viewpoint, if the adhesive forces between the solution and fixture walls are weaker than the cohesive forces within the solution, stress will be relaxed (deformation energy released) by the formation of a zone of high shear at the solution-wall interface – *i.e.*, the

occurrence of wall-slip will reduce the likelihood (and energetic driving force) for other flow instabilities to nucleate.<sup>37 70</sup>

### 3.4.3 Plug flow of the hexagonal sample

The increased surfactant concentration produced a transition from dense spherical micelles at 20 wt.% to a hexagonal organization of elongated cylindrical micelles at 40 wt.%.<sup>71</sup> The flow curve response of the hexagonal sample was shear thinning over all investigated shear rates, consistent with previous studies.<sup>71 72</sup> However, signatures of plug flow were observed in the rheo-flow velocimetry results (see Figure 3-12). Thus, the sheared hexagonal sample was not uniformly shear thinning through its volume. Instead, deformation appeared to be localized to regions of the solution that were directly adjacent to the moving and stationary walls. These shear thinning “lubrication layers”, as they are sometimes called,<sup>44 73</sup> facilitated the motion of the bulk plug of solution.

Compared to disordered cylindrical micelles and lamellar phases, others have shown that the hexagonal phase of surfactant solutions typically exhibits greater viscoelasticity due to increased interactions between neighboring micelles in the hexagonally packed microstructure.<sup>72</sup> So even though it cannot be directly measured here, the plug of solution was assumed to have a rheological response similar to a viscoelastic solid based on observations of the solution during sample preparation. What was detected in the basic rheometry experiments was the shear thinning response of the lubrication layers that effectively surround the viscoelastic plug within the solution. And while velocimetry measurements were not possible within these layers due to the 42- $\mu\text{m}$  spatial resolution of the USV system, here an attempt is made to explain the molecular-level mechanisms that are responsible for the shear thinning behavior observed in the flow curve based entirely on the known microstructure of the sample, *i.e.*, hexagonally close packed cylindrical micelles.

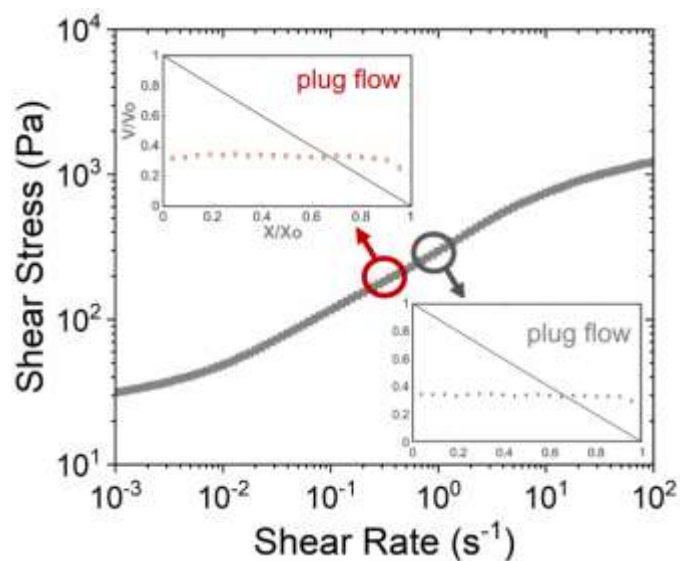


Figure 3-12 Hexagonal sample: flow curve and flow velocimetry relationship. Flow curve data from Figure 3-4b and local velocity profiles at three shear rates from Figure 3-7c. Inset plots display the normalized velocity as a function of normalized gap

Deformation of a hexagonal phase is the result of cooperative and associative movement of small elastic units (*i.e.*, solid-like domains).<sup>72-74</sup> Hexagonal domains do not have a mesoscopic uniform orientation; thus, each domain requires a specific level of energy to move and rotate before it completely aligns in the direction of the flow, contributing to a mesoscopic-type movement. Therefore, critical shear rates can produce movement of specific domains, *e.g.*, those in contact with the fixture walls, which lead to the creation of a transient, friction-reducing lubricating layer. Once the lubrication layers are created, the viscoelastic plug effectively disengages from the moving wall and acquires a lower flow velocity. This behavior will persist until a critical level of strain is surpassed, generating an effective orientation of an adjacent layer of hexagonal domains.<sup>72</sup> These critical strain values required for mesoscopic movement may explain the different power laws observed in the flow curve of hexagonal sample. And as more hexagonal domains in the lubrication layer align in the flow direction, less torque is required to achieve the same applied shear rate, yielding a shear thinning response.

### 3.4.4 Apparent yield stresses of lamellar samples

In the context of this study, lamellar-40 and lamellar-70 samples were designed to be model concentrated surfactant solutions that behave as yield stress fluids.<sup>75</sup> Both samples displayed similar rheology and Angstrom-scale microstructure and were described by the Hershel and Buckley model with different yield stresses: 0.29 Pa for lamellar-40 and 4.1 Pa for lamellar-70. Yield stress is defined as the transition (critical or transient) from a solid-like to liquid-like state of deformation of a complex fluid.<sup>45</sup> However, accurately quantifying yield stress using a shear rheometer can be quite complex as contributions from different flow behaviors, including wall-slip and shear banding, can create artifacts impacting the measurement of this parameter.<sup>76</sup> Evidence of such artifacts are seen by directly comparing the flow curve and velocimetry data, displayed in Figure 3-13 and Figure 3-14.

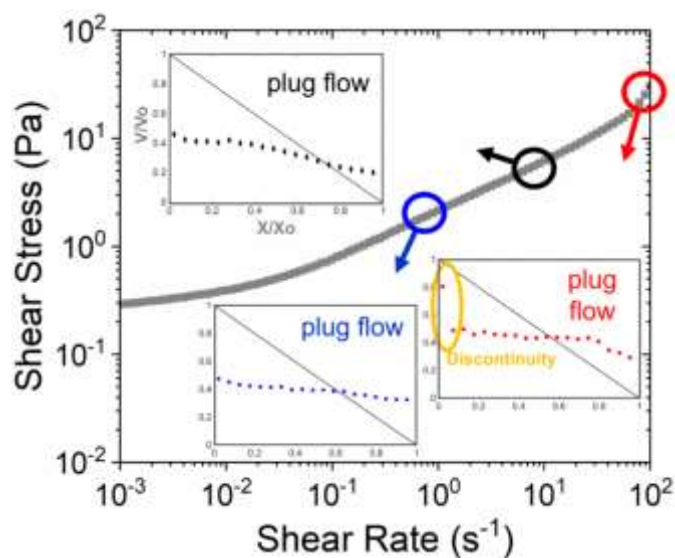


Figure 3-13 Lamellar-40 flow curve and flow velocimetry relationship. Flow curve data from Figure 3-4c and local velocity profiles at three shear rates from Figure 3-7d. Inset plots display the normalized velocity as a function of normalized gap

The lamellar-40 sample (Figure 3-13) exhibited plug flow at every applied shear rate ( $0.7 \text{ s}^{-1}$ ,  $7 \text{ s}^{-1}$  and  $70 \text{ s}^{-1}$ ). The highest shear rate resulted in the formation of a discontinuity near the moving wall and small shear band near the stationary wall ( $x / x_o > 0.8$ ). The lamellar-70 sample (Figure 3-14) displayed plug flow at low shear rates, the formation of a slight shear band near the moving wall ( $x / x_o < 0.2$ ) at intermediate shear rates, and evidence of a possible “recovery” of simple shear

behavior at high shear rates. Thus, due to the occurrence of plug flow and some areas of shear banding in the velocimetry data, the flow curve data for these lamellar samples should not be used to directly quantify a “true” (bulk) yield stress value, as such values seem to represent only the stress required to deform a relatively small volume of sample, *i.e.*, lubrication layers around the plug.

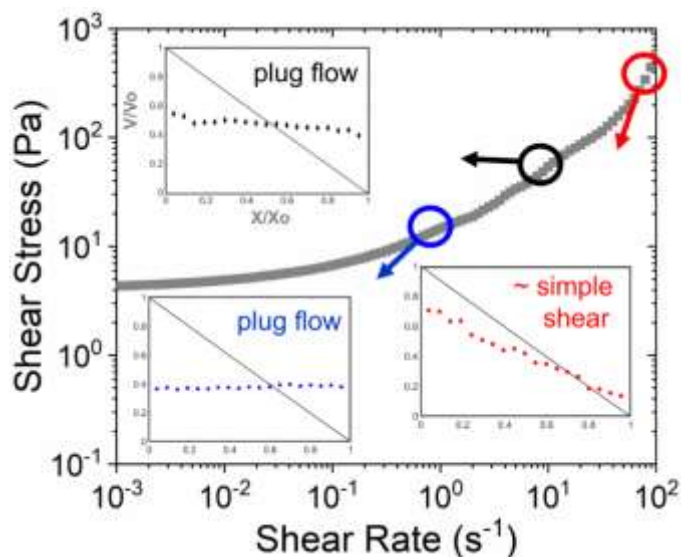


Figure 3-14 Lamellar-70 sample: flow curve and flow velocimetry relationship. Flow curve data from Figure 3-4c and local velocity profiles at three shear rates from Figure 3-7e. Inset plots display the normalized velocity as a function of normalized gap

The mechanics of plug flow within the lamellar samples is believed to be similar to the hexagonal sample in which lubrication layers are created by the rearrangement and flow of small, solid-like domains composed of hexagonally packed cylindrical micelles. For the lamellar samples, domains are most likely composed of sheets and oily streaks, which are not expected to be as elastic as the hexagonal domains. This most likely explains why deformation occurred at relatively lower values of stress for the lamellar samples compared with the hexagonal sample (see flow curve in Figure 3-4).<sup>77 78 79</sup>

To fully understand the flow behavior of the lamellar samples, it is also necessary to consider the shear history dependency of the lamellae in the microstructure. It is well known that a lamellar

phase under continuous and steady shear (flow or oscillatory) undergoes a series of microstructural rearrangements due to their nonequilibrium nature.<sup>80</sup> As shown in the flow birefringent images of Figure 3-9 for the lamellar-70 sample, the organization of oily streaks varied over a short period of time from random orientation at rest to highly oriented at high shear rates and this rearrangement appeared to be non-reversible. Thus, the oriented oily streaks most likely dominated the lamellar microstructure that existed during the flow curve and flow velocimetry measurements, which were conducted from high to low applied shear rates. Therefore, the differences in the measured flow behavior of the lamellar-70 and lamellar-40 samples were most likely dependent on the organization of oily streaks, as described below.

Comparing Figure 3-13 and Figure 3-14, the lamellar-40 sample displayed plug flow at the highest applied shear rate while the lamellar-70 sample displayed behavior approaching simple shear. This difference was most likely a function of the lamellar spacing in the two samples, a direct result of the differences in surfactant concentration (70 wt.% vs. 40 wt.%) and ionic strength (0% NaCl vs. 5% NaCl).<sup>11 81</sup> The lamellar spacing does not change with the formation of MLV; however, domains of MLV leads to the formation of continuous oily streaks which change the viscosity behavior of lamellar phase.<sup>80</sup> As shown in Figure 3-8, oily streaks were observed to be nearly adjacent in the lamellar-70 sample while the lamellar-40 sample contained streaks that were separated by ~ 50 microns. This increased spacing (reduced concentration) of oily streaks in the lamellar-40 sample most likely increased the likelihood of strain localization at high shear rates (manifest as lubrication layers and plug flow) while the concentrated structure of the lamellar-70 sample displayed a more uniform deformation response at high shear rates (manifest as simple shear).

### **3.5 Summary and Implications**

This study demonstrates a potential workflow to determine the processing-relevant relationships between the microstructure and flow behavior of concentrated surfactant solutions using a combination of basic rheological experiments, rheo-flow velocimetry tests, and flow birefringence measurements. A key objective was to evaluate the quality of information about a liquid surfactant that was obtained from a flow curve experiment performed in a shear rheometer. It was found that common features of flow curves (*e.g.*, power-law shear thinning behavior) can result from a wide

variety of material responses, including shear-induced wall-slip and plug flow, and rheo-physical experiments were required to correlate the local deformation behavior with its rheological signature.

The most dilute surfactant solution (20 wt.% SLE<sub>1</sub>S) formed disordered spherical micelles and displayed Newtonian, simple shear behavior. When salt was added to the solution, worm-like micelles formed and displayed wall-slip at shear rates corresponding to shear thinning behavior in the flow curve. When the surfactant concentration was increased to 40 wt.% SLE<sub>1</sub>S, the solution became a viscoelastic solid-like material with a microstructure of hexagonally packed cylindrical micelles. When shear deformation was applied, plug flow was observed at shear rates which corresponded to shear thinning in the flow curve, a response most likely generated by a lubrication layer of aligned cylinders surrounding the viscoelastic plug. Upon the addition of salt, the microstructure was transformed to a lamellar structure, which also displayed shear thinning plug flow at all investigated shear rates. At the highest surfactant concentration of this study (70 wt.% SLE<sub>1</sub>S), a lamellar microstructure was present and behaved similarly to the less concentrated lamellar sample except that at very high shear rates, the viscosity slightly increased and behavior approaching simple shear was observed.

Future work can expand from this study to include other formulation and processing-relevant parameters such as temperature and salt content. The timescales of microstructural reorganization during or following shear deformation could also be characterized in more detail to provide additional insight into some of the critical shear rates observed here in an effort to further define the relationships between processing, microstructure, flow properties, and performance.

In general, the shear-induced microstructures of concentrated surfactant solutions, which form the chemical base for many detergents and personal care products, can have very different rheological properties ranging from strongly thixotropic phases to phases that are shear thinning. When concentrated solutions are exposed to high shear forces, a variety of behaviors can occur, such as shear banding, fluid fracture, and wall-slip. While these are typically assumed to be bad for industrial processing (*e.g.*, resulting in material inhomogeneity), it is largely unknown if these behaviors could potentially enhance the manufacturing of concentrated materials, perhaps by

reducing the pressures needed to pump fluids through a pipe or by controllably mixing multi-phase components during pumping.

In light of the recent sustainability challenges to create more concentrated products, company resources are most often devoted to new capital manufacturing equipment, and few (if any) resources are devoted to developing a better understanding of the processing science related to more complex, concentrated raw materials and feedstocks. Until the fundamental scientific relationships between microstructure, properties, and large-scale processability and performance are better defined for concentrated complex fluids, industry will continue to sacrifice valuable resources to inefficient and unsustainable manufacturing processes.

### 3.6 References

1. Koehler A, Wildbolz C. Comparing the Environmental Footprints of Home-Care and Personal-Hygiene Products: The Relevance of Different Life-Cycle Phases. *Environ Sci Technol.* 2009;43(22):8643-8651. doi:10.1021/es901236f
2. Giagnorio M, Amelio A, Grüttner H, Tiraferri A. Environmental impacts of detergents and benefits of their recovery in the laundering industry. *J Clean Prod.* 2017;154:593-601. doi:10.1016/j.jclepro.2017.04.012
3. Anderson R. Companies get serious about water use - BBC News. BBC News. <https://www.bbc.com/news/business-35613148>. Published 2016. Accessed October 29, 2018.
4. Saouter E, Van Hoof G, Pittinger CA, Feijtel TCJ. The Effect of Compact Formulations on the Environmental Profile of Northern European Granular Laundry Detergents. *Int J Life Cycle Assess.* 2001;6(6):363-372. doi:10.1007/BF02978867
5. Butler P. Shear induced structures and transformations in complex fluids. *Curr Opin Colloid Interface Sci.* 1999;4(3):214-221. doi:10.1016/S1359-0294(99)00041-2
6. Roux D, Nallet F, Diat O. Rheology of Lyotropic Lamellar Phases. *Europhys Lett.* 1993;24(1):53-58. doi:10.1209/0295-5075/24/1/009
7. Rosevear FB. Liquid Crystals: The Mesomorphic Phases of Surfactant Compositions. *J Soc Cosmet Chem.* 1968;19(1):581-594.
8. Laughlin RG. *The Aqueous Phase Behavior of Surfactants*. Academic Press; 1994.

9. Ezrahi S, Tuval E, Aserin a. Properties, main applications and perspectives of worm micelles. *Adv Colloid Interface Sci.* 2006;128-130(2006):77-102. doi:10.1016/j.cis.2006.11.017
10. Berni MG, Lawrence CJ, Machin D. A review of the rheology of the lamellar phase in surfactant systems. *Adv Colloid Interface Sci.* 2002;98(2):217-243. doi:10.1016/S0001-8686(01)00094-X
11. Gentile L, Silva BFB, Lages S, Mortensen K, Kohlbrecher J, Olsson U. Rheochaos and flow instability phenomena in a nonionic lamellar phase. *Soft Matter.* 2013;9(4):1133-1140. doi:10.1039/c2sm27101j
12. Richtering W. Rheology and shear induced structures in surfactant solutions. *Curr Opin Colloid Interface Sci.* 2001;6(5-6):446-450. doi:10.1016/S1359-0294(01)00118-2
13. Kresta SM, Paul EL, Atiemo- Obeng VA, eds. *Handbook of Industrial Mixing.* John Wiley & Sons, Inc.; 2004. doi:10.1002/0471451452
14. Basappa G, Kumaran V, Nott P, Ramaswamy S, Naik V, Rout D. *Structure and Rheology of the Defect-Gel States of Pure and Particle-Dispersed Lyotropic Lamellar Phases.* Vol 12.; 1999.
15. Carreau PJ. *Rheometry of Pastes, Suspensions and Granular Materials. Applications in Industry and Environment.* Vol 46. Wiley; 2006. doi:10.1007/s00397-006-0118-y
16. Bird RB (Robert B, Stewart WE, Lightfoot EN. *Transport Phenomena.* 2nd ed. (Anderson W, ed.). New York: John Wiley & Sons, Inc.; 2007.
17. Wyss HM. Rheology of soft materials. *Fluids, Colloids Soft Mater An Introd to Soft Matter Phys.* 2018:149-164. doi:10.1002/9781119220510.ch9
18. Macosko CW. *Rheology: Principles, Measurements, and Applications.* Vol 41. Wiley-Blackwell; 1995. doi:10.1002/aic.690411025
19. Larson RG. Instabilities in viscoelastic flows. *Rheol Acta.* 1992;31(3):213-263. doi:10.1007/BF00366504
20. Fardin MA, Divoux T, Guedeau-Boudeville MA, et al. Shear-banding in surfactant wormlike micelles: elastic instabilities and wall slip. *Soft Matter.* 2012;8(8):2535. doi:10.1039/c2sm06992j

21. Christel M, Yahya R, Albert M, Abboud Antoine B. Stick-slip control of the Carbopol microgels on polymethyl methacrylate transparent smooth walls † *Soft Matter. Soft Matter*. 2012;8:7365. doi:10.1039/c2sm26244d
22. Malkin AY, Patlazhan SA. Historical perspective Wall slip for complex liquids- Phenomenon and its causes. *Adv Colloid Interface Sci*. 2018;257:42-57. doi:10.1016/j.cis.2018.05.008
23. Fardin MA, Ober TJ, Grenard V, et al. Interplay between elastic instabilities and shear-banding: three categories of Taylor-Couette flows and beyond †. *Soft Matter*. 2012;8:10072. doi:10.1039/c2sm26313k
24. Divoux T, Fardin MA, Manneville S, Lerouge S. Shear Banding of Complex Fluids. *Annu Rev Fluid Mech*. 2016;48:81-103. doi:10.1146/annurev-fluid-122414-034416
25. Sprakel J, Spruijt E, Stuart MAC, Besseling NAM, Lettinga MP, Van Der Gucht J. Shear banding and rheochaos in associative polymer networks. *Soft Matter*. 2008;4:1696-1705. doi:10.1039/b803085e
26. Ligoure C, Mora S. Fractures in complex fluids: The case of transient networks. *Rheol Acta*. 2013;52(2):91-114. doi:10.1007/s00397-012-0668-0
27. Divoux T, Barentin C, Manneville S. Stress overshoot in a simple yield stress fluid: An extensive study combining rheology and velocimetry. *Soft Matter*. 2011;7(19):9335-9349. doi:10.1039/c1sm05740e
28. Hutton JF. Fracture of Liquids in Shear. *Nature*. 1963;200(4907):646-648. doi:10.1038/203177a0
29. Hutton JF. Fracture and Secondary Flow of Elastic Liquids. *Rheol Acta*. 1969;8:54-59. doi:https://doi-org.ezproxy.lib.purdue.edu/10.1007/BF02321355
30. Archer LA, Ternet D, Larson RG, Archer LY, Ternet D, Larson RG. "Fracture" *Phenomena in Shearing Flow of Viscous Liquids*. Vol 36.; 1997.
31. Li Y, McKenna GB. Startup shear of a highly entangled polystyrene solution deep into the nonlinear viscoelastic regime. *Rheol Acta*. 2015;54(9-10):771-777. doi:10.1007/s00397-015-0876-5
32. Husband DM, Mondy LA, Ganani E, Graham AL. Direct measurements of shear-induced particle migration in suspensions of bimodal spheres. *Rheol Acta Rheol Acta*. 1994;33:185-192. doi:10.1007/BF00437303

33. Graham AL, Mammoli AA, Busch MB. Effects of demixing on suspension rheometry. *Rheol Acta*. 1998;37(2):139-150. doi:10.1007/s003970050100
34. Sui C, Mckenna GB. Instability of entangled polymers in cone and plate rheometry. 2007. doi:10.1007/s00397-007-0169-8
35. Veerman C, Sagis LMC, Venema P, et al. Shear-induced aggregation and break up of fibril clusters close to the percolation concentration. *Rheol Acta*. 2005;44:244-249. doi:10.1007/s00397-004-0403-6
36. Rehage H, Hoffmann H. Shear induced phase transitions in highly dilute aqueous detergents solutions. *Rheol Acta*. 1982;21:561-563. doi:10.1007/BF01534347
37. Erk KA, Martin JD, Hu YT, Shull KR. Extreme strain localization and sliding friction in physically associating polymer gels. *Langmuir*. 2012;28(9):4472-4478. doi:10.1021/la204592r
38. Berret J-F, Séréro Y, Winkelman B, Calvet D, Collet A, Viguier M. Nonlinear rheology of telechelic polymer networks. *J Rheol (N Y N Y)*. 2001;45(2):477-492. doi:10.1122/1.1339245
39. Berret J-F, Séréro Y. Evidence of Shear-Induced Fluid Fracture in Telechelic Polymer Networks. *Phys Rev Lett*. 2001;87(4):048303. doi:10.1103/PhysRevLett.87.048303
40. Takeda M, Kusano T, Matsunaga T, Endo H, Shibayama M, Shikata T. Rheo-SANS studies on shear-thickening/thinning in aqueous rodlike micellar solutions. *Langmuir*. 2011;27(5):1731-1738. doi:10.1021/la104647u
41. Kotula AP, Meyer MW, De Vito F, Plog J, Hight Walker AR, Migler KB. The rheo-Raman microscope: Simultaneous chemical, conformational, mechanical, and microstructural measures of soft materials. *Rev Sci Instrum*. 2016;87(10):105105. doi:10.1063/1.4963746
42. Kiewiet S, Janssens V, Miltner HE, Van Assche G, Van Puyvelde P, Van Mele B. RheoDSC: A hyphenated technique for the simultaneous measurement of calorimetric and rheological evolutions. *Rev Sci Instrum*. 2008;79(2):234904. doi:10.1063/1.2838585
43. Markus, Raffel. Wilert, Christian, Wereley, Steve. Kompenhans J. *Particle Image Velocimetry: A Practical Guide*. 2nd ed. New York: Springer Berlin Heidelberg; 2007. doi:10.1007/978-3-540-72308-0

44. Manneville S, Becu L, Colin A. High-frequency ultrasonic speckle velocimetry in sheared complex fluids. *Eur Phys J Appl Phys*. 2004;28(3):361-373. doi:10.1051/epjap:2004165
45. Divoux T, Barentin C, Manneville S. From stress-induced fluidization processes to Herschel-Bulkley behaviour in simple yield stress fluids. *Soft Matter*. 2011;7(18):8409. doi:10.1039/c1sm05607g
46. Herle V, Manneville S, Fischer P. Ultrasound velocimetry in a shear-thickening wormlike micellar solution: Evidence for the coexistence of radial and vorticity shear bands. *Eur Phys J E*. 2008;26(1-2):3-12. doi:10.1140/epje/i2007-10304-3
47. Holton DA, Jackson B, Saito A, Wormald NC. Rapid MRI and velocimetry of cylindrical couette flow. *Magn Reson Imaging*. 1990;14(4):465-473. doi:10.1002/jgt.3190140410
48. Poelma C. Ultrasound Imaging Velocimetry: a review. *Exp Fluids*. 2017;58(1):3. doi:10.1007/s00348-016-2283-9
49. Dimitriou CJ, Casanellas L, Ober TJ, McKinley GH. Rheo-PIV of a shear-banding wormlike micellar solution under large amplitude oscillatory shear. *Rheol Acta*. 2012;51(5):395-411. doi:10.1007/s00397-012-0619-9
50. Thornell TL, Subramaniam K, Erk KA. The impact of damage accumulation on the kinetics of network strength recovery for a physical polymer gel subjected to shear deformation. *J Polym Sci Part B Polym Phys*. 2016;54(17):1693-1701. doi:10.1002/polb.24071
51. Shapley NC, Armstrong RC, Brown RA. Laser Doppler velocimetry measurements of particle velocity fluctuations in a concentrated suspension. *J Rheol (N Y N Y)*. 2002;46(1):241-272. doi:10.1122/1.1427908
52. Manneville S, Colin A, Waton G, Schosseler F. Wall slip, shear banding, and instability in the flow of a triblock copolymer micellar solution. *Phys Rev E - Stat Nonlinear, Soft Matter Phys*. 2007;75(6):1-11. doi:10.1103/PhysRevE.75.061502
53. Feigin LA, Svergun DI. *Structure Analysis by Small-Angle X-Ray and Neutron Scattering*. (George W. Taylor, ed.). Princeton, NJ; 1987. doi:10.1007/978-1-4757-6624-0
54. Manaia EB, Abuçafy MP, Chiari-Andréo BG, Silva BL, Oshiro Junior JA, Chiavacci LA. Physicochemical characterization of drug nanocarriers. *Int J Nanomedicine*. 2017;12:4991-5011. doi:10.2147/IJN.S133832

55. Rosevear FB. The microscopy of the liquid crystalline neat and middle phases of soaps and sythetic detergents. *J Am oil Chem Soc.* 1954;31:628-639. doi:10.1007/BF02545595
56. Israelachvili JN. *Intermolecular and Surface Forces*. Academic Press; 2011.
57. Lerouge S, Berret J-F. Shear-induced transitions and instabilities in surfactant wormlike micelles. In: Dusek K, Joanny J, eds. *Polymer Characteriation*. Paris: Springer Berlin Heidelberg; 2009:71. doi:10.1007/12\_2009\_13
58. Aoudia M, Al-Haddabi B, Al-Harhi Z, Al-Rubkhi A. Sodium Lauryl Ether Sulfate Micellization and Water Solubility Enhancement Towards Naphthalene and Pyrene: Effect of the Degree of Ethoxylation. *J Surfactants Deterg.* 2010;13(1):103-111. doi:10.1007/s11743-009-1131-9
59. Caicedo-Casso E, Sargent J, Dorin RM, et al. A rheometry method to assess the evaporation-induced mechanical strength development of polymer solutions used for membrane applications. *J Appl Polym Sci.* August 2018:47038. doi:10.1002/app.47038
60. Larson RG. *The Structure and Rheology of Complex Fluids (Topics in Chemical Engineering)*. Oxford University Press; 1999.
61. Panton RL. *Incompressible Flow*. 4th ed. Hoboken, New Jersey: John Wiley & Sons, Inc.; 2013.
62. Cassagnau P. Linear viscoelasticity and dynamics of suspensions and molten polymers filled with nanoparticles of different aspect ratios. *Polym (United Kingdom)*. 2013;54(18):4762-4775. doi:10.1016/j.polymer.2013.06.012
63. Walker LM. Rheology and structure of worm-like micelles. *Curr Opin Colloid Interface Sci.* 2001;6(5-6):451-456. doi:10.1016/S1359-0294(01)00116-9
64. Berret J-F. Rheology of Wormlike Micelles : Equilibrium Properties and Shear Banding Transition. In: Terech P, Weiss RG, eds. *Molecular Gels*. Paris: Springer; 2006:667-720. <http://arxiv.org/abs/cond-mat/0406681>. Accessed October 6, 2018.
65. Mishra BK, Samant SD, Pradhan P, Mishra SB, Manohar C. *A New Strongly Flow Birefringent Surfactant System*. Vol 9.; 1993. <https://pubs.acs.org/sharingguidelines>. Accessed November 6, 2018.
66. Wunderlich I, Hoffmann H, Rehage H. Flow birefringence and rheological measurements on shear induced micellar structures. *Rheol Acta.* 1987;26(6):532-542. doi:10.1007/BF01333737

67. Makhloufi R, Decruppe JP, Aït-Ali A, Cressely R. Rheo-Optical Study of Worm-like Micelles Undergoing a Shear Banding Flow. *Europhys Lett.* 1995;32(3):253-258. doi:10.1209/0295-5075/32/3/011
68. Rogers SA, Calabrese MA, Wagner NJ. Rheology of branched wormlike micelles. *Curr Opin Colloid Interface Sci.* 2014;19:530-535. doi:10.1016/j.cocis.2014.10.006
69. Mohammadigoushki H, Muller SJ. A flow visualization and superposition rheology study of shear-banding wormlike micelle solutions. *Soft Matter.* 2016;12(4):1051-1061. doi:10.1039/c5sm02266e
70. Lettinga P, Manneville S. Competition between shear banding and wall slip in wormlike micelles. *Phys Rev Lett.* 2009;103(24):1-4. doi:https://doi.org/10.1103/PhysRevLett.103.248302
71. Montalvo G, Valiente M, Rodenas E. Rheological Properties of the L Phase and the Hexagonal, Lamellar, and Cubic Liquid Crystals of the CTAB/Benzyl Alcohol/Water System. *Langmuir.* 1996;12(21):5202-5208. doi:10.1021/la9515682
72. Sushko ML, Seddon JM, Templar RH. History-dependent rheology of a surfactant hexagonal phase. *Phys Rev E - Stat Nonlinear, Soft Matter Phys.* 2002;65(031501):1-10. doi:10.1103/PhysRevE.65.031501
73. Murray LR, Bice JE, Soltys EG, Perge C, Manneville S, Erk KA. Influence of adsorbed and nonadsorbed polymer additives on the viscosity of magnesium oxide suspensions. *J Appl Polym Sci.* 2018;135(3):45696. doi:10.1002/app.45696
74. Ahir S V, Petrov PG, Terentjev EM. Rheology at the Phase Transition Boundary: 2. Hexagonal Phase of Triton X100 Surfactant Solution. *Langmuir.* 2002;18:9140-9148. doi:10.1021/la025793c
75. Ahmed Siddig M, Radiman S, Jan L, Muniandy S. Rheological behaviours of the hexagonal and lamellar phases of glucopone (APG) surfactant. *Physicochem Eng Asp.* 2006;276:15-21. doi:10.1016/j.colsurfa.2005.10.004
76. Bonn D, Denn MM. Materials science. Yield stress fluids slowly yield to analysis. *Science.* 2009;324(5933):1401-1402. doi:10.1126/science.1174217

77. Briceño-Aumada Z, Soltero A, Maldonado A, Perez J, Langevin D, Impéror-Clerc M. On the use of shear rheology to formulate stable foams. Example of a lyotropic lamellar phase. *Colloids Surfaces A Physicochem Eng Asp.* 2016;507:110-117. doi:10.1016/j.colsurfa.2016.07.077
78. Panizza P, Colin A, Coulon C, Roux D. A dynamic study of onion phases under shear flow: Size changes. *Eur Phys J B.* 1998;4(1):65-74. doi:10.1007/s100510050352
79. Gentile L, Rossi CO, Olsson U. Rheological and rheo-SALS investigation of the multi-lamellar vesicle formation in the C 12 E 3 /D 2 O system. *J Colloid Interface Sci.* 2012;367:537-539. doi:10.1016/j.jcis.2011.10.057
80. Fritz G, Wagner NJ, Kaler EW. Formation of Multilamellar Vesicles by Oscillatory Shear. *Langmuir.* 2003;19:8709-8714. doi:10.1021/la0349370
81. Diat O, Roux D, Nallet F. “Layering” effect in sheared lyotropic lamellar phase. *Phys Rev E - Stat Nonlinear, Soft Matter Phys.* 1995;51(4):3296-3300.

## **4. SHEAR RHEOMETRY AS MEASURING TOOL OF THE POLYMER EROSION CONCENTRATION FOR POLYMER DISSOLUTION: THE CASE OF A SEMICRYSTALLINE WATER-SOLUBLE POLYMER**

### **4.1 Introduction**

Current tendencies in product development of the cleaning and beauty care industry are the inclusion of smart packaging technology to reduce the use of disposable packages in their products.

<sup>1</sup> One of the most common solutions is the integration of packages based on water-soluble polymers. These packages integrate physical characteristics that make them a viable choice for product transportation and product delivery for practical use. <sup>2</sup> The most rewarding point of this approach is the integration of economic savings, high consumer satisfaction, and environmental benefits.

Research and development of water-soluble polymers have been popular in the past decades. <sup>3</sup> A relevant topic has been the dynamics of polymer dissolution since these time-scales affect design production processes (e.g., polymer-solvent mixing for casting) and end use (e.g., detergent pouch dissolution). <sup>4</sup> During the past decades, polymer scientists have been developing theories, mathematical models, and measurement techniques to estimate polymer dissolution times scales. <sup>5</sup> Even though each study focuses on individual applications, the science behind these findings have common physics so approaches can be harmonized to advance for the needs of many industries. <sup>6</sup>

The dissolution of polymers is different than of small molecules. <sup>7</sup> <sup>6</sup> Dissolution of low molecular weight solutes start almost immediately after the solvent contacts the dry matrix. Different than small molecules, polymer dissolution does not happen instantaneously because polymer chains are long molecules with the ability to form physical entanglements (intricated 3D matrix) and detangling involves an additional timescale. Both processes are affected by solvent flow regimes, self-diffusion of solutes and the saturation concentration of the solute in the solvent, but only polymer dissolution introduces an extra factor to the equation: polymer viscoelasticity. <sup>8</sup>

Polymer dissolution occurs in a two-step process: swelling and erosion.<sup>9</sup> Swelling occurs when a penetrating solvent (at initial concentration  $C_s$ ) attacks the dry matrix (polymer specimen at initial concentration  $C_p$ ) creating an intermediate phase commonly called the gel layer (see Figure 4-1). The formation of the gel layer creates two interfaces that move in opposite directions. The matrix-gel interface (MG in Figure 4-1) is the point in space where the dry matrix (at  $C_p$ ) has its first contact with the solvent. This interface moves toward the center of the dry matrix ( $-\Delta x$ ). On the other hand, the gel-solvent interface (GS in Figure 4-1) moves far from the center of the matrix ( $+\Delta x$ ). This interface is the last point in space where the entanglements of polymer chains are still capable to hold a 3D matrix. In other words, polymer chains disengage at the gel-solvent interface once the critical polymer concentration ( $C_e$ ) is reached, enabling the erosion process.

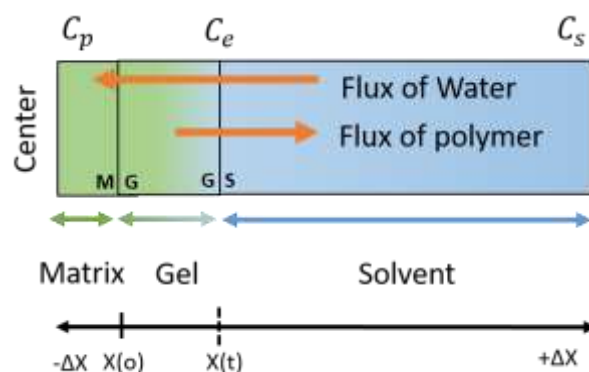


Figure 4-1. General dissolution framework of a dry polymer specimen that is being attacked by a penetrating solvent. General dissolution framework of a dry polymer specimen that is being attacked by a penetrating solvent.

The dynamics of the matrix-gel and the gel-solvent interface are time-dependent. The matrix-gel interface moves always to  $-\Delta x$  at a rate proportional to the penetrating solvent mass flow.<sup>10</sup> Conversely, the gel-solvent interface undergoes through three main stages after the initial exposure to the solvent.<sup>11</sup> First, the gel-solvent interface moves away from the center of the dry matrix ( $+\Delta x$ ). During the beginning of the exposure, the penetrating solvent mass flux dominates the dynamics of the gel-solvent interface since disengagement of polymer chains has not begun. After some time of exposure, the gel-solvent interface reaches a critical concentration ( $C_e$ ) and polymer chains begin to disengage. The initiation of polymer chain disengagement slowly initiates the second stage in which the effects of penetrating solvent mass flux are balanced with disengaging

polymer mass flux. These conditions keep the gel-solvent thickness at an equilibrium value. Lastly, the gel-solvent interface retreats backward ( $-\Delta x$ ) as the disengaging polymer mass flux overcomes the penetrating solvent mass flux effects; erosion of the gel layer begins. The duration and development of each stage depends on factors such as osmotic pressure, physicochemical properties of the polymer, polymer-solvent solubility, polymer viscoelasticity, and solvent characteristics.<sup>12</sup> An essential factor that dominates the dynamics of each stage is the solvent flow regimes. Pekcan et al. demonstrated that certain convection conditions could produce the erosion behavior of the polymer without the appearance of a gel layer.<sup>13</sup>

Scientists have developed different models to consider the dynamics of both interfaces.<sup>6</sup> However, the penetration of the solvent is considered a fast phenomenon compared to the events of polymer chain disengagement.<sup>8</sup> The limiting step in polymer dissolution occurs at the gel-solvent interface, and the disengagement occurring is influenced by the flow regimes of the solvent (outside the concentrated polymer) as well as the internal viscoelastic response within the dissolving polymer.<sup>12</sup> Consequently, phenomenological observations of a time-dependent gel-solvent interface are considered by the author of this document as the most relevant set of data to study dissolution of polymers.

Different approaches to polymer dissolution modeling are available. Phenomenological observations have used either Fickian equations or external mass transfer models that started by defining the time-dependent gel-solvent interface position.<sup>5</sup> The interface position is the result of a mass balance between the penetrating solvent mass flow (moving the interface to  $+\Delta x$ ) and disengaging polymer mass flux (moving the interface to  $-\Delta x$ ). Each final model presented a different degree of complexity by integrating parameters such as the properties of polymers (e.g., molecular mass, polydispersity, tacticity, glass transition temperature, crystallinity and relaxation time),<sup>14</sup> solvents (e.g., molecular interactions),<sup>15</sup> and environmental conditions (e.g., flow regimes and temperature)<sup>13</sup>. The set of assumptions considered during modeling included, but are not limited to: well-mixed solutions, incompressible fluids, constant polymer and solvent concentrations, constant diffusion coefficients and constant disengagement rates. All of the above are attempts to highlight key variables involved, simplifying a complex phenomenon as much as possible.

The techniques used to gather the experimental measures affect how data are used. These range from custom-made devices to advanced, high-end instrumentation and techniques. Some significant developments involve light scattering,<sup>16</sup> gravimetric,<sup>17</sup> refractometry,<sup>18</sup> microscopy,<sup>14</sup> laser interferometry,<sup>19</sup> ellipsometry,<sup>20</sup> fluorescence,<sup>21</sup> NMR<sup>22</sup> and FT-IR.<sup>23</sup> These techniques vary in accuracy; applications are influenced by instrument cost, the aim of the study, and individual preference.

In general, dissolution studies that require a deep understanding employ a combination of high-end techniques (microscale precision in space and time) coupled with a robust, well-developed mathematical model that includes complex physical, environmental and thermodynamic constants from the polymer-solvent system. Then, the application of such studies for academic purposes where obtaining absolute measurement is of high relevance is well justified. However, applying these approaches to industrial research is not cost-effective. For instance, evaluating the dissolution time of polymer solutions to drive business decisions requires results of dozens of samples in as many solvents, with results produced in days (not months). Also, the samples often contain several combinations of impure raw materials, solvent qualities, fabrication processes multiplying the number of parameters to deconvolute. The above introduces conditions that lead to endless repetitions of costly experiments making current high-end techniques a tedious, inappropriate work-flow.

Therefore, a simple and effective method to estimate the total dissolution time of polymers would be an essential solution for industrial research. This method should allow the study of multiple variables and its robustness would flex according to case specific demands. For instance, the development of soluble-shells for drug delivery in humans would need experiments with high accuracy of the time-dependent mass transfer properties. However, to develop water-soluble pouches used to deliver cleaning detergents, engineers would most likely need a single point in time (time until a film-breaks) which would be allowed to present a greater uncertainty compared to drug-delivery shells. This motivates the need for an accessible method that still captures the essential physics.

This chapter introduces the last protocol developed in this dissertation. The bulk of the chapter demonstrates the potential of a cost-effective, visualization technique to determine polymer dissolution times as a function of solvent shear rates. The relevant key in this chapter is the use of shear rheometry to determine the critical concentration when the polymer disentangles (at the gel-solvent interface) which is a necessary parameter for the calculation of mass transfer coefficients of the experimental observations. The critical concentration is determined by correlating the flow behavior of water-soluble polymer solutions to external solvent shear rates. Finally, a simple set of mass transfer experiments are shown to demonstrate a possible application describing the relationship of the developed work-flow with the rheological properties of a polymer matrix that is being dissolved by the action of a penetrating solvent.

## **4.2 Materials and Methods**

### **4.2.1 Materials**

Selvol™ E 205 is the water-soluble polymer selected to represent the experimental section of this study. Selvol™ E 205 is a commercial denomination of a partially hydrolyzed (87 to 89%) polyvinyl alcohol of approximate  $58.000 \text{ g}\cdot\text{mol}^{-1}$  molar mass produced by Sekisui Specialty Chemicals, LLC. Deionized (DI) water is the solvent used to prepare polymer solutions. Sample “S” was a mix of Selvol E 205 and DI water. Sample SPPG was the plasticized version of sample S. The plasticizer used in sample SPPG was propylene glycol at 15 wt.% Selvol replacement. All samples were prepared using dual-axis centrifugation at 3000 RPM for 10 min on sealed containers. Samples stabilized within days of sample preparation under constant environmental conditions (70 °C).

To perform the dissolution study using the stirrer-vial setup, samples S and SPPG at 44 wt.% polymer were used. Same samples at 0.1 wt.% to 50 wt.% polymer were used for rheological characterization.

The visualization of the gel-solvent interface during the stirrer-vial dissolution test was enhanced by incorporating Fluoresbrite™ carboxylate microspheres from Polysciences, Inc. into the solvent. The microspheres are monodispersed (1  $\mu\text{m}$  in diameter) and yellow-green fluorescent (excitation

wavelength of 441 nm and an emission wavelength of 486 nm). 8 drops of spheres solution are seeded to 0.3 kg of DI water ( $3 \times 10^{-5}$  % total DI water by mass). The primary goal of the microspheres is to create sharp change in refractive index between the solvent and the gel elucidating the gel-solvent boundary. It is assumed that the microspheres do not penetrate the concentrated entangled polymer gel during the measuring time.

Selvol™ E 205, Fluoresbrite™ carboxylate microspheres, deionized water, and other materials were donated by the Corporate Engineering Laboratories (CETL) from Procter and Gamble, West Chester, OH.

#### 4.2.2 The stirrer-vial dissolution test work-flow

A custom-made stirrer-vial set up as shown in Figure 4-2 was used to evaluate dissolution time as a function of solvent shear rate. A stirrer with a flat-surface tip (0.005 m width) and digitally-controlled RPM was coupled with a commercial clear glass 8-dram vial with 0.025 m in diameter and total volume of 30 cm<sup>3</sup>. In this apparatus, the diameter of the vial is approximately five times the diameter of the stirrer. A costume-made extension cup was added to the vial to accommodate an excess of solvent of 25 cm<sup>3</sup>. The illumination used to excite the fluorescent microspheres (seeded to the solvent) was black light from a LED DragonX UV light (54x3 Watts). A Canon EOS Rebel T5 camera with polarizer lens and EOS Rebel T5 software were used to acquire images at constant intervals of time between 30 s to 180 s.

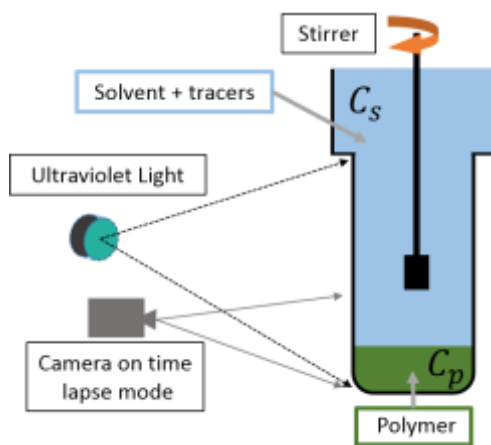


Figure 4-2. Vial-stirrer experimental set up used for dissolution experiments.

The preparation for the stirrer-vial dissolution test started with the sample preparation. A specimen (S or SPPG sample) of 1 g was added to the glass vial and then centrifuged at 2000 RPM for 10 min to assure a flattened disc shape at the bottom of the vial. The vial was sealed and left overnight in an oven at 60 °C for stabilization. Fluorescent microspheres were added to the deionized water right before the beginning of the test ( $3 \times 10^{-5}$  % solvent mass). 54 ml of solvent with seeded tracers were added to the vial-cup set-up. The acquisition of images started right after the addition of solvent to the vial. A total of four different solvent shear rate conditions were tested with one specimen per condition. Solvent shear rate conditions are represented by Reynolds number ( $R_e$ ) as shown in Equation 4-1.

Equation 4-1. Reynolds number ( $R_e$ ) for the stirrer-vial dissolution experiment;  $d$  is the stirrer diameter,  $N$  is the angular velocity and  $\mu_w$  is the kinematic viscosity of water.

$$R_e = \frac{d^2 N}{\mu_w}$$

### 4.2.3 Average solvent shear rate for the stirrer-vial set-up

The average solvent shear rate on the stirrer-vial set up was necessary to calculate the water-exerted stress ( $\tau_w$ ) on the surface of the polymer specimen. The average solvent shear rate was calculated using theoretical equations developed by Sanchez Perez et al.<sup>24</sup> First, the power number ( $N_p$ ) for the stirrer was calculated in an independent experiment by measuring the torque ( $M$ ) necessary to produce a given angular velocity ( $N$ ) and fitting the data to a  $M$  versus  $N^2$  relationship as presented in Equation 4-2.

Equation 4-2. Stirrer necessary torque to produce certain angular velocity.  $M$  is torque in N.m,  $d$  is stirrer diameter,  $\rho_w$  is water density,  $N$  is the stirrer angular velocity ( $\text{rad.s}^{-1}$ ).

$$M = \frac{N_p d^5 \rho_w}{2\pi} N^2$$

The independent experiment yield to a power number ( $N_p$ ) of 2.49. The power number is used in Equation 4-3 to calculate the average solvent shear rate as a function of angular velocity.

Equation 4-3. The average solvent shear rate of the stirrer-vial system.  $\dot{\gamma}_w$  is the average solvent shear rate and  $\eta_w$  is the dynamic viscosity of the water.

$$\dot{\gamma}_w = \left( \frac{4N_p d^2 \rho_w}{9\pi\eta_w} \right) N^{\frac{3}{2}}$$

Finally, water-exerted stress ( $\tau_w$ ) on the surface of the polymer can be calculated using Equation 4-4. The water-exerted stress for each applied Reynolds Number are presented in Table 4-1.

Equation 4-4. Water-exerted stress on the surface of the polymer specimen in the stirrer-vial test.  $\eta_w$  is the solvent dynamic viscosity.

$$\tau_w = \eta_w \dot{\gamma}_w$$

Table 4-1. Physical constants for the stirrer-vial dissolution test.

Reynolds Number $R_e$	Average water shear rate $\dot{\gamma}_w$ ( $s^{-1}$ )	Water-exerted stress $\tau_w$ (Pa)
3665	3043	3.04
2618	1837	1.84
1571	854	0.85
524	164	0.16

#### 4.2.4 Calculation of velocity of diffusion for the stirrer-vial dissolution test

Visualizing the gel-solvent interface over time (stirrer-vial dissolution test) is the key to compute the velocity of diffusion of polymer to solvent. Image sequences were created to track the change in position of the gel-solvent interface ( $\Delta x$ ). Five different points along the gel-solvent boundary were measured using ImageJ. The change in position of the gel-solvent interface ( $\Delta x$ ) was plotted and fitted against experimental time to determine their dependency.

The goal of the current chapter is to demonstrate the potential of a work-flow development using a custom-made experimental set-up. The parameters of diffusion were calculated using two simple mass flux equations that described the gel-solvent interface position over time. The equations derived for the gel-solvent interface consider a variable mass instead of variable concentration as the initial concentration of the specimen ( $C_p$ ) and the erosion concentration ( $C_e$ ) at the gel-solvent

interface are considered constant for the duration of the experiment. Other assumptions include fluid and polymer incompressibility, a constant area of diffusion ( $A$ ), constant polymer density ( $\rho_p=1 \text{ g.cm}^{-3}$ ), constant solvent concentration ( $C_s$ ), and constant shear conditions ( $\tau_w$ ), and constant diffusivity for the complete duration of the experiment.

For applied Reynold numbers where swelling of the matrix was observed ( $\Delta x > 0$ ), the position of the gel-solvent interface ( $\Delta x$ ) was a function of the square root of time as shown in Equation 4-5.  $\Delta x$  in Equation 4-5 represents the intake of a solvent that is penetrating a semi-infinite specimen under unsteady diffusion. Thus,  $\sqrt{\frac{D}{\pi t}}$  represents the time-dependent velocity of diffusion of the solvent penetrating the matrix.

Equation 4-5. Gel-solvent interface position as a function of time for  $\Delta x > 0$  (solvent intake conditions).  $A$  is the area of diffusion,  $m_w$  is the mass of solvent,  $D$  is the penetrating solvent diffusion coefficient,  $C_{we}$  is the erosion concentration in solvent terms,  $\rho_w$  solvent density and  $t$  is the experimental time.

$$\frac{1}{A} \frac{dm_w}{dt} = \sqrt{\frac{D}{\pi t}} (C_{we} - C_{wp}), \quad \text{if } m_w = x * A * \rho_w \xrightarrow[\text{yields}]{\text{integrating,}} \Delta x = 2 \sqrt{\frac{D}{\pi}} (C_{we} - C_{wp}) \sqrt{t}$$

Conversely, for applied Reynolds numbers where erosion of the matrix was observed ( $\Delta x < 0$ ), the gel-solvent interface position ( $\Delta x$ ) was correlated to linear time using Equation 4-6. Equation 4-6 represents the polymer delivered to the solvent as a function of time. The velocity of diffusion ( $K_{eP}$ ) is a constant lumped parameter that considers diffusive and convective terms.

Equation 4-6. Gel-solvent interface position as a function of time for  $\Delta x < 0$  (polymer erosion conditions).  $m_p$  is mass of polymer and  $K_{eP}$  is the lumped mass transfer coefficient dependent of Reynolds number.

$$\frac{1}{A} \frac{dm_p}{dt} = K_{eP} (C_e - C_s), \quad \text{if } m_p = x * A * \rho_p, C_s = 0 \xrightarrow{\text{yields}} -\Delta x = K_{eP} C_e t$$

#### 4.2.5 Film dissolution test work-flow

The total dissolution time of polymer films in a stagnant solvent was measured to create a set of data with different dissolution conditions. This data served to compare the results of the work-flow from the stirrer-vial dissolution test. Figure 4-3 presents the experimental set-up of the film. The specimen is a thin film of variable thickness ( $>90$  wt.% polymer,  $75\text{-}180\mu\text{m}$ ) sandwiched in a standard projector slide that secures a constant area of exposure ( $7.43\text{ cm}^2 \times 2$  is the total area). The solvent is deionized water at room temperature contained in a cubic bath ( $300\text{ cm}^3$ ). The visualization equipment is the same used during the stirrer-vial test, but the light source was a LED white backlight. There are not tracers in the solvent in the film dissolution test. Instead, a grid of markers is printed on the surface of each film to make possible the visualization of the film over time.

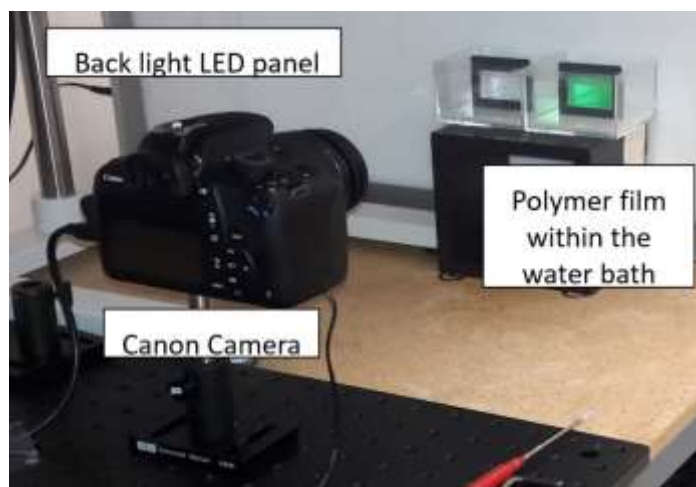


Figure 4-3. Film dissolution test set-up. The total dissolution time was the time that takes the printed grid to disappear. This set-up was used under permission of the Corporate Engineering Technical Laboratories, P&G. West Chester, Ohio.

The preparation for the test started with the film casting. Polymer films were cast using blade or pour casting techniques. The polymer solution used was 20 wt. % polymer. The film was dried at room temperature until it reached concentrations greater than 90 wt. % polymer. Grid printing and cutting to shape were the final adjustments before placing in the chamber.

The total film dissolution time was measured at the point in time in which the grid of markers disappeared from the analyzed area. Figure 4-4 shows a representation of the image sequence time for the film dissolution test. The projector slide was held perpendicular to the surface by a custom-made plate. The addition of solvent marked the beginning of the experiment. Pictures were taken with a constant interval of time between 5 s to 10 s.

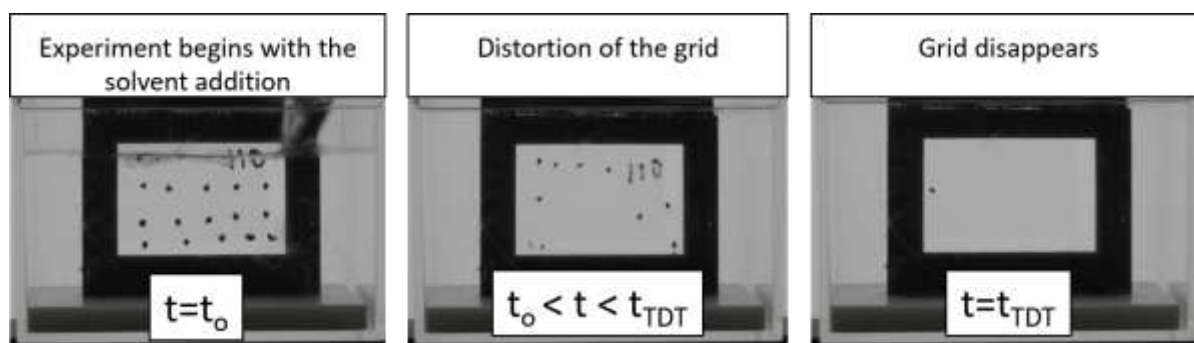


Figure 4-4. Image sequence of the dissolution film test. The addition of solvent begins the test ( $t_0$ ). The disappearance of the grid marks the end of the test; this is the total dissolution time (TDT).

#### 4.2.6 The diffusion coefficient of a Selvol E 205 chain in water

An independent dynamic light scattering (DLS) experiment on sample S at 1 wt.% and 2 wt.% polymer concentration was used to calculate the diffusion coefficient ( $D_{Chain}$ ) of a Selvol E 205 coil in water. The approximated hydration diameter ( $d_h$ ) was approximate 15.65 nm. The diffusion coefficient ( $D_{Chain}$ ) was calculated using a correction to the Stokes-Einstein equation presented in Equation 4-7.  $D_{Chain}$  was equal to  $2.76 \times 10^{-7} \text{ cm}^2\text{s}^{-1}$  and it used during the calculation of Sherwood numbers in the analysis section.

Equation 4-7. Correction to the Stokes-Einstein equation to calculate the diffusion coefficient for a random coil in a dilute stage.  $K_B T$  is the thermal energy at 295 K,  $\eta$  solvent viscosity and  $D_h$  is the coil hydration diameter.<sup>25</sup>

$$D_{Chain} = \left( \frac{K_B T}{3\pi\eta d_h} \right)$$

#### 4.2.7 The link with shear rheology in the determination of $C_e$

Equation 4-5 and Equation 4-6 needed a polymer erosion concentration ( $C_e$ ).  $C_e$  represents a polymer concentration at which the polymer chains (or bulk) disengage from the surface of the gel caused by solvent erosion. The stirrer-vial dissolution tests consider solvent shear rate as the main variable to study polymer dissolution. High solvent shear rates create forced convection conditions that erode faster than low shear rates. Consequently, the expected  $C_e$  at the gel surface is a function of the solvent shear rate.

The calculation of the polymer erosion concentration ( $C_e$ ) as a function of solvent shear rate is done using oscillatory shear rheometry. The erosion of the gel is possible if the water-exerted stress exceeds the stress for viscous deformation of the gel. Then,  $C_e$  as a function of shear rate can be calculated by creating a master plot of required stress for viscous deformation as a function of polymer concentration. Such calculations can be done using oscillatory shear rheometry and the concept of the linear viscoelastic range (LVR). The LVR represents the end of the elastic deformation behavior of a viscoelastic material and the beginning of irreversible or viscous deformation. Consequently, the stress needed to reach the LVR limit is analogous to the water-exerted stress.

A TA ARG2 rheometer equipped with 40 mm parallel plates was used to measure the storage ( $G'$ ) and loss modulus ( $G''$ ) at increasing oscillatory strain and constant frequency ( $10 \text{ rad}\cdot\text{s}^{-1}$ ). Parallel plates are coated with sandpaper (80 grit  $\approx 232 \mu\text{m}$ ) to reduce slippage and the gap used was 1 mm. Samples S and SPPG at 20 wt.%, 30 wt.%, 40wt.% and 50wt.% polymer were tested. Visual determination of the LVR in every sample was done by evaluating the deviation out of the linearity of  $G'$ . Then, the oscillation stress (for each LVR strain) is replotted as a function of polymer concentration to create the master curve. Finally, every tested water-exerted stress ( $\tau_w$ ) is evaluated in the master curve to calculate their respective  $C_e$ .

Rheological characterization of Selvol solutions was completed using rotational rheometry on samples S and SPPG. An Anton Paar MCR702 rheometer couple with a 27 mm cylindrical double gap geometry (used for 1 wt.% and 10 wt.% polymer concentration) and a 10 mm Couette geometry (used for 50wt.% polymer concentration) was used. The volume of the sample was 8 mL

for the double gap and 1.2 mL for the Couette geometry. Three logarithmic ramps were used to construct the flow profile: From  $0.001 \text{ s}^{-1}$  to  $0.1 \text{ s}^{-1}$  with an average time of 60 s/point, from  $0.1 \text{ s}^{-1}$  to  $1 \text{ s}^{-1}$  with an average time of 30 s/point and from  $1 \text{ s}^{-1}$  to  $1000 \text{ s}^{-1}$  with an average time of 7 s/point.

## 4.3 Results

### 4.3.1 Flow characterization

Figure 4-5 presents the shear stress response as a function of shear rate of samples S and SPPG. Curves in Figure 4-5 were not mathematically fitted because the steady flow was not the focus of this document. However, a visual interpretation is enough to provide insightful information. The Bingham model [ $\tau = \tau_y + \eta\dot{\gamma}$ ] can be used to describes samples S and SPPG at 10 wt.% and 50 wt.%.  $\tau$  is the shear stress,  $\tau_y$  is the apparent yield stress,  $\eta$  is the dynamic viscosity and  $\dot{\gamma}$  is the shear rate. The dynamic viscosity ( $\eta$ ) is constant for samples at 10 wt.% at all shear rates, but it is shear rate dependent for samples at 50 wt.%. On the other hand, the flow behavior at low concentration (1wt.% polymer) is better captured by a Hershel-Bulkley model [ $\tau = \tau_y + k\dot{\gamma}^n$ ] as the stress behavior showed a power law dependency to shear rate;  $k$  Is the consistency index and  $n$  is the power index.

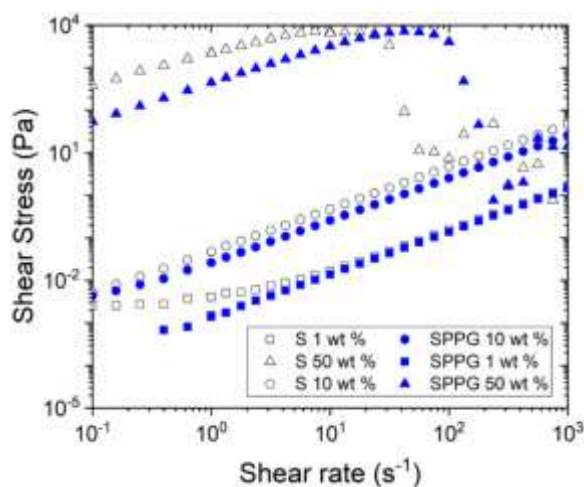


Figure 4-5. Flow curve for sample S and SPPG at 1 wt.%, 10 wt.% and 50wt.%. Empty symbols in black are data sets of sample S. Filled symbols in blue are data sets of sample SPPG.

### 4.3.2 $C_e$ determination

The calculation of  $C_e$  as a function of solvent shear rate started with the use of oscillatory amplitude sweep test. Figure 4-6 shows the general trend of the amplitude sweeps ( $G'$  and  $G''$  modulus as a function of oscillation strain) for S and SPPG samples at 20 wt.% and 50 wt.% polymer. Both samples behaved as a viscoelastic fluid ( $G'' > G'$ ) at the tested concentrations with sample S reporting the greater modulus.

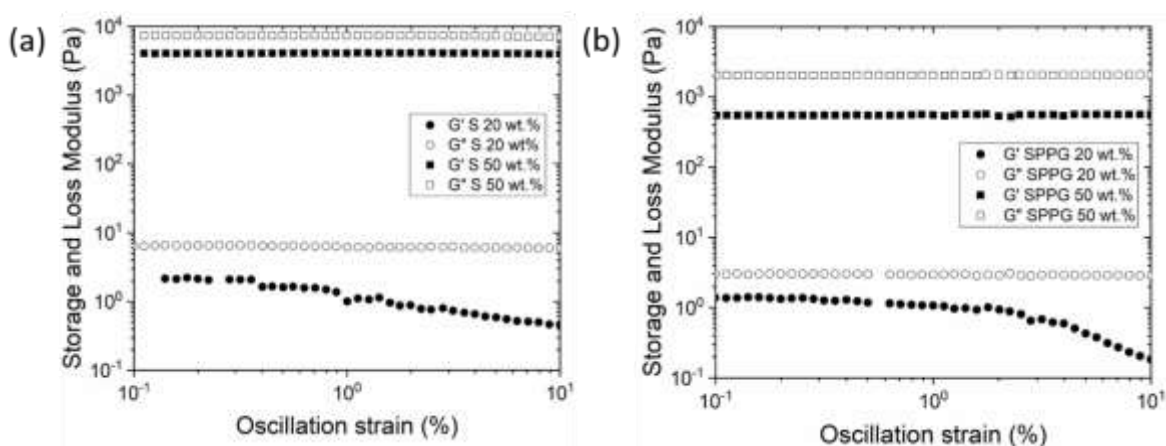


Figure 4-6.  $G'$  and  $G''$  general behavior of samples and SPPG.  $G'' > G'$  indicating a viscoelastic liquid behavior. (a) Sample S at 20 wt.% and 50 wt.% (b) Sample SPPG at 20 wt.% and 50 wt.%.

$G' - G''$  as a function of strain in the log to log scale did not allow a direct determination of the LVR. Replotting the  $G'$  data in individual linear-to-log plots was necessary to visually find the clear 5% off-set in deviation of linearity of  $G'$  data. Figure 4-7 shows the results for the oscillatory amplitude sweep on 20 wt.%, 30 wt.%, 40 wt.% and 50 wt.% polymer for samples S and SPPG.

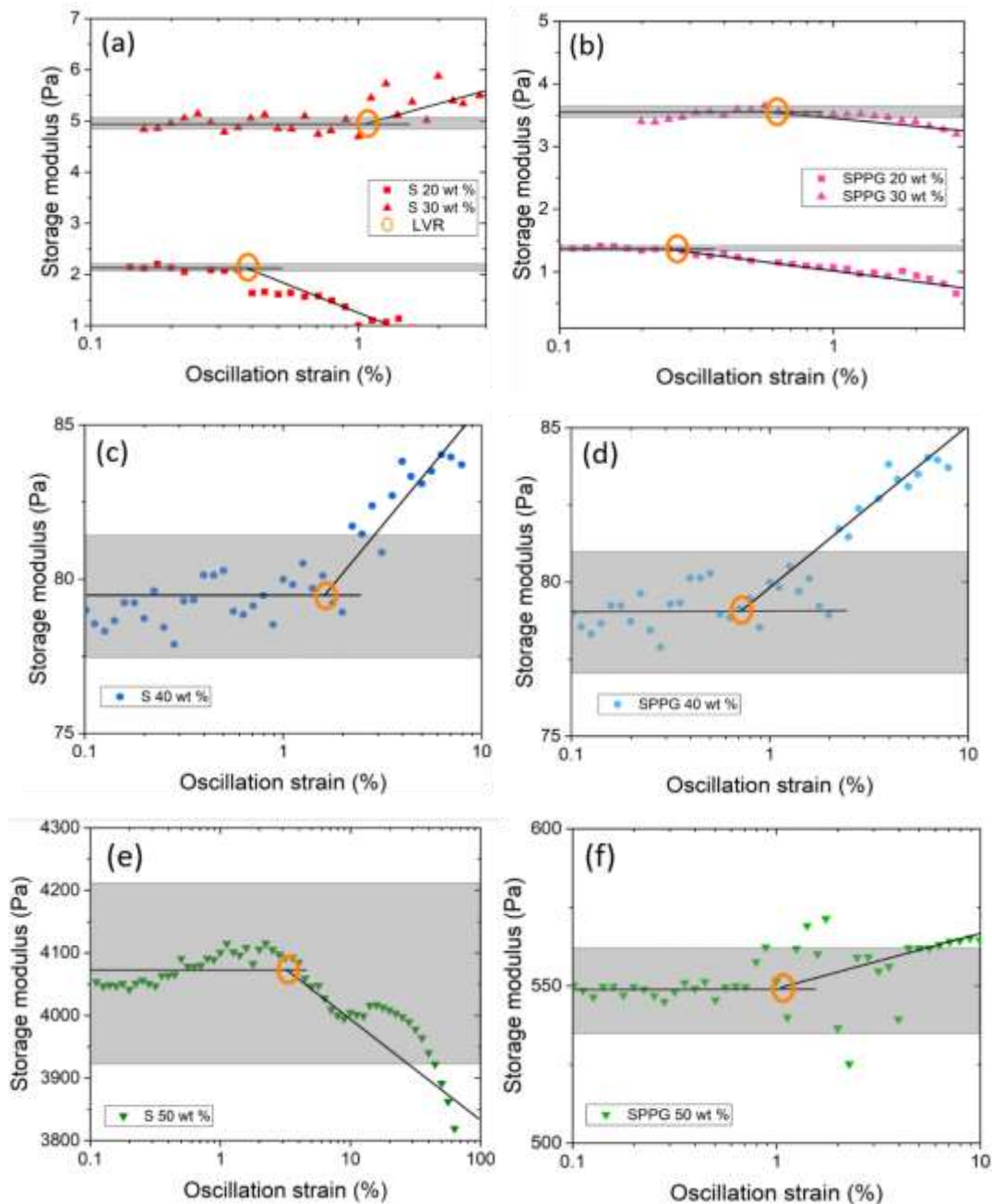


Figure 4-7.  $G'$  data as a function of oscillation strain on a linear-log scale. (a) sample S 20 wt.% and 30 wt.% polymer (b) sample SPPG 20 wt.% and 30 wt.% polymer (c) sample S 40 wt.% polymer (d) sample SPPG 40 wt.% polymer (e) sample S 50 wt.% polymer (f) sample  $G'$  data as a function of oscillation strain on a linear-log scale. (a) sample S 20 wt.% and 30 wt.% polymer (b) sample SPPG 20 wt.% and 30 wt.% polymer (c) sample S 40 wt.% polymer (d) sample SPPG 40 wt.% polymer (e) sample S 50 wt.% polymer (f) sample SPPG 50 wt.% polymer. The crossover point between two solid lines represents the intersection of the initial  $G'$  plateau and the out-of-linearity  $G'$  (greater than 5%) elucidate the LVR (orange circle). The shaded area corresponds to a  $\pm 2.5\%$  initial  $G'$  plateau.

Table 4-2 summarizes the LVR values (oscillation strain %) and their respective oscillation stress. In general, higher LVR resulted from specimens at higher polymer concentration. Also, sample S showed a higher LVR than sample SPPG at every polymer concentration.

Table 4-2. Oscillation stress for the linear viscoelastic range. LVR for samples S and SPPG as a function of polymer concentration. Oscillation strain and stress values were obtained from a visual analysis on Figure 4-7.

Polymer Concentration wt. %	LVR oscillation strain %		LVR oscillation stress Pa	
	S	SPPG	S	SPPG
20	0.39	0.24	0.024	0.0076
30	1.06	0.55	0.76	0.18
40	1.58	0.71	9.74	2.01
50	3.17	1.03	269.6	21.53

The data in Table 4-2 can be replotted in Figure 4-8 as a master curve to calculate  $C_e$  as a function of solvent shear rate. Figure 4-8 shows the oscillation stress to produce viscous deformation as a function of polymer concentration.  $C_e$  can be determined by evaluating every water-exerted shear stress from the stirrer-vial dissolution test (corresponding to an applied  $R_e$ ) then reading the respective polymer concentration for such stress. All  $C_e$  are summarized in Table 4-3.

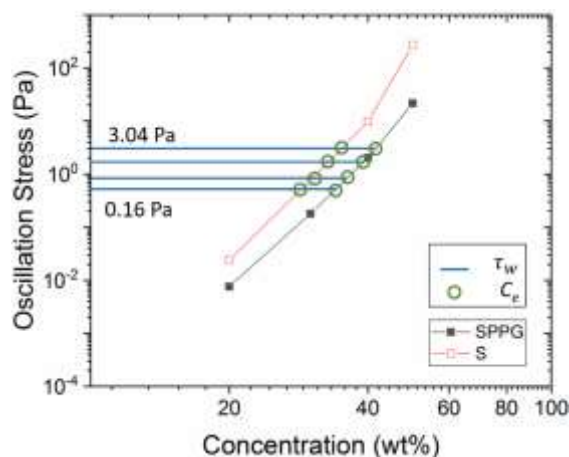


Figure 4-8.  $C_e$  master curve: oscillation stress necessary for viscous deformation as a function of polymer concentration. Red and black curves are the experimental data of sample S and SPPG respectively. The blue lines are the evaluated water-exerted stresses. The green circles are the respective  $C_e$ .

Table 4-3.  $C_e$  as a function of solvent Reynolds number in the stirrer-vial dissolution test.

Water-exerted stress $\tau_w$ (Pa)	Reynolds Number $Re$	Erosion Concentration $C_e$ (wt. %)	
		S	SPPG
3.04	3665	35	42
1.84	2618	33	40
0.85	1571	30	36
0.16	524	25	30

### 4.3.3 The velocity of diffusion in the stirrer-vial dissolution test

Figure 4-9 presents the results from the stirrer-vial dissolution test. Figure 4-9 presents the gel-solvent interface position over time ( $\Delta x_{(t)} = x_t - x_0$ ) as a function of Reynolds number. Five measurements along the gel-solvent interface were used to average individual experimental points ( $\Delta x$ ) at 0 min, 10 min, 60 min, 120 min, and 180 min respectively.

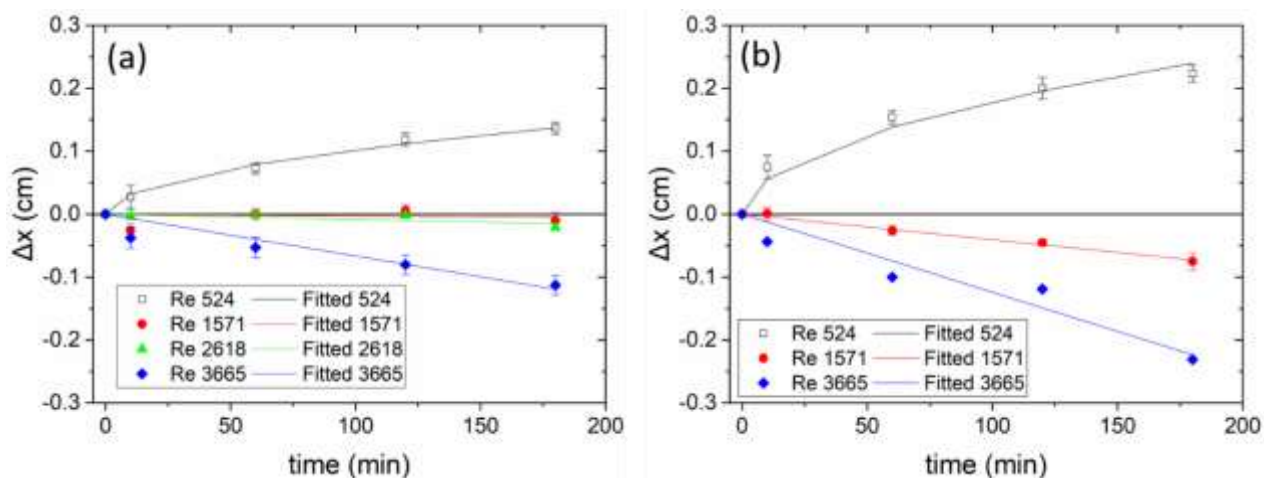


Figure 4-9. Gel-solvent interface position over time as a function of applied Reynolds number.

(a) sample S and (b) Sample SPPG. Colored dots represent the experimental data while solid lines represent the expected modeled behavior based on Equations 5 and 6. Positive  $\Delta x$  indicates swelling of the specimen, while negative  $\Delta x$  indicates erosion.

The position of the gel-solvent interface over time exhibited two general behaviors that were dependent on the applied Reynolds number. Low Reynolds numbers induced changes in position towards positive deltas ( $+\Delta x$ ) while high Reynolds numbers induced a retreating interface, negative deltas ( $-\Delta x$ ). The specimens from samples S and SPPG displayed a swelling behavior

( $+\Delta x$ ) at Reynolds number of 524. Experimental points at 524  $R_e$  were fitted to Equation 4-5. The experimental data showed a square root of time dependency and reported diffusion coefficients of  $3.8\text{E-}5 \text{ cm}^2.\text{s}^{-1}$  for S sample and  $2.1\text{E-}4 \text{ cm}^2.\text{s}^{-1}$  for sample SPPG. Sample SPPG reported a  $\Delta x$  of 0.22 cm (highest) while sample S reported 0.14 cm at 180 min.

Negative changes in position ( $-\Delta x$ ) reflecting the erosion of samples S and SPPG, occurred at Reynold number of 1571, 2618 and 3665. The experimental data showed a linear dependency with time fitting Equation 4-6. The calculated mass transfer coefficients for sample S were  $1.5\text{E-}6 \text{ cm}.\text{s}^{-1}$ ,  $4.2\text{E-}6 \text{ cm}.\text{s}^{-1}$ , and  $3.2\text{E-}5 \text{ cm}.\text{s}^{-1}$  for 1571, 2618 and 3665  $R_e$  respectively. For Sample SPPG, the calculated mass transfer coefficients were  $1.9\text{E-}5 \text{ cm}.\text{s}^{-1}$  and  $4.9\text{E-}5 \text{ cm}.\text{s}^{-1}$  for 1571 and 3665  $R_e$  respectively. It is important to highlight that sample SPPG showed the highest mass transfer coefficients for a given Reynolds number.

#### **4.3.4 The velocity of diffusion in the film dissolution test**

Four different specimens of sample S (75, 110, 150 and 180  $\mu\text{m}$  in thickness) were tested using the film dissolution test. The total dissolution time of each film was measured at the instance in which the grid printed on the surface of the film completely disappeared from the image.

Theoretical dissolution time for films was calculated using Equation 4-6 previously developed for the experimental data gathered from the stirrer-vial dissolution test. The parameters used were the mass of the film, the exposed area of the film and the greatest mass transfer coefficient of the stirrer-vial experiment ( $3.2 \times 10^{-5} \text{ cm}.\text{s}^{-1}$ ) and respective  $C_e$  (0.35 wt.%). Table 4-4 summarize the experimental and calculated results.

Table 4-4. Dissolution time as a function of film thickness for the film dissolution test. Experimental and calculated (from Equation 4-6) dissolution times for films.

Film Thickness ( $\mu\text{m}$ )	Experimental time of the film dissolution test (s)	Calculated dissolution time from Equation 4-6 (s)
75	95	337
110	140	491
150	320	660
180	995	781

Nevertheless, the variation between the experimental and calculated dissolution time in Table 4-4 is dependent on film thickness. They trend similarly but do differ. An attempt to create a correlation between these factors is made by calculating the ratio of experimental to calculated dissolution time. Figure 4-10 shows the ratio as a function of film thickness. Figure 4-10. Shows the existence of a critical film thickness in which the ratio between experimental to calculated dissolution time is constant.

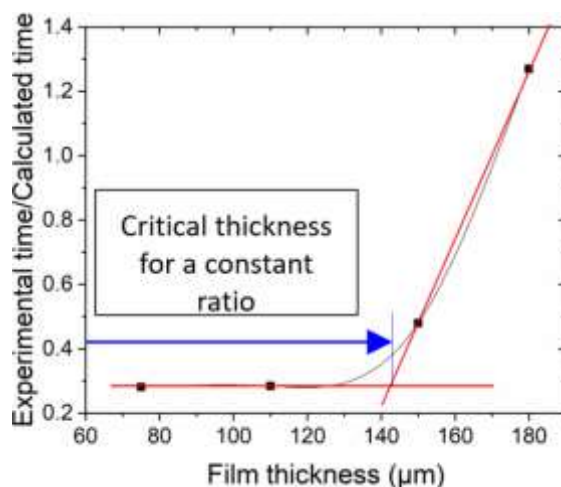


Figure 4-10. Experimental and calculated dissolution time ratio of films as a function of the film thickness. The black squares represent experimental data. Red solid lines are linear fittings to define the onset of film thickness.

#### 4.4 Discussion

As mentioned in the introduction of this chapter, this study intended to show the potential of a proposed cost-effective visualization technique to calculate relative polymer dissolution time as a function of solvent shear rate. The proposed protocol applied established science of polymer

dissolution on practical visualization experiments coupled with shear rheometry. One key step is the integration of oscillatory shear rheometry as an experimental tool to study the viscoelastic response of samples S and SPPG and thus determine the polymer concentration required for the erosion of the specimen ( $C_e$ ).

#### 4.4.1 Viscoelastic response of samples S and SPPG and $C_e$ determination

The first step towards the creation of the polymer dissolution protocol involved the determination of the polymer erosion concentration ( $C_e$ ).  $C_e$  is the polymer concentration needed for erosion to occur at a given water-exerted stress.<sup>16</sup> Erosion, seen as disengagement of polymer chains due to irreversible deformation, is only possible if the water-exerted stress is superior to the polymer stress needed for viscous deformation.<sup>26</sup> Hence,  $C_e$  is a property dependent on the viscoelastic response of each polymer sample and applied solvent shear rate.

As shear stress is responsible for polymer erosion in the stirrer-vial test, shear rheometry was proposed as an adequate tool to determine  $C_e$ . First, steady flow experiments and concepts such yield stress were considered to perform this calculation. Valois et al., used shear steady flow experiments to determine a critical concentration for the erosion of a polysaccharide of  $5 \times 10^6$  g.mol<sup>-1</sup>.<sup>16</sup> They used the onset shear rate for shear thinning behavior as an indicative of viscous deformation in their high molecular mass polymers. The onset data was transformed into critical stresses which led to the creation of a master plot of viscous deformation stress as a function of polymer concentration. Yet, the application of such protocol using samples S and SPPG was not possible as they did not show a clear shear thinning onsets during steady flow experiments (see Figure 4-5). Instead, they showed a constant viscosity behavior. This behavior has also been observed in other polyvinyl alcohol (PVA) solutions of low molecular mass.<sup>27 28</sup> The constant viscosity in sample S and SPPG can be partially explained by the entanglement density. Selvol E 205 is a low molecular mass polymer ( $58 \times 10^3$  g.mol<sup>-1</sup>) with low entanglement density compared to the high molecular mass polysaccharide used by Valois et al., 2016 ( $5 \times 10^6$  g.mol<sup>-1</sup>). Another reason to avoid the application of Valois et al., 2016 protocol was that flow behavior of sample S and SPPG at 50 wt.% (shown in Figure 4-5) depicted evidences of possible flow instabilities as shear stress suddenly dropped several orders of magnitude in a short range of shear rates. In this case, the observed stress response does not represent a material property, but it is product of an

artifact of the experiment. This behavior has been observed in similar polymer systems, and it can be attributed to the shear induced formation of shear bands of different viscosities.<sup>29</sup>

Since the rotational rheometry was insufficient to calculate  $C_e$ , the viscoelastic response of samples S and SPPG was evaluated using oscillatory shear rheometry. The behavior of storage modulus ( $G'$ ) and loss modulus ( $G''$ ) during the amplitude sweep test for specimens at 20 wt.% and 50 wt.% polymer (see Figure 4-6) suggested a general viscoelastic liquid behavior ( $G'' > G'$ ) for both samples. This behavior can be explained by the fact that samples S and SPPG are polymer solutions of polyvinyl alcohol (PVA) (highly soluble in polar solvents) with high contents of water.<sup>30</sup> Once water penetrates a solid specimen of PVA, water works as a plasticizing element reducing the elastic component ( $G'$ ) contribution in the total complex shear modulus ( $G^* = G' + iG''$ ) of PVA.<sup>31</sup> Mainly, water molecules have two ways of action to reduce the  $G'$  effect. First, water molecules can accumulate in between polymer chains (reducing hydrophobic interactions) allowing them to pass each other easily, thus reducing the effectiveness of chain entanglements.<sup>32</sup> Second, water molecules can attach physically to the hydroxyl side groups of PVA reducing the chance for physical cross-links (inter- and intra- hydrogen bonding) between PVA chains.<sup>33</sup> The last method directly affect the chances of PVA to form a crystalline long-range order structure; the more unbonded hydroxyl groups within the matrix, the less crystalline and elastic is the hole PVA sample.<sup>34</sup> Both ways of water interaction contribute to the reduction of the elasticity of the solution. Then, hydrated PVA (without a crystalline long-range structure) is more likely to expend energy in the form of friction and heat dissipation than store it during deformation ( $G' > G''$ ).<sup>35</sup>

The effect of water content on the viscoelastic properties of samples S and SPPG was better appreciated in Figure 4-7. Figure 4-7 presented the visual LVR determination for samples S and SPPG at 20 wt.%, 30 wt.%, 40 wt.% and 50 wt.% polymer. Generally, lower oscillation stresses and lower values of strain were reported at higher water content in samples S and SPPG. For example, sample S at 20 wt.% polymer reported an LVR of 0.39 % at 2.1 Pa while the same sample at 50 wt.% polymer reported an LVR of 3.17 % at 4000 Pa. The higher content of water in the solution only increased the plasticizing effect by diluting the polymer and suppressing the inter- and intra- the hydrogen bonding of PVA chains.

Water was not the only element reducing the elastic component ( $G'$ ) of the total viscoelastic response. For instance, samples S and SPPG at 50 wt. % polymer reported an LVR of 3.17 % at 269 Pa and 1.03 % at 21 Pa respectively. The combined addition of water and propylene glycol in sample SPPG induced a more significant reduction of the elastic properties of PVA compared to the addition of water alone in sample S. This behavior is expected as propylene glycol is a well-known plasticizer for PVA.<sup>28</sup> Also, Wright et.al., demonstrated that the addition of propylene glycol to water as a cosolvent in PVA solution has a better diluting effect than water alone.<sup>36</sup> Then, the addition of propylene glycol and water mix multiply the softening effect on the matrix as it can dissolve PVA chains and interfere more efficiently with the inter- and intra- hydrogen bonding once again reducing the chances for PVA to form long-range crystalline structures.<sup>34</sup>

Most importantly, the addition of propylene glycol produced a dilution effect on the polymer load of sample SPPG. The total polymer load of sample SPPG splits between PVA at 85% and propylene glycol at 15%. That is, 15% of the total polymer load is a plasticizing low molecular mass element. Then, the reduced elastic response ( $G'$ ) of sample SPPG, compared to sample S, is the product of a combined effect of a reduced number inter- and intra- hydrogen bonds between PVA chains and a substantial dilution of the polymer matrix (lower wt.% of PVA in the specimen). In short, the viscoelastic response of sample S and SPPG was a function of polymer concentration and the amount of propylene glycol. These two factors defined the  $C_e$  values. The  $C_e$  values summarized in Table 4-3 are replotted as  $C_e$  as a function solvent shear rate in Figure 4-11. Figure 4-11 suggests that  $C_e$  is proportional to the solvent shear rate and inversely proportional to the elasticity ( $G'$ ) of the sample. In other words, sample SPPG needs a lower dilution than sample S to reach favorable conditions for erosion to happen at the surface of the gel-solvent interface for a given specific solvent shear rate.

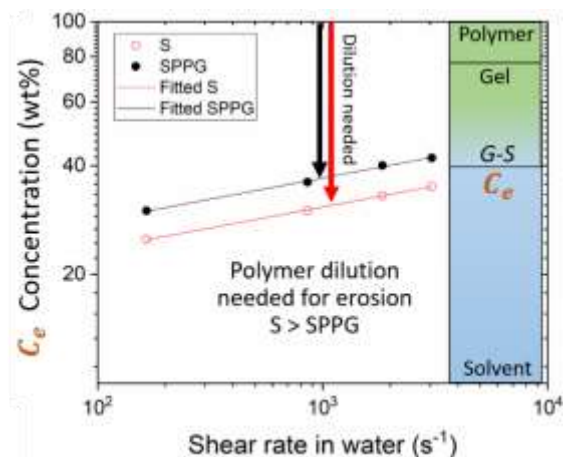


Figure 4-11.  $C_e$  versus the solvent shear rate in the stirrer-vial test for samples S and SPPG. Sample SPPG needs less dilution than sample S to reach adequate condition to start erosion for a given solvent shear rate.

The  $C_e$  values that were determined using shear oscillatory rheometry are considered good approximations because they are congruent with the results from the stirrer-vial dissolution test shown in Figure 4-9. Sample SPPG showed the highest  $C_e$  and highest mass transfer fluxes compare to sample S. For instance,  $C_e$  (at  $3665 R_e$ ) is 42 wt.% and 35 wt.% for sample SPPG and S respectively. If the initial concentration of the specimen in the stirrer-vial test was 44 wt.%, sample SPPG required a lower amount of solvent to penetrate in order to reach the critical erosion concentration compared to sample S. In this order of ideas, Sample SPPG always will start the erosion behavior before sample S for a given Reynolds number just as Figure 4-9 showed.

#### 4.4.2 Mass flux at the gel-solvent interface

Visualizing and capturing the dissolution phenomena was the second challenge during the development of this protocol. A custom-made stirrer-vial set-up (see Figure 4-2) was used to track down the position over time of the gel-solvent interface. The results presented in Figure 4-9 showed two different behaviors of the gel-solvent interface as a function of the solvent Reynolds number: swelling and erosion (illustrated in Figure 4-12). These two evolutions of the gel-solvent interface should not be independent of each other as swelling of the polymer matrix is the first step toward erosion.<sup>5</sup> However, these behaviors are independently analyzed in this experiment as different convection conditions produce swelling or erosion.

The observation of swelling behavior ( $+\Delta x$ ) in samples S and SPPG occurred at a Reynolds number of 524. As the solvent penetrated the semi hydrated matrix (44 wt.% polymer), it caused the displacement of the gel-solvent interface towards positives values of  $x$  as shown in Figure 4-12a.<sup>10</sup> The swelling behavior depicted a square root of time dependency typically of the initial stages of polymer dissolution.<sup>37</sup> This dependency is the product of a non-linear gradient of solvent concentration analogous to the formation of a variable diffusive layer.<sup>38</sup>

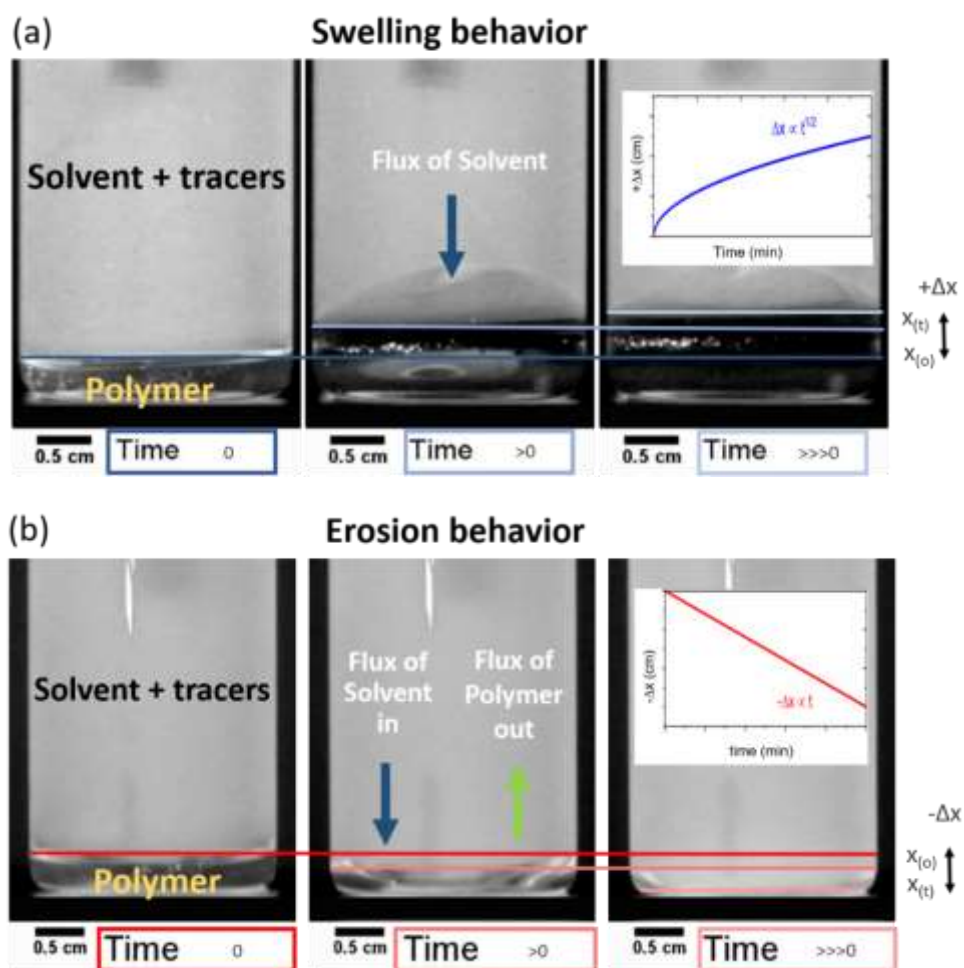


Figure 4-12. The evolution of the gel-solvent interface over time and its dependency with applied Reynolds number. (a) Swelling behavior ( $+\Delta x$ ) at low  $R_e$  showed a square root of time dependency (b) Erosion behavior ( $-\Delta x$ ) at high  $R_e$  showed a linear time dependency.

The swelling behavior is purely due to solvent intake; it depends on the elasticity and free volume of the matrix and the molecular size of the solvent.<sup>39 40</sup> In the case of sample S and SPPG, the

solvent is the same, but the elasticity and free volume of the matrix are different. As previously demonstrated during the dynamic shear rheometry experiments (see Figure 4-7), the softness of the SPPG matrix is congruent with the ability of the water molecules to penetrate the matrix since swelling is more significant for sample SPPG than sample S (see Figure 4-9). The water penetration is aided by the expected larger free volume of sample SPPG since it contains a larger density of chain-ends. (from a low molecular mass propylene glycol) compared to sample S.<sup>41 42</sup> All the statements above are also congruent with the calculated diffusion coefficients for a penetrating solvent using Equation 4-5 ( $D=2.1 \times 10^{-4} \text{ cm}^2.\text{s}^{-1}$  for SPPG is greater than  $D=3.8 \times 10^{-5} \text{ cm}^2.\text{s}^{-1}$  for S).

Conversely, the observation of erosion behavior in sample S and SPPG ( $-\Delta x$ ; displacement of the gel-solvent interface toward negative values as shown in Figure 4-12b) occurred at Reynolds numbers of 1571, 2618 and 3665 at different mass flux rates. At these Reynolds numbers, swelling of the matrix (formation of a gel layer) was not observed because the flow conditions forced any swollen layer to mix immediately with the solvent.<sup>13</sup> Consequently, a steady state concentration profile in which both the polymer and solvent are considered well mixed is reached. Then, the erosion rate was entirely analogous to the polymer disengagement rate at the gel-solvent interface caused by solvent-induced deformation.<sup>43</sup> The above explains why the erosion behavior depicted the linear time dependency for both samples as observed in Figure 4-9.

The linear time dependency allowed the calculation of mass transfer coefficients to explain the erosion behavior of samples S and SPPG (See Equation 4-6). The diffusive (solvent penetration) and convective (shear rates) terms are lumped in one parameter ( $K_{eP}$ ) simplifying the analysis of polymer dissolution.<sup>25</sup> The mass transfer coefficients for sample S ( $1.5 \times 10^{-6} \text{ cm}.\text{s}^{-1}$ ,  $4.2 \times 10^{-6} \text{ cm}.\text{s}^{-1}$ , and  $3.2 \times 10^{-5} \text{ cm}.\text{s}^{-1}$  for 1571, 2618 and 3665  $R_e$  respectively) are lower than those observed in sample SPPG ( $1.9 \times 10^{-5} \text{ cm}.\text{s}^{-1}$  and  $4.9 \times 10^{-5} \text{ cm}.\text{s}^{-1}$  for 1571 and 3665  $R_e$  respectively). The faster dissolution behaviors of sample SPPG compared to sample S is congruent with previous results of dissolution of plasticized polymers.<sup>44</sup> The same conceptual model used to explain swelling behavior can be used to explain the erosion behavior; both depend on the capacity of the polymer to relax upon externally applied stresses. Sample SPPG with lower elasticity ( $G'$ ) has a greater chance for a faster erosion at given water-shear stress.

Lastly, the experimental data in Figure 4-9 suggested the existence of an onset Reynolds number (onset was not calculated). This onset  $R_e$  defined the minimum convection conditions that balanced the erosion rate with the swelling rate of the specimen (as long as the specimen keeps a core at the initial polymer concentration to keep supplying the events). For instance, the gel-solvent interface position of sample S at a Reynold number of 1571 holds a value close to zero  $\Delta x$  for a long period of time. The physical importance of the onset Reynolds number is the determination of minimum shear rate conditions to prevent the accumulation of polymer in the surface of the gel-solvent interface.

#### 4.4.3 Mass transfer correlations

The mass transfer behavior across interfaces (fluid-solid in this case) is usually reported in terms of non-dimensional numbers called mass transfer correlations.<sup>25</sup> Very often, elucidating the influence of convective versus diffusive term on a mass transfer experiment is communicated by the empirical Sherwood number ( $S_h$ ) as a function of Reynolds number ( $R_e$ ) in the form of Equation 4-8.

Equation 4-8. The general form of a fluid-solid mass transfer correlation. A and B are constants that depend on the geometry and velocity regime of the experiment performed. B=0.5 has been found for experiments under laminar flow while B=1 has been found for turbulent flows.

$$S_h = A * R_e^B S_c^{1/3}$$

$S_h$  is generally the dependent variable which relates the mass transfer velocity to diffusion velocity as follows  $S_h = \frac{kd}{D_{Chain}}$ , where  $k$  is the experimental mass transfer coefficient,  $d$  is the impeller diameter and  $D_{Chain}$  is the diffusion coefficient of a polymer coil in water. Reynolds number is the independent variable that encompasses the inertial and viscous forces. Usually, the Schmidt number ( $S_c$ ) is also included as a constant pre-factor.  $S_c$  relates the diffusivity of momentum versus diffusivity of mass as follows  $S_c = \frac{\mu}{D_{Chain}}$ , where  $\mu$  is the kinematic viscosity.

Figure 4-13 exhibit the empirical mass transfer correlation for the dissolution of samples S and SPPG. Data from the stirrer-vial experiment (during erosion behavior) coupled with the measurements of the diffusion coefficient of a polymer coil in water ( $D_{Chain}$ ) from an independent DLS experiment are used to calculates the  $S_h$  as a function of  $R_e$ . However, few experimental

points are available to build a meaningful correlation. Hence, it is imperative to continue gathering more data points to fill the gaps of the curve presented in Figure 4-13.

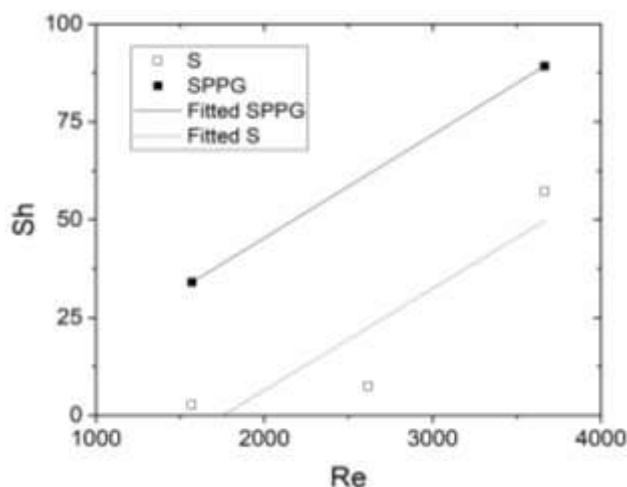


Figure 4-13. Empirical Sherwood number as a function of Reynolds number of sample S and SPPG on the stirrer-vial dissolution test.

#### 4.4.4 Stirrer-vial versus films dissolution test.

The film dissolution experiment and the stirrer-vial dissolution experiment are both tools that calculate a rate of mass transfer of polymer into a solvent. They apply different convection conditions at the gel-solvent interface. The stirrer-vial test induced forced convection by using a velocity-controlled stirrer. Conversely, the film dissolution test induced forced convection by the action of gravity by regularly washing away any gel layer. These convection conditions keep the polymer and solvent as well-mixed solutions in both cases. Thus, it could be possible to find solvent shear rates in the stirrer-vial test that match the shear rates of gravity force acting on the surface of the film.

Figure 4-10 showed the existence of a film thickness range in which the data from both tests are correlated through a constant factor (film experimental dissolution time is approximate 0.5 times the calculated dissolution time for sample S). It is difficult to provide the root reasons for such behavior, but an analysis of the physical condition of the film dissolution test supports consistency across both test.

A well-mixed solution condition in both experiments generates steady-state diffusion of solvent molecules into the matrix. If the initial film thickness of the specimen is below the critical thickness, the rate of water penetration is proportional to the film weakening rate. Then, the breakage time for films is proportional to the film thickness (analogous to erosion behavior in the stirrer-vial test). However, if the initial film thickness is above the critical thickness, the rate of water penetration will not be proportional to the film weakening rate as the water molecules will have to travel further to hydrate the matrix creating gradients of solvent concentration.

Indeed, empirical evidence from both tests results in an acceptable phenomenological correlation to measure dissolution time. However, precaution must be taken when drawing conclusions because arbitrarily-selected parameters from the stirrer-vial test were used to calculate the dissolution time of films using Equation 4-6. Also, differentiating the time for a film to break/rupture versus the total time to dissolve from the stirrer-vial test is important. Once a film breaks, the surface area can change in ways that enhance dissolution (*i.e.*, break up into multiple thin films) or slow down dissolution (films may roll up into slabs).

#### **4.5 Summary and Implications**

This study demonstrated the potential of macro scale visualization and shear rheology work-flow to measure polymer dissolution as a function of solvent shear rate. The principal objective was to lay down the foundations for a cost-effective work-flow where variables could be lumped, and numerous samples tested rapidly. It was found that a simple apparatus can be used to calculate relative changes in polymer mass flux under dissolution.

Oscillatory shear rheometry played a significant role in the determination of the critical erosion concentration. Applying a fundamental understanding of rheology was necessary to create the bridge that correlated the solvent shear rates with the erosion behavior at the gel-solvent interface. Although it is possible to use rotational and oscillatory rheometry to calculate an erosion concentration, only oscillatory measurements were adequate for the polyvinyl alcohol used in this experiment.

Being able to dial-in various solvent Reynolds numbers enabled the exploration of different evolution regimes at the gel-solvent interface. The stirrer-vial set up allowed to bracket the convection conditions creating independent experiments for each flow regime. Such capabilities are of great relevance to study polymer dissolution under real shear conditions. With enough observations, it would be possible to find the minimum solvent shear rate to avoid gradients of concentrations in water-soluble polymers.

Relative differences in the viscoelastic response of sample S and SPPG were observed in the polymer dissolution behavior. The highest rate of dissolution was observed in sample SPPG. The root reason is the lower elasticity and greater free volume of sample SPPG compared to sample S. The addition of propylene glycol played a dual effect of dilution and plasticization.

An initial and valuable contribution of future work would be to standardize the stirrer-vial set up so, it agrees with most common geometries used in mixing. Furthermore, greater insights could surface from a more detailed analysis of the solvent shear rates. It will be beneficial to develop a more robust mathematical model that describes in greater detail the swelling and erosion behavior introducing polymer physical constants into account.

In general, the presented work-flow showed with efficacy how the swelling and erosion behaviors are tightly dependent on the viscoelastic response of the sample, creating the opportunity to use the presented protocol as a screening tool for an initial decision-making exercise over considerable changes in the formulation of possible water-soluble polymers.

#### 4.6 References

1. Kerry J, Butler P. *Smart Packaging Technologies for Fast Moving Consumer Goods*. John Wiley; 2008.
2. Selke SEM, Culter JD. *Plastics Packaging : Properties, Processing, Applications, and Regulations*. <https://www.sciencedirect.com/book/9783446407909/plastics-packaging>. Accessed March 11, 2019.
3. Swift G. Requirements for biodegradable water-soluble polymers. *Polym Degrad Stab*. 1998;58:19-24. doi:[https://doi.org/10.1016/S0141-3910\(97\)00162-6](https://doi.org/10.1016/S0141-3910(97)00162-6)

4. Parker A, Vigouroux F, Reed WF. Dissolution kinetics of polymer powders. *AIChE J.* 2000;46(7):1290-1299. doi:10.1002/aic.690460703
5. Miller-Chou BA, Koenig JL. A review of polymer dissolution. *Prog Polym Sci.* 2003;28(8):1223-1270. doi:10.1016/S0079-6700(03)00045-5
6. Narasimhan B. Mathematical models describing polymer dissolution: consequences for drug delivery. *Adv Drug Deliv Rev.* 2001;48:195-210. doi:10.1016/S0169-409X(01)00117-X
7. Ugur S, Dinc AK, Kislak Y. Effect of molecular weight on the dissolution properties of polystyrene latex films. *J Polym Res.* 2012;19(9):9943. doi:10.1007/s10965-012-9943-0
8. Devotta I, Ambeskar V., Mandhare A., Mashelkar R. The life time of a dissolving polymeric particle. *Chem Eng Sci.* 1994;49(5):645-654. doi:10.1016/0009-2509(94)85010-0
9. Lee PI, Peppas NA. Prediction of polymer dissolution in swellable controlled-release systems. *J Control Release.* 1987;6(1):207-215. doi:10.1016/0168-3659(87)90077-0
10. Ueberreiter K, Asmussen F. Velocity of dissolution of polymers. Part I. *J Polym Sci.* 1962;57(165):187-198. doi:10.1002/pol.1962.1205716515
11. Pekcan Ö, Canpolat M, Kaya D. In situ fluorescence experiments for real-time monitoring of annealed high-T latex film dissolution. *J Appl Polym Sci.* 1996;60(12):2105-2112. doi:10.1002/(SICI)1097-4628(19960620)60:12<2105::AID-APP7>3.0.CO;2-Q
12. Peppas NA, Wuf JC, Von Meerwall ED. *Mathematical Modeling and Experimental Characterization of Polymer Dissolution.* Vol 27.; 1994. <https://pubs.acs.org/sharingguidelines>. Accessed March 11, 2019.
13. Pekcan Ö, Uğur Ş, Yılmaz Y. Real-time monitoring of swelling and dissolution of poly(methyl methacrylate) discs using fluorescence probes. *Polymer (Guildf).* 1997;38(9):2183-2189. doi:10.1016/S0032-3861(96)00769-0
14. Ouano AC, Carothers JA. Dissolution dynamics of some polymers: Solvent-polymer boundaries. *Polym Eng Sci.* 1980;20(2):160-166. doi:10.1002/pen.760200208
15. Cooper WJ, Krasicky PD, Rodriguez F. Effects of molecular weight and plasticization on dissolution rates of thin polymer films. *Polymer (Guildf).* 1985;26(7):1069-1072. doi:10.1016/0032-3861(85)90230-7

16. Valois P, Verneuil E, Lequeux F, Talini L. Understanding the role of molar mass and stirring in polymer dissolution. *Soft Matter*. 2016;12(39):8143-8154. doi:10.1039/c6sm01206j
17. Meeuwse M, Lempers S, Van Der Schaaf J, Schouten JC. Liquid-Solid Mass Transfer and Reaction in a Rotor-Stator Spinning Disc Reactor. doi:10.1021/ie1003366
18. Asmussen F, Ueberreiter K. Velocity of dissolution of polymers. Part II. *J Polym Sci*. 1962;57(165):199-208. doi:10.1002/pol.1962.1205716516
19. Krasicky PD, Groele RJ, Jubinsky JA, Rodriguez F, Namaste YMN, Obendorf SK. Studies of dissolution phenomena in microlithography. *Polym Eng Sci*. 1987;27(4):282-285. doi:10.1002/pen.760270408
20. Papanu JS, Hess DW, Bell AT, Soane DS. In Situ Ellipsometry to Monitor Swelling and Dissolution of Thin Polymer Films. *J Electrochem Soc*. 1989;136(4):1195. doi:10.1149/1.2096852
21. Uğur S, Pekcan Ö. Fluorescence technique to study thickness effect on dissolution of latex films. *J Appl Polym Sci*. 2000;77(5):1087-1095. doi:10.1002/1097-4628(20000801)77:5<1087::AID-APP16>3.0.CO;2-K
22. Peppas NA, Wu JC, von Meerwall ED. Mathematical Modeling and Experimental Characterization of Polymer Dissolution. *Macromolecules*. 1994;27(20):5626-5638. doi:10.1021/ma00098a017
23. van der Weerd J, Andrew Chan K., Kazarian SG. An innovative design of compaction cell for in situ FT-IR imaging of tablet dissolution. *Vib Spectrosc*. 2004;35(1-2):9-13. doi:10.1016/J.VIBSPEC.2003.11.004
24. Sánchez Pérez JA, Rodríguez Porcel EM, Casas López JL, Fernández Sevilla JM, Chisti Y. Shear rate in stirred tank and bubble column bioreactors. *Chem Eng J*. 2006;124:1-5. doi:10.1016/j.cej.2006.07.002
25. Cussler EL. *Diffusion : Mass Transfer in Fluid Systems*. Cambridge University Press; 2009.
26. Barkoula N-M, Karger-Kocsis J. Review Processes and influencing parameters of the solid particle erosion of polymers and their composites. *J Mater Sci*. 2002;37(18):3807-3820. doi:10.1023/A:1019633515481

27. Lyoo WS, Kim BC, Ha WS. Rheological and rheo-optical properties of high molecular weight syndiotactic and atactic polyvinylalcohol solutions. *Polym Eng Sci*. 1997;37(7):1259-1265. doi:10.1002/pen.11770
28. Han Cho Y, Chul Kim B, Sik Dan K. Effects of Propylene Glycol on the Physical Properties of Poly(vinyl alcohol) Solutions and Films. *Macromol Res*. 2009;17(8):591-596. <https://link.springer.com/content/pdf/10.1007%2F03218914.pdf>. Accessed March 6, 2019.
29. Manneville S, Colin A, Waton G, Schosseler F. Wall slip, shear banding, and instability in the flow of a triblock copolymer micellar solution. *Phys Rev E - Stat Nonlinear, Soft Matter Phys*. 2007;75(6):1-11. doi:10.1103/PhysRevE.75.061502
30. Rwei S-P, Huang C-C. Electrospinning PVA solution-rheology and morphology analyses. *Fibers Polym*. 2012;13(1):44-50. doi:10.1007/s12221-012-0044-9
31. Cooper WJ, Krasicky PD, Rodriguez F. Dissolution rates of poly(methyl methacrylate) films in mixed solvents. *J Appl Polym Sci*. 1986;31(1):65-73. doi:10.1002/app.1986.070310107
32. Larson RG. *The Structure and Rheology of Complex Fluids (Topics in Chemical Engineering)*. Oxford University Press; 1999.
33. Gao H-W, Yang R-J, He J-Y, Yang L. Rheological behaviors of PVA/H<sub>2</sub>O solutions of high-polymer concentration. *J Appl Polym Sci*. 2009;116(3). doi:10.1002/app.31677
34. Takizawa A, Negishi T, Ishikawa K. Sorption of water vapor by poly(vinyl alcohol): Influence of polymer crystallinity. *J Polym Sci Part A-1 Polym Chem*. 1968;6(3):475-484. doi:10.1002/pol.1968.150060304
35. Macosko CW. *Rheology: Principles, Measurements, and Applications*. Vol 41. Wiley-Blackwell; 1995. doi:10.1002/aic.690411025
36. Wright EJ, Andrews GP, McCoy CP, Jones DS. The effect of dilute solution properties on poly(vinyl alcohol) films. *J Mech Behav Biomed Mater*. 2013;28:222-231. doi:10.1016/J.JMBBM.2013.08.002
37. Tu Y-O, Ouano AC. Model for the Kinematics of Polymer Dissolution. *IBM J Res Dev*. 1977;21(2):131-142. doi:10.1147/rd.212.0131
38. Crank J. *The Mathematics of Diffusion*. 2nd ed. Oxford University Press; 1975.

39. Devotta I, Mashelkar RA. Role of Thermodynamic and Kinetic Factors in Polymer Dissolution in Mixed Solvents. *Chem Eng Commun.* 1997;156(1):31-43.  
doi:10.1080/00986449708936667
40. Ouano, A.C.; Carothers JA. Dissolution Dynamics of Some Polymers: Solvent-Polymers Boundaries. *IBM J Res Dev.* 1980;20(2):160-166.
41. Buera M del P, Levi G, Karel M. Glass transition in poly(vinylpyrrolidone): effect of molecular weight and diluents. *Biotechnol Prog.* 1992;8(2):144-148.  
doi:10.1021/bp00014a008
42. Liu H, Wilén C-E. Extension of the chain-end, free-volume theory for predicting glass temperature as a function of conversion in hyperbranched polymers obtained through one-pot approaches. *J Polym Sci Part B Polym Phys.* 2004;42(7):1235-1242.  
doi:10.1002/polb.10772
43. Devotta I, Badiger MV, Rajamohanan PR, Ganapathy S, Mashelkar RA. Unusual retardation and enhancement in polymer dissolution: Role of disengagement dynamics. *Chem Eng Sci.* 1995;50(16):2557-2569. doi:10.1016/0009-2509(95)00103-C
44. Rodriguez F, Krasicky PD, Groele RJ . Dissolution rate measurements. *Solid State Technol.* 1985;28(5):125-131.

## 5. CONCLUSIONS AND FUTURE WORK

### 5.1 Conclusion

This dissertation studied the role of mesoscopic microstructural factors that control the rheological behavior of three microstructured fluids with high potential for transformation into products. Three applied rheometry protocols with proven efficacy in the relative measurement of flow properties of microstructured fluids through the combination of interdisciplinary characterization techniques were developed. An important and valuable addition to this study was the integration of flow-velocimetry techniques which elucidate the gray areas of measuring flow properties of microstructure fluids using shear rheometry. The combination of shear rheometry, flow velocimetry, scattering characterization, flow birefringence, and mass transfer calculations showed potential to build robust sets of experimental evidence that can be used to aid in the design of tailored rheologies that drive the successful transformation of novel microstructured fluids into commercial products.

Three main topics of research were covered: the effects of solvent evaporation over the flow behavior of self-assembly block copolymers, the effect of shear deformation over the flow behavior of lyotropic structures of concentrated surfactants and the effect of a penetrating solvent over the flow behavior of water-soluble polymers.

Chapter 2 showed the role of the triblock terpolymer chemistry and solvent evaporation over the mechanical strength development of polymer solutions used to fabricate membranes via SNIPS. The rheological properties of the triblock copolymer solutions were strongly dependent on the ability of the block copolymer molecule to form a long-range organization which in turn is dependent of the chemical structure of the triblock copolymer molecule, the block-block and block-solvent interactions, and the concentration of polystyrene within the block copolymer molecule. A hierarchical order ( $ISV > ISB > ISD$ ) in magnitude was observed for rheological properties under minimal and significant solvent evaporation, with ISV solutions displaying the highest values. These findings may have potential to tailor the morphology of a SNIPS membrane

by designing specific molecule combinations (blocks) that achieve the desired viscosity, micelle mobility, and a final macro-void support layer in a roll-to-roll set-up.

Chapter 3 demonstrated the complexity of measuring lyotropic surfactant microstructures using shear rheometry. A key result was the demonstration of the fact that shear-induced artifacts are the root cause for common features of flow curves such as shear thinning behavior. For instance, wall-slip was observed in worm-like micelles while plug flow was observed in Lamellar-40 and Lamellar-70 samples. Wall slip occurred because the application of a relevant shear rate exceeded the relaxation behavior of the worm-like sample. Conversely, plug flow was attributed to the formation of lubricating layers linked to the deformation of small elastic domains in Hexagonal and Lamellar samples. The manifestation of the shear-induced artifacts was then a factor of the surfactant concentration, ionic strength, and shear rate application.

Chapter 4 displayed the potential of a macro-scale visualization technique paired with shear rheometry to measure lumped parameters of mass transfer in polymers. The designed dissolution test allowed the application of specific forced convection conditions at the surface of the polymer to study polymer dissolution as a function of solvent Reynolds number. Oscillatory rheometry played a significant role in the determination of critical erosion concentrations by measuring the viscoelastic response of water-soluble polymers. The dissolution rate of polyvinyl alcohol (PVA) was fueled by the presence of propylene glycol that reduced the crystallinity and thus the viscoelasticity of the PVA matrix. The experimental data demonstrated that the presented workflow might be used as a screening tool for an initial decision-making exercise on polymer blend formulation.

## **5.2 Future Work**

Future work can expand from every chapter presented in this dissertation. First, it is appropriate to state that performing flow-velocimetry measurements on each material studied in this dissertation using USV technique would be beneficial for further continuation and validation of each developed protocol. Also, it would be appropriate to test materials with similar physical and chemical characteristics on each protocol to obtain a greater reference data set.

Chapter 2 could use a visualization technique to prove that the radial rate of film development while measuring viscoelastic properties under significant evaporation is indeed equivalent for all evaluated block copolymers in solution. Constant diffusion coefficients are used to validate this assumption, but visual confirmation would help to communicate that the apparent  $G'$  value is solely a function of the differences in the molecular structure of block copolymers and properties of their solutions. Also, the dynamic transformation of ISB and ISD microstructure under solvent evaporation should be studied using *in situ* grazing incidence small-angle x-ray scattering as *Gu et al.*, did with the ISV sample. This set of data will support the rheological behavior of the three studied molecules. The implementation of this new experiments could lead to a more robust protocol for block copolymer design.

Chapter 3 could expand its reach by studying samples that use different sources for counterions and co-solvents to recreate distinct variants of the current formulations. Furthermore, to increase the experimental evidence on shear induced microstructures, all lyotropic structures such as hexagonal and lamellar phases should be fully studied using the Linkam shear cell coupled with optical microscopy. This new set of visual evidence would help to deconvolute the dynamics of transient rheological behaviors and the factors that trigger the recovery of simple shear conditions from flow instabilities. Lastly, the addition of oscillatory shear rheometry would be a valuable inclusion to this study in order to quantify the particular timescale of microstructural reorganization.

Chapter 4 could use the standardization of the stirrer-vial set-up. Hence, all the results gathered could be compared with others that are doing similar experiments. Furthermore, greater insights could surface from a more detailed analysis of the solvent shear rates at the surface of the polymer instead of using an average shear rate. Moreover, a greater number of data points (solvent Reynolds number) are needed to complete the mass transfer correlation of Sherwood number as a function of Reynolds number. Finally, although it is not imperative, it will be beneficial to develop a more robust mathematical model that describes in greater detail the swelling and erosion behavior of polymer, introducing physical constants of a dissolving polymer.

## VITA

Eduard is a Materials Engineer born and raised in the Republic of Colombia. His expertise comprehends bridging established science with manufacturing-scale engineering applications. He has actively participated in academic as well as corporate engineering research where he had developed applied rheology workflows for optimizing both product-making and consumer-use experiences.

Eduard graduated from Universidad del Valle (Colombia) in 2009 with a BS in Materials Engineering, and in 2012 with an MS in Materials Engineering. In the Universidad del Valle, he spent three years of his undergraduate and graduate career at the GMC (“Grupo de Materiales Compuestos”) research group. During this time, Eduard developed and tested new cementitious materials based on the re-use of industrial and agricultural byproducts such as fly ash and rice husk ash.

Eduard entered the Ph.D. program in Materials Engineering at Purdue University in 2014. In the Soft Material Mechanics group at Purdue University, he developed expertise in the rheology of complex fluids including rheo-visualization techniques on formulated products, and hydration/swelling of cross-linked hydrogels. He presented his results in recognized conferences such as the Society of Rheology Meeting and published in peer-reviewed journals such as *Rheological Acta* and *Journal of Applied Polymer Science*. In 2018 as part of a collaboration project between Purdue University and Procter and Gamble Co., Eduard was embedded in the Procter and Gamble corporate engineering group for eleven months developing workflows to measure polymer dissolution.

Eduard awaits for his graduation from the Ph.D. program in Materials Engineering at Purdue University in Spring 2019 under the mentoring of Dr. Kendra A. Erk. He foresees a future in engineering in which he creates smooth transitions for upcoming technologies to be used in the soft materials industry.